

University of Louisville

ThinkIR: The University of Louisville's Institutional Repository

Electronic Theses and Dissertations

5-2017

Novel III-V alloys for unassisted water splitting.

Alejandro Martinez-Garcia

University of Louisville

Follow this and additional works at: <http://ir.library.louisville.edu/etd>



Part of the [Other Chemical Engineering Commons](#)

Recommended Citation

Martinez-Garcia, Alejandro, "Novel III-V alloys for unassisted water splitting." (2017). *Electronic Theses and Dissertations*. Paper 2664.
<https://doi.org/10.18297/etd/2664>

This Doctoral Dissertation is brought to you for free and open access by ThinkIR: The University of Louisville's Institutional Repository. It has been accepted for inclusion in Electronic Theses and Dissertations by an authorized administrator of ThinkIR: The University of Louisville's Institutional Repository. This title appears here courtesy of the author, who has retained all other copyrights. For more information, please contact thinkir@louisville.edu.

NOVEL III-V ALLOYS FOR UNASSISTED WATER SPLITTING

By

Alejandro Martinez-Garcia

A dissertation

Submitted to the Faculty of the

J.B. Speed School of Engineering, University of Louisville

in partial Fulfillment of the requirements

for the degree of

Doctor of Philosophy in Chemical Engineering

Department of Chemical Engineering

University of Louisville

Louisville, KY 40292

May 2017

NOVEL III-V ALLOYS FOR UNASSISTED WATER SPLITTING

By

Alejandro Martinez-Garcia

Bachelor of Engineering, Universidad de los Andes (Colombia), 2008

Master of Engineering, Universidad de los Andes (Colombia), 2012

A Dissertation Approved on

April 20, 2017

By the Following Dissertation Committee

Dr. Mahendra K. Sunkara (Dissertation Director)

Dr. Thomas Starr

Dr. Xiao – an Fu

Dr. Shamus McNamara

Dr. Joshua Spurgeon

ACKNOWLEDGEMENTS

The author wishes to acknowledge his advisor Dr. Mahendra K. Sunkara for mentorship and the Conn Center for Renewable Energy Research, The University of Louisville, J.B. Speed School of Engineering for financial support through the University Fellowship, Speed School Graduate Fellowship, and The Grosscurth Fellowship. The National Science Foundation, and the U.S. Department of Energy, are acknowledged for supporting this work through grants DOE- EPSCoR (DE-FG02-07ER46375) and Kentucky's Experimental Program to Stimulated Competitive Research KY-NSF EPSCoR "Powering the Kentucky Bioeconomy for a Sustainable Future". The author would also like to acknowledge the National Renewable Energy Lab (NREL) for support through collaboration for characterization of samples, valuable discussions and academic exchange.

The thesis committee members are acknowledged for their valuable insights. I wish to thank Dr. Swathi Sunkara, Dr. Ben Russell, Dr. William Paxton, Dr. Srikanth Ravipati, Dr. Madhu Menon, and Dr. Jacek Jacinski for their contributions. I would also like to express my gratitude to all my labmates and Conn Center staff, but most especially to my dear friend Daniel Jaramillo for constant support and lending his clinical eye for troubleshooting.

The U.S DOE Office of Energy Efficiency and Renewable of Energy is acknowledged for its important mission to create and sustain American leadership in the transition to a global clean energy economy and its vision of strong and prosperous America powered by clean, affordable, and secure energy.

DEDICATION

This thesis is dedicated to my beloved family.

María del Rosario, Luis Alejandro, and Andrés.

Thank you for your words of encouragement and support along the way.

ABSTRACT

NOVEL III-V ALLOYS FOR UNASSISTED WATER SPLITTING

Alejandro Martinez-Garcia

April 20, 2017

Direct conversion of solar energy to fuels by photoelectrochemical (PEC) water splitting has been identified as a promising route for sustainable power generation and storage. However, semiconductor materials with suitable opto-electronic properties have yet to be identified. In this dissertation, band gap engineering of III-V alloys, tuning the light sensitivity of GaP and GaN nitride through alloying Sb, is investigated for developing new semiconductor alloys with appropriate opto-electronic properties and their performance with overall water photoelectrolysis. In addition to III-V materials, copper oxide (Cu_2O) was investigated as a p-type electrode. Metal organic chemical vapor deposition, halide vapor phase epitaxy and hot filament chemical vapor deposition methods were employed for the synthesis of tunable III-V alloys and wide band gap semiconductors as photoanodes and photocathodes.

Synthesis of p- $\text{Cu}_2\text{O}/\text{WO}_3$ core-shell nanowire arrays resulted in a five-fold improvement of the photocurrent density compared to TiO_2 -coated copper oxide nanowire arrays. The deposition of WO_3 and CuWO_4 reduced the CuO phase impurities in Cu_2O leading to considerable enhancement of the photocathode activity in terms of charge separation and stability.

Nearly epitaxial films of $\text{GaSb}_x\text{N}_{(1-x)}$ were grown on lattice matching and miss-matching substrates, studying the effect of substrate temperature and metal precursor ratios in the incorporation of antimony. The photovoltages and the very high carrier concentration of nearly epitaxial $\text{GaSb}_x\text{N}_{(1-x)}$ films suggests that un-intentional doping causes a high degree of degeneracy and a metallic character of the electrodes. This helps explain the lack of a depletion region in the epitaxial films of $\text{GaSb}_x\text{N}_{(1-x)}$ due to continuous density of states between the valence and conduction bands.

Un-biased water splitting with 2% solar to hydrogen efficiency under 1.5 AM illumination is reported using $\text{GaSb}_x\text{P}_{1-x}$. The optoelectronic properties of GaP are modified to study the indirect-to-direct band gap cross-over point in this ternary III-V system. The photoanodes show a photovoltage of 750 mV, photocurrents of 7 mA cm^{-2} at 10 sun illumination, and corrosion resistance at pH 0. The growth of compact, free-standing films of $\text{GaSb}_x\text{P}_{1-x}$ was achieved with inexpensive metallic precursors. Experimental results indicate that only photon energies greater than 2.68 eV generate mobile and extractable charges. Here it is demonstrated that a low penetration depth and efficient carrier extraction to the indirect conduction band of the material can be achieved above the energy level of the hydrogen reduction potential. This observation could potentially challenge the longstanding belief that direct band gap materials outperform indirect ones in regards to absorption.

Single semiconductor water splitting can be accomplished by tuning the band structure of $\text{GaSb}_x\text{P}_{1-x}$ through incorporation of antimony into the lattice of GaP. $\text{GaSb}_x\text{P}_{(1-x)}$ was tested with p-type silicon as a wired dual PEC cell. Improved photocurrent with a z-scheme configuration results from enhanced absorption of low energy photons at the p-Si photocathode, and demonstrates the feasibility of using $\text{GaSb}_x\text{P}_{(1-x)}$ in a tandem photoelectrochemical cell.

TABLE OF CONTENTS

	PAGE
ACKNOWLEDGEMENTS.....	
ABSTRACT.....	
LIST OF FIGURES.....	
1. INTRODUCTION	1
1.1. Global Energy Challenges and the Environment.....	1
1.2. Hydrogen market: present and future	4
1.3. Photoelectrochemical water splitting.....	5
1.3.1 Material requirements for water splitting	8
1.3.2 Material Challenges	12
1.4. Proposed approach.....	12
1.5. Objectives of this study.....	16
1.5.1 Specific Objectives	16
1.6. Organization of thesis	17
2. BACKGROUND	19
2.1. Introduction.....	19

2.2.	PEC water splitting fundamentals.....	19
2.3.	Review of techno-economic analysis.....	22
2.4.	State of the Art on Water Splitting	24
2.4.1.	Taxonomy of solar energy conversion systems	24
2.4.2.	Single Semiconductor photoelectrochemical cells	27
2.4.3.	Tandem Cells	28
2.5.	Review of materials and their performance in un-assisted water splitting	30
2.5.1.	Narrow band gap semiconductors.....	30
2.5.2.	Wide band gap semiconductors	32
2.5.2.1.	Oxides	32
2.5.3.	II-IV and III-V with tunable band gaps	35
2.6.	Growth considerations	40
2.7.	Antecedents of Metal Organic Chemical Vapor Deposition of GaSbN	42
3.	EXPERIMENTAL METHODS.....	45
3.1.	Computation techniques.....	45
3.2.	Metalorganic Chemical Vapor Deposition of III-Nitrides.....	45
3.3.	Halide Vapor Phase Epitaxy of III-Phosphides	51
3.3.1.	Growth of $\text{GaSb}_x\text{P}_{(1-x)}$ films	51
3.4.	Materials Characterization	53

3.5. Electrochemical Methods.....	55
3.5.1 Electrode fabrication.....	55
3.5.2 Open Circuit Potential Measurements	57
3.5.3 Mott-Schottky	58
3.5.4 Linear Sweep Voltammetry	59
3.5.5 Chronoamperometry	60
3.5.6 Incident Photon-to-Current Efficiency and Photocurrent Spectroscopy	61
4. P-TYPE Cu_2O NANOWIRE ARRAY PHOTOCATHODES.....	63
5. GROWTH AND PHOTOELECTROCHEMICAL CHARACTERIZATION OF $\text{GaSb}_x\text{N}_{1-x}$ FILMS FOR PEC	79
5.1. MOCVD Tool improvement.....	79
5.1.1 Run/vent operation.....	79
5.1.2 Extrinsic doping.....	80
5.2. GaSbN characterization	80
5.3. Vapor-liquid-solid (VLS) growth of GaSbN	111
5.4. PEC Characterization.....	114
6. GROWTH AND CHARACTERIZATION OF GaSbP FILMS.....	128
6.1. Antecedents of Metal Organic Chemical Vapor Deposition of GaSbP	128
6.2. Reactor revamping.....	128

6.2.1. Run/vent operation.....	128
6.2.2. Substrate temperature control	129
6.2.3. HVPE chemistry	129
6.3. GaSb _x P _{1-x} characterization	132
6.4. Photoelectrochemical characteristics	138
7. CONCLUSIONS	155
8. RECOMMENDATIONS.....	159
REFERENCES.....	161
CV.....	171

LIST OF FIGURES

Figure 1.1. Three different photoelectrochemical water splitting cell configurations, a) n-type semiconductor is driving the reactions, b) p-type semiconductor is driving the reaction, c) both electrodes absorb radiation of different wavelengths to drive the water splitting half-reactions.....	7
Figure 1.2 Wired dual semiconductor photoelectrochemical cell with separate reaction compartments.....	8
Figure 1.3 a) AM 0, AM 1.0 global and AM 1.5 direct spectra using ASTM data. Adapted from Chen et al. ¹³ B) Hot carrier thermalisation with above band gap illumination.	10
Figure 1.4 Band diagram of a n-type semiconductor under illumination with hole quasi-fermi level too negative (above) the OER reaction potential. ¹⁴	11
Figure 1.5 a) Band engineering of III-V alloys towards direct water photoelectrolysis	13
Figure 1.6 a) Monolithically integrated Photoanode+Photocathode design for distributed H ₂ generation, b) Light-driven suspended particle water splitting reactor for centralized H ₂ production.	15
Figure 2.1. Band energetics of an n-type photoabsorber in contact with an aqueous electrolyte. Adapted from Lewis et al. ²²	21

Figure 2.2 Simplified taxonomy of devices for solar fuels generation. (Adapted from Lewis et al. ⁹)	26
Figure 2.3 Contour plot of reported solar-to-hydrogen efficiency with single semiconductor and 2-Junction PEC Cells. ^{20,28-39} The STH values range from 0.06 to 14% represented by color scale on the right.	29
Figure 2.4 Calculated oxidation and reduction potentials for different semiconductors at pH 0. Adapted from Chen & Wang. ⁴⁰	32
Figure 2.5 a) Band gap energies of elemental and III-V semiconductors versus lattice constants. (Adapted from Ref. ⁵⁷) b) Iso efficiency plot showing the STH efficiency limits of a photocathode + photoanode (Z-scheme) (Adapted from Ref. ²⁷)	40
Figure 2.6. Strain relaxation in lattice mis-matched growth.....	41
Figure 2.7 Epitaxial relationship between GaSb _x P _{1-x} and (100) Si.....	42
Figure 2.8 GaSb _x N _{1-x} (575-800°C) and GaN (850-1000°C) films deposited by MOCVD. Adapted from Sunkara et. al., 2016.	43
Figure 2.9 Photoelectrochemical characterization of polycrystalline GaSb _x N _{1-x} films. Adapted from Sunkara. ⁷⁶	44
Figure 3.1. a) 3-D rendering of MOCVD chamber used for CFD analysis at the stagnation point b) drawing of the chamber with dimensions c) meshing d) streamlines e) radial velocity contours f) top view of GaSbN wafer	47
Figure 3.2 MOCVD reactor P&ID with gas-handling network.....	48

Figure 3.3 a) Two step growth process with Temperature and molar flux profiles, b) Air leak rate into MOCVD chamber at operating pressure.....	51
Figure 3.4 Simplified P&ID Diagram of HVPE System	53
Figure 3.5 Band diagram of an n-type semiconductor in contact with metal forming a rectifying junction.	56
Figure 4.1 a) SEM of Cu ₂ O NW array (top view), b) SEM of Cu ₂ O nanowire array coated with CuWO ₄ (top view); c) SEM of Cu ₂ O nanowire coated with WO ₃ (tilted cross-section). d) Tauc plots for the as-synthesized CuO, CuWO ₄ coated Cu ₂ O NW arrays, WO ₃ coated Cu ₂ O NWs and vacuum annealed Cu ₂ O NWs.	65
Figure 4.2 a) XRD of as deposited copper oxide nanowires (black), XRD of CuWO ₄ film on fused silica (red), b) X-ray diffraction patterns CuWO ₄ coated Cu ₂ O nanowire array (purple), c) redox model for copper oxide phase transformation.	67
Figure 4.3 a) Linear sweep voltammogram for the WO ₃ and CuWO ₄ modified Cu ₂ O NW arrays and b) as-synthesized Cu ₂ O NW	69
Figure 4.4 Chopped J-V curves for WO ₃ /Cu ₂ O	71
Figure 4.5 Phase pure Cu ₂ O a) SEM (tilt 45°), b) Tauc plot c)XRD, d) LSV at ph 5.	72
Figure 4.6 Chronoamperometry at -0.5 V vs. Ag/AgCl, for un-coated phase pure Cu ₂ O (black) and 45 minute deposition of WO ₃ on Cu ₂ O (purple).....	73
Figure 4.7 Transient open-circuit voltage for the CuWO ₄ , WO ₃ coated Cu ₂ O NWs.	75
Figure 4.8 LSV for Cu ₂ O/WO ₃ photocathodes; 15 min deposition of WO ₃ (red), 45 min deposition of WO ₃ (purple), 120 min deposition of WO ₃ (black)	76

Figure 4.9 a) Band edge positions of Cu_2O , WO_3 , CuWO_4 , TiO_2 and at pH=5 before equilibration; b) Band diagram after equilibration in the dark at 0 V vs. RHE...	77
Figure 5.1 a) cross-sectional micrograph of $\text{GaSb}_x\text{N}_{1-x}$, 775°C c) Top surface of $\text{GaSb}_x\text{N}_{1-x}$ grown at 775°C without buffer layers b) Cross-sectional micrograph of GaN 850°C, d) GaN grown 850°C without buffer layers.	81
Figure 5.2 Photoelectrochemical characterization of textured films, $E_g = 2 \text{ eV}$ a) OCP, b) chopped J-V curve, c) Mott-Schottky Plot (dark), 100 kHz.	83
Figure 5.3 Matrix of experiments in the GSR and Substrate temperature space.	85
Figure 5.4 A) Sample A (083116) cross section, 825°C. b) evolution of microstructure in GaSbN, (Adapted from S. Sunkara ⁷⁶) c) XRD	87
Figure 5.5 XRD of Samples B, C, D on Sapphire.	89
Figure 5.6 Cross-sections of Samples B, 071516g and 071516s, a) on Sapphire a) on GaN	90
Figure 5.7 XRD 010916G and 071516g and 030817g	90
Figure 5.8 SEM of Sample C (011117g) 30 min reaction, Sample D (012017g) 120 min reaction.	91
Figure 5.9 Sample E. 825°C, GaSbN on GaN, 18:1, 4 $\mu\text{mol min}^{-1}$. a) cross-section,..	92
Figure 5.10 XRD pattern for Sample E., 040416 825C, GaSbN on GaN, GSR 1:18, 4 $\mu\text{mol min}^{-1}$. Diffraction patterns of Samples G and I also shown for comparison.	93
Figure 5.11 Tauc plot Sample E. 040416 825C, GaSbN on GaN, 18:1, 4 $\mu\text{mol min}^{-1}$.	94

Figure 5.12 Lattice constants of $\text{GaSb}_x\text{N}_{1-x}$ films grown at increasing levels of TMGa to AMSb.....	96
Figure 5.13 Percent strain in the c-direction of GaSbN films grown at 825°C at different GSR values. (Black: Sapphire, dark grey: GaN, light grey: silicon)	97
Figure 5.14 Silicon crystal, a) (100) plane, b) Si (111) plane, c-d) epitaxial relationship between c- $\text{GaSb}_x\text{N}_{1-x}$ and (111) Si.....	98
Figure 5.15 Domain size in $\text{GaSb}_x\text{N}_{1-x}$ at increasing levels of GSR.	100
Figure 5.16 UV-vis Tauc plots of samples grown between 825 -850°C	101
Figure 5.17 C-parameter of samples grown at 850°C at different GSR's.....	102
Figure 5.18 XRD diffraction pattern of GaSbN films grown on Silicon wafers	103
Figure 5.19 Sample J (032216g and 032216s) were grown at a GSR 1:12 and 875°C.	104
Figure 5.20 Band gap bowing in growth experiments performed at iso-GSR as a function of substrate temperature.....	105
Figure 5.21 Scanning Electron Micrographs of GaN grown on (a) GaN, and (b,d) Sapphire, c) Tauc Plot of uv-vis spectroscopy of GaN in both substrates e) growth mechanism of GaN on Sapphire. ^{96,97}	107
Figure 5.22 SEM of VLS-grown GaSbN a) cross-section b) tilted surface (5% tilt)	112
Figure 5.23 a) Brightfield TEM image of VLS grown GaSbN (cross sectional view) , b) Pyramidal facets at the surface (detail 1) c) area for calculation of stacking fault density, d) plot profile of GaSbP showing stacking faults as peaks of high grey value.....	114

Figure 5.24 OCP and chopped J-V curves for a,c) undoped GaSbN 040416, b,d) Si:doped GaSbN 011177.....	115
Figure 5.25 Normalized OCP for nearly epitaxial GaSbN film showing the potential decay when illumination is turned off inset (linearized data).....	117
Figure 5.26 Band diagrams of textured $\text{GaSb}_x\text{N}_{(1-x)}$ electrodes in contact with two different redox couples, left) $2\text{H}^+/\text{H}_2$, right) $\text{Ru}^{+3}/\text{Ru}^{+2}$	123
Figure 6.1 HVPE-grown $\text{GaSb}_{0.03}\text{P}_{0.97}$ free-standing films a) X-ray diffraction pattern for $\text{GaSb}_x\text{P}_{(1-x)}$ (GaP [PDF 01-0722146] shown for comparison), b)-c) SEM cross-sectional views	133
Figure 6.2 a) Cross-sectional scanning electron micrograph of $\text{GaSb}_x\text{P}_{(1-x)}$ film. b) EDX spectrum of selected area c-e) Elemental maps for Ga, P and Sb.....	134
Figure 6.3 a) Simulated band structure for $\text{GaSb}_x\text{P}_{(1-x)}$, inset: Simulated Optical absorption spectra for $\text{GaSb}_{0.056}\text{P}_{0.944}$ for the three polarization directions. b) Tauc plot of Uv-Vis diffuse reflectance spectra of $\text{GaSb}_x\text{P}_{(1-x)}$ film (blue and red) and n-GaP (orange and black), c) PL spectrum (100K) for $\text{GaSb}_x\text{P}_{(1-x)}$, d) E- <i>k</i> -x diagram showing carrier excitation process, and injection to electrolyte.	135
Figure 6.4 a) XRD of GaSbP grown increasing Sb vapor pressures b) detail of refraction peak (111) c) Tauc plot of Uv-Vis diffuse reflectance spectra of $\text{GaSb}_{0.1}\text{P}_{0.9}$ films (black) , $\text{GaSb}_{0.06}\text{P}_{0.97}$ (blue), $\text{GaSb}_{0.03}\text{P}_{0.97}$ (red).	137
Figure 6.5 Secondary ion-mass spectrometry (SIMS) depth profile of silicon and antimony in a $\text{GaSb}_{0.03}\text{P}_{0.97}$ film.	140

Figure 6.6 Photoelectrochemical characterization of $\text{GaSb}_{0.03}\text{P}_{0.97}$ photoanode a) Chronopotentiometry under 10 sun chopped illumination, b) Linear sweep voltammogram under chopped illumination (10 suns) c) Mott-Schottky plot (100 Hz) in the dark d) Spectral response	141
Figure 6.7 Normalized photocurrent response obtained by photocurrent spectroscopy: Tauc plots of a $\text{GaSb}_{0.03}\text{P}_{0.97}$ a) allowed direct transition b) allowed indirect transition.	144
Figure 6.8 a) Chronoamperometry of $\text{GaSb}_x\text{P}_{(1-x)}$ photoanode at zero external bias in two electrode configuration. b) STH efficiency of $\text{GaSb}_{0.03}\text{P}_{0.97}$ at 3 different illumination intensities. c) Optical determination of oxygen concentration profile under chopped illumination. The results of a Pt vs Pt cell control cell are presented for comparison.	145
Figure 6.9 Linear sweep voltammograms for $\text{GaSb}_x\text{P}_{(1-x)}$ anode under chopped illumination with long-pass filtered light. Black curve: unfiltered AM 1.5G, Green curve: $\lambda_{\text{cutoff}} = 400$ nm; blue curve: $\lambda_{\text{cutoff}} = 550$ nm; and red curve: $\lambda_{\text{cutoff}} = 610$ nm.	146
Figure 6.10 Spectral response of $\text{GaSb}_{0.03}\text{P}_{0.97}$ photoanode with and without IrO_2 as OER co-catalyst.	146
Figure 6.11 Spectral absorption coefficients and the light penetration depths in $\text{GaSb}_{0.03}\text{P}_{0.97}$ and GaP.	148
Figure 6.12 Photoelectrochemical characterization of n -GaP photoanode a) Chronopotentiometry under 10 sun chopped illumination, b) Mott-Schottky plot	

(100 Hz) in the dark c) Linear sweep voltammogram under chopped illumination (10 suns) d) Comparative band diagram of GaSb _{0.03} P _{0.97} and GaP.....	150
Figure 6.13 Linear sweep voltammograms under chopped illumination (2 suns) in 1M H ₂ SO ₄ , a) GaSb _{0.03} P _{0.97} (black) and GaP (blue), b) GaSb _{0.03} P _{0.97} and GaSb _{0.1} P _{0.9}	
151	
Figure 6.14 Testing of a wired PEC with GaSbP photoanode and GaP coated Si photocathode.....	152
Figure 6.15 Overlapped J-V curves for p-Si photocathode and GaSb _{0.03} P _{0.97} photoanode.	153

CHAPTER 1

INTRODUCTION

1.1. Global Energy Challenges and the Environment

Up until the onset of the first industrial revolution, and for the last 1 million years the Earth's atmospheric CO₂ concentration has oscillated between 175-300 ppm. In the last 150 years however, the concentration of this greenhouse gas has steadily increased and reached an alarming level of 400 ppm.¹ More importantly, the average temperature on Earth has followed along the trend with record-breaking temperatures seen each year. According to reports issued by the Intergovernmental Panel on Climate Change, The United Nations Framework Convention on Climate Change and the National Aeronautics and Space Administration (NASA), we live in a new geological era – the anthropocene - where human-related CO₂ emissions have changed climate, affecting the lithosphere and ecology on a planetary scale.² 85% of the 16 TW of power consumed globally is supplied by combustion fossil fuels in the form of natural gas, coal, and petroleum raffinates.¹ Energy consumption is expected to increase by 50% in the next 30 years, mostly driven by accelerated economic growth of developing nations. This projection of energy use by the year 2050 has been referred to as the Terawatt Challenge, equivalent to building a new 1GW nuclear power plant roughly every 2 days in order to replace fossil fuel sources. It is common misconception that fossil fuels will be exhausted in the first half of the 21st century, but in fact conservative estimations predict that there are enough

reserves of liquid/gaseous hydrocarbons for at least 200 years and over 1000 years supply of coal to sustain an average consumption growth of $2.3\% \text{ yr}^{-1}$. However, intensive consumption of fossil energy would lead to carbon emissions in the order of 11×10^9 tons yr^{-1} . Therefore, if no carbon sequestration technologies are implemented and generation is scaled up with a business-as-usual approach, at the current rate, in the next 50 years runaway climate change will most likely reach a tipping point threatening our economic system, ecosystems and life on Earth as we know it. While combustion of fossil fuels for transportation, power generation and industrial production account for the majority of the emissions, agricultural activities also generate CO_2 , but to a lesser extent.

Technological innovations leading to the steam engine, power plants and combustion engines emerged to convert chemical or potential energy into work, mainly for the purpose of feeding a growing population, sustaining comfortable environments for us to inhabit, and providing faster means of travelling. Without a doubt, progress of society has historically been related to our ability of making more efficient use of the available energy resources. In the same way, to further improve the quality of life on Earth, future societal development will be contingent on our capacity to adapt for sustainably exploiting the highest, most abundant and safest form of energy available to us which is sunlight.

Today the world needs hydrogen from renewable sources more than ever before to produce ammonia for fertilizers, to hydrogenate hydrocarbons, and as a clean transportation fuel. The greatest technological challenge of our time is, therefore, figuring out a way of efficiently harvesting solar radiation in a decentralized fashion and storing energy for use on-demand so that fossil fuels can be phased out.

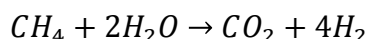
The first and second industrial revolutions led to centralized power generation, and only in the 1970's with the widespread adoption of electricity a new industrial revolution happened bringing about the information age, computer aided design and advanced manufacturing techniques. It's hard to foresee what distributed energy systems will bring from geopolitical, economic and environmental standpoints. It is quite clear, however, that business and research ventures centered on advanced functional materials – at the heart of photovoltaics, photoelectrochemical cells and batteries - will play a major role in the next industrial revolution. Especially, among the known distributed generation systems, photoelectrochemical water splitting appears to be a promising technology for directly converting and storing solar power in the form of chemical bonds as solar fuels for on-demand use.

Indeed, direct conversion of solar energy to fuels is the most feasible and the ultimate route to store energy for on-demand electricity generation. About 1.2×10^{17} W of solar power in the UV-Vis-IR range strike the surface of the earth. While multiple energy conversion schemes (including wind, tidal, hydro, bio, and PV technologies) could all add up to help meet 30 TW of global power demand, only hydrogen production via photoelectrochemical (direct solar) water splitting seems to hold promise at a worldwide scale, as it uses an abundant energy source to produce a carbon-free fuel with little capital investment.³ Yet, the present technological obstacle in this area is the development of inexpensive, highly-efficient semiconductor electrodes to drive the water splitting reactions. DOE has defined as the ultimate target a 25 % solar-to- hydrogen conversion efficiency (STH) for producing hydrogen in photoelectrochemical cells.⁴ To achieve such

a high STH it is required to generate about 20.3 mA/cm² from a photoelectrochemical cell without external bias.

1.2. Hydrogen market: present and future

About 65 million metric tons of hydrogen are produced each year mainly by steam reforming. This chemical process has an overall reaction:



However, this synthesis route depends on non-renewable sources and it is inherently environmentally offensive as it releases massive amounts of CO₂.⁵

While electrolytic synthesis of H₂ represents a minor portion of the hydrogen produced worldwide, large plants with a 6 MW capacity have already been commission in Germany to balance the load in rapidly changing output of renewable generation systems.⁶

At present, H₂ has a market size of over 150 billion dollars, as it is widely used as commodity in hydrotreatment of bulk petrochemicals, to produce naftas, jet fuel and gas oil, gasoline, and in the Haber process for production of ammonia. H₂ is an extremely flexible commodity commonly used as process gas in semiconductor processing, in the synthesis of industrial chemicals like methanol, in metallurgy, in the glass and food, fat and aerospace industry.⁷ These established smaller-scale industrial applications are interesting markets for hydrogen produced decentrally where production cost becomes competitive with retail prices. Due to the increasing industrial demand and potential use as a transportation fuel, the hydrogen market is expected to grow rapidly in the next 20

years with the fast deployment of fuel cell hybrid electric vehicles, such as the Nissan Leaf, Honda's Clarity, Toyota Mirai, GM's HydroGen4 and Mercedes-Benz F-cell car, among others.

In the US, the adoption of fuel cell technologies in emerging markets is currently driven by DOE's market transformation program. The goal of this program is to accelerate the expansion of hydrogen and fuel cell use by reducing the barriers that are holding back full technology commercialization. This strategy has resulted in the deployment of thousands of fuel cells that are now demonstrating the use of clean energy technologies to reduce CO₂ emissions and the use of petroleum while increasing energy security. Material handling equipment, emergency backup power, mobile generation, maritime, and cargo equipment applications of fuel cells are examples of fruitful collaboration between industry stakeholders and the Office for Energy Efficiency and Renewable Energy (EERE) where federal support has catalyzed the market to achieve economic benefits.⁸

1.3. Photoelectrochemical water splitting

Photoelectrochemical water splitting cells are artificial photosynthetic devices that harness the energy of sunlight and directly convert it into energy-dense chemical bonds that can be used as fuels. All solar fuels generators depend on an electrical asymmetry to direct photogenerated charges in separate directions to oxidize or reduce some chemical species, like water, and isolate the chemical products. The required separation can be driven by either electrochemical potential differences or kinetic asymmetries at the junction between two different materials.⁹ The PEC half-reactions on semiconductors are

driven by photoexcited minority carriers.¹⁰ An example of the simplest configuration, with a single photoabsorber water splitting cell, is shown in Figure 1.1a.

Figure 1.1.a shows a schematic of a PEC with an n-type photoelectrode where the oxygen evolution reaction takes place at the semiconductor-electrolyte interface. The other half reaction, where H₂ is produced, occurs at a counter electrode with low overpotential, such as platinum. In this configuration H⁺ ions produced as a byproduct of oxygen evolution, diffuse through the solution towards the counter electrode to supply protons for the half reaction that takes place at the cathode.

In an alternative configuration (

Figure 1.1b), that is equally simple as the one described previously, a p-type photocathode is used to absorb sunlight but the hydrogen evolution reaction occurs on the working electrode, i.e. on the p-type absorber, and the other half reaction takes place on the counter electrode selected to have a low overpotential for oxidation of water, such as iridium oxide.

These previously mentioned configurations can be combined into a single device that absorbs sunlight of different wavelengths on each of the electrodes. Such a device having two photoabsorbers is referred to as a wired Z-scheme dual semiconductor photoelectrochemical cell (

Figure 1.1c). In practice, it is desirable to keep the evolving gases separated in different containers, as shown in Figure 1.2 to avoid a mixture of explosive gases and to be able to carry out the half-reactions at different pH values.

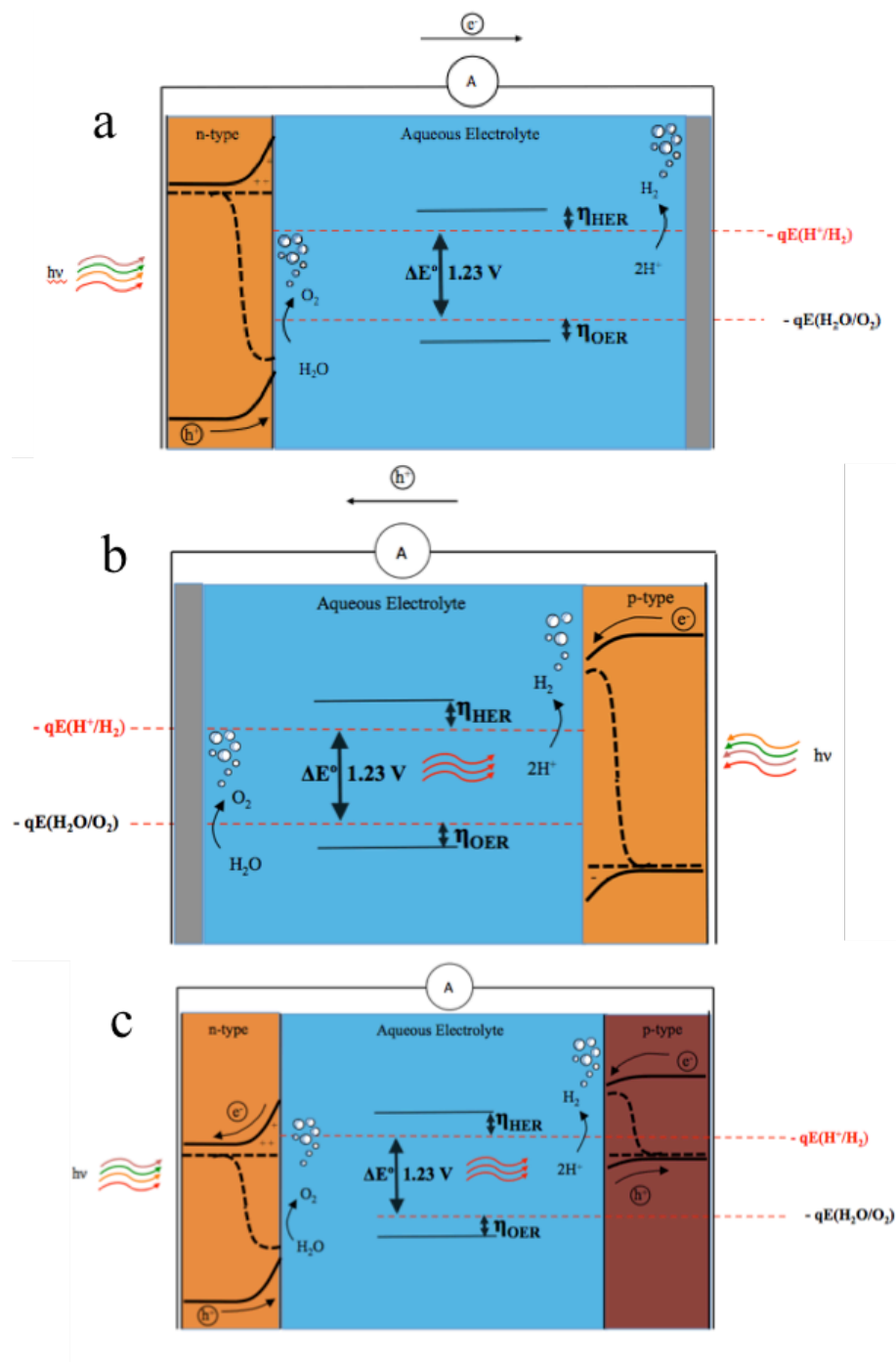


Figure 1.1. Three different photoelectrochemical water splitting cell configurations, a) n-type semiconductor is driving the reactions, b) p-type semiconductor is driving the reaction, c) both electrodes absorb radiation of different wavelengths to drive the water splitting half-reactions.

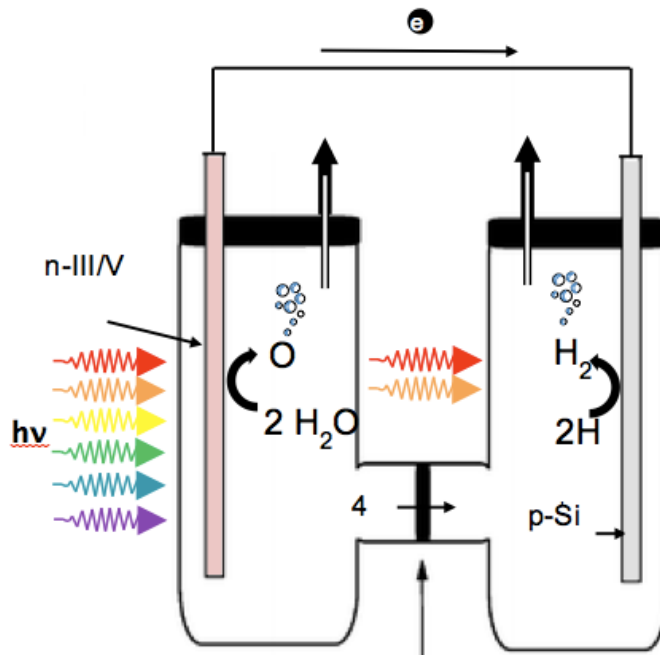


Figure 1.2 Wired dual semiconductor photoelectrochemical cell with separate reaction compartments.

1.3.1 Material requirements for water splitting

From a thermodynamic standpoint, under standard conditions only $E^\circ_{\text{cell}}=1.23 \text{ V}$ or $\Delta G^\circ = +237.2 \text{ kJ mol}^{-1}$ are necessary for water splitting if there are no major energy losses; in reality these are un-avoidable as in any energy conversion system.¹¹ The maximum power that could be converted with a material having that absorption wavelength cut-off of 1008 eV based on the standard AM1.5g illumination is given by expression:

$$P_{\text{total}} = A \int_{300}^{\frac{1240}{E_g}=1008} I(\lambda)_{\text{AM1.5g}} d\lambda$$

Assuming 100% quantum conversion efficiency the maximum attainable solar-to-hydrogen efficiency, η_{STH} , would be about 47%. However, there is a significant entropic energy loss associated with the work that needs to be done to extract the excited photogenerated carriers. The chemical potential of the excited state, $\Delta\mu_{ex}$, determines the amount of useable photopotential that can be generated in a single semiconductor photoelectrochemical cell. As we will see later, the amount $\Delta\mu_{ex}$ is considerably smaller than the band gap magnitude, and it is equal to the difference between the quasi-Fermi levels of the semiconductor under intense illumination, and to the open circuit voltage in the flat band condition for an ideal semiconductor.^{5,11} In practice, the chemical potential is at best $\Delta\mu_{ex} = 0.75 E_g$. The energetic overpotential for driving the half-reactions at a reasonably high current density (to obtain a commercially viable production rate) is about 0.2-0.4 eV even using some of the best catalysts available.

This means that the minimum possible band gap to compensate for the entropic energy losses and kinetic overpotentials for a single semiconductor cell is, $E_g = (1.23 + 0.2)/0.75 = 1.9 \text{ eV}$, to carry out water splitting at a nominal current densities between 10-20 mA cm^{-2} . Since a semiconductor having a band gap of 1.9 eV will only absorb light with wavelengths smaller than 652 nm, a significant portion of the integrated solar spectral irradiance cannot be harvested because it presents at smaller energies. (Fig 1.4a) Another loss stems from energy wasted to thermalisation of hot carriers relaxing to the conduction band edge from elevated energy levels above the conduction band (Fig 1.4b); this phenomenon accounts for a substantial portion of the energy lost as heat which cannot be stored as chemical bonds in a solar fuel.¹²

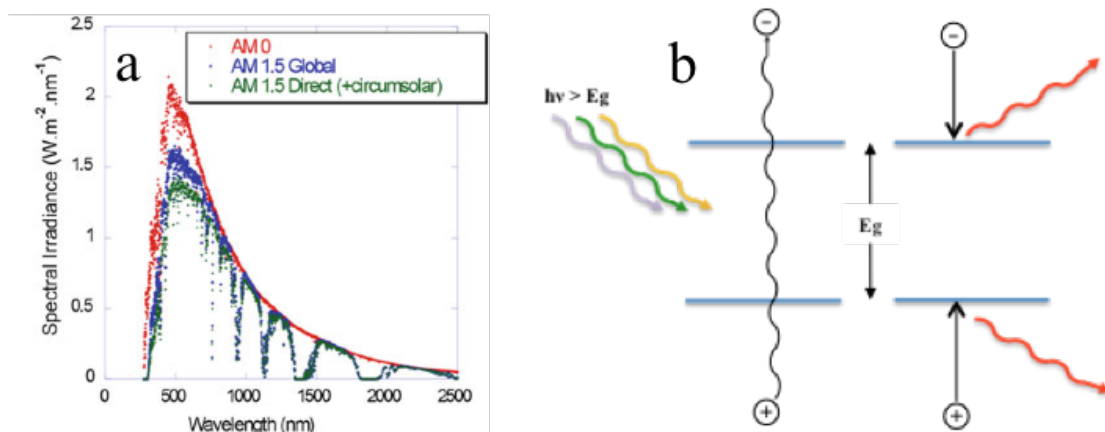


Figure 1.3 a) AM 0, AM 1.0 global and AM 1.5 direct spectra using ASTM data. Adapted from Chen et al.¹³ B) Hot carrier thermalisation with above band gap illumination.

Clearly the upper limit for the absorber band gap is defined by the highest spectral irradiance energy of AM1.5g radiation, which peaks at around 500nm and drops substantially in the ultraviolet. Thus the optimal band gap lies somewhere between 1.9 and 2.5 eV. Therefore, in order to maximize solar radiation absorption and avoid thermalisation at visible wavelengths, to achieve efficiencies beyond 15% the band gap of the semiconductor material should be between 1.9 ~ 2.2eV.^{5,11}

Having quasi-fermi levels that also straddle the redox potentials for water splitting (plus the overpotentials) is a requirement that has been vastly understated in the literature. The extent of separation of the quasi-fermi levels is particularly important to determine how much useable photopotential can be generated in a single semiconductor photoelectrochemical cell. This is analogous to the observed photovoltage in silicon photovoltaic cells: the band gap of Si is 1.12 eV but the open circuit voltage of a single junction cell typically is in the order of 0.6-0.7 V. In other words, while the

semiconductor band-diagram representations reflect the internal energy of holes and electrons, they do not represent the useable energy.

In fact, it is often mis-represented that a material with a band gap that straddles the redox potentials can split water. However, if the hole quasi-fermi level is too negative, i.e. above the OER potential, then the hole potential for driving the water oxidation reaction is not enough, and in this case water splitting is not possible.¹⁴ This condition is represented in Figure 1.5 below:

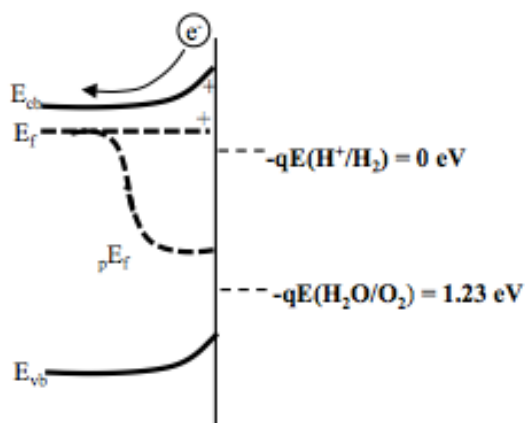


Figure 1.4 Band diagram of a n-type semiconductor under illumination with hole quasi-fermi level too negative (above) the OER reaction potential.¹⁴

1.3.2 Material Challenges

All known materials come short of un-assisted water splitting due to, at least, one of the following observations: a) being unable to absorb the necessary wide-range of sunlight wavelengths, b) having thermodynamically inadequate band alignment with respect to HER and OER redox potentials, c) generating insufficient photovoltage to separate the quasi-fermi levels, d) suffering from photocorrosion/passivation, e) having unfavorable planar surfaces, f) presenting defective structures that limit transport and collection of carriers by recombination, g) exhibit sluggish redox kinetics, and h) undesirable native conductivity type for a photoanode.^{9,15} While the issue of slow interfacial charge-transfer kinetics can be addressed by incorporating proper electrocatalysts, the remaining challenges are essentially all tied to inherent material properties, namely, band gap, work function, carrier concentration, electron affinity, absorption coefficient, absorber redox potential, crystallinity and solid morphology.

1.4. Proposed approach

As mentioned earlier, the key requirement for single semiconductor water splitting using visible light-absorbing materials is that the valence band edge and hole *imref* should be more negative than the oxygen evolution reaction with enough overpotential. It has been shown that the band gap of GaN can be reduced to 1.8 eV from 3.45 eV by alloying it with antimony less than 8 at%.¹⁶ The valence band edge of the resulting polycrystalline $\text{GaSb}_x\text{N}_{(1-x)}$ alloys with 1.9 eV band gap has been shown to straddle the oxygen evolution reaction. Such a material is, at first glance, theoretically well suited as an anode in the proposed device for unassisted water splitting with high photocurrents ($>18 \text{ mA/cm}^2$ or $\sim\text{STH}$ of 20%).¹⁷ The key challenge is to grow good quality

material cost effectively on p-type Si substrates. Similarly, alloying of GaP with antimony can be used to produce $\text{GaSb}_x\text{P}_{1-x}$ semiconductors. GaP is an indirect band gap semiconductor with its conduction band edge located much further negative of the hydrogen evolution reaction potential.

Here, the approach is engineering the band structure of n-type $\text{GaSb}_x\text{N}_{1-x}$ and $\text{GaSb}_x\text{P}_{1-x}$ alloy semiconductors to enhance opto-electronic properties such as visible light absorption, carrier lifetime and mobility of GaP and GaN when alloyed with Sb, as shown in Figure 1.5.

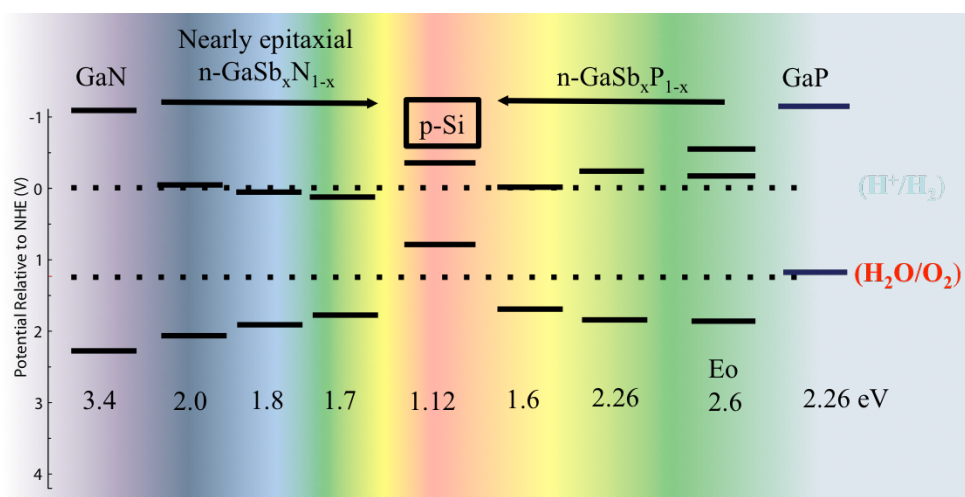


Figure 1.5 a) Band engineering of III-V alloys towards direct water photoelectrolysis

However, the major limitation is that these n-type $\text{GaSb}_x\text{P}_{1-x}$ alloys with band gaps lower than 2.0 eV may not be able to straddle oxygen evolution with enough overpotential. So, a device incorporating a direct band gap $\text{GaSb}_x\text{P}_{1-x}$ alloy semiconductor with 1.8 eV gap as anode and p-type Si as photocathode can achieve up to 15% STH with unassisted water splitting. The theoretical efficiencies of dual absorber cells are taken from reference.¹⁸ A 1.8 eV band gap, n-type $\text{GaSb}_x\text{P}_{1-x}$ will need a Si counter photoelectrode to provide bias for achieving photoelectrochemical water splitting. So, the overall economic model involving low cost manufacturing of high quality layers could make this device potentially competitive for producing hydrogen less than \$4/Kg.¹⁹

Conceptually, to meet the ultimate target of 25% STH efficiency, a water splitting PEC design incorporating novel III-V's and inexpensive silicon would consist of a monolithic photocathode + photoanode (Z-Scheme) architecture, where Si and a III-V semiconductor are connected back-to-back through a transparent ohmic junction (Figure 1.6a). The anode side is protected by one or more passivating layers and decorated with an oxygen evolution co-catalyst. The cathode side is functionalized with hydrogen evolution catalyst. As the two gases are produced separately on either side of the system, an ion-selective membrane should permit the diffusion of H^+ ions from the anode to the cathode, while preventing the crossover of produced gases through diffusion of dissolved gases (or bubbles) to the opposite side of the cell to prevent mixtures of explosive gases. This design is ideal for distributed power generation such as in the developing world, remote areas, new off-the-grid development, and domestic generation of H_2 for use in transportation fuel cells. An alternative conceptual embodiment consists of light-driven suspended particle reactor with anisotropically functionalized photoabsorber particles, such as III-V materials to produce H_2 and O_2 in a continuously stirred vessel. (Figure 1.6b) This design is better suited to be part of a centralized system such as H_2 generation at a plant-scale level in a refinery or ammonia synthesis facility. Each of these embodiments has their own advantages and limitations, as well as different scientific and engineering challenges that have yet to be solved. Some of outstanding problems are the subject matter and specific goals of this work.

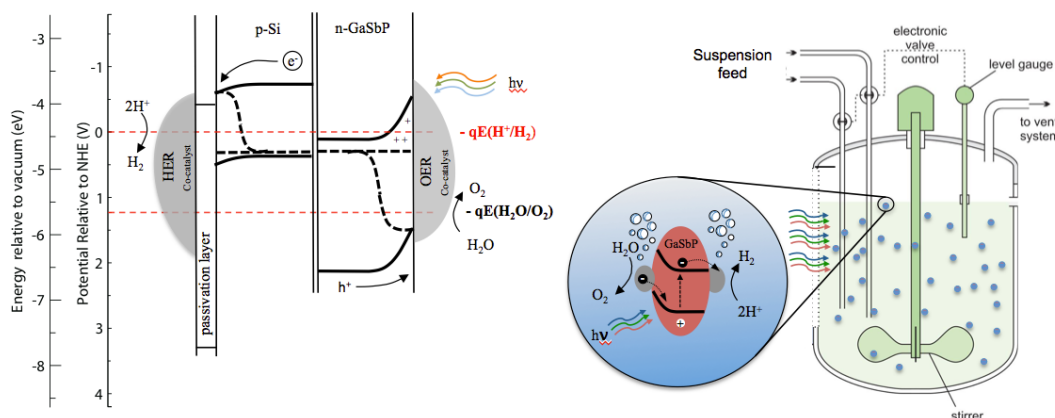


Figure 1.6 a) Monolithically integrated Photoanode+Photocathode design for distributed H_2 generation, b) Light-driven suspended particle water splitting reactor for centralized H_2 production.

In both concepts, the only feedstock materials to produce hydrogen in the cell on a sunny day are water and possibly a buffer solution on each half-reaction compartment to maintain the pH at an optimal value for stable operation. The only energy input to the system is sunlight itself.

In summary, this study involves the development of n-type $GaSb_xN_{1-x}$ and n-type $GaSb_yP_{1-y}$ alloy semiconductors towards implementation in z-scheme fashion with p-type Si or Cu_2O photocathodes to produce highly efficient, unassisted water splitting system. As discussed later, the above materials can be grown using halide vapor phase epitaxy (HVPE) technique at high growth rates, low cost and high crystallinity (with >100 micron domain sizes). The durability of the photoanode materials for short periods is not found to be an issue. However, the long-term durability will need to be addressed through the use of protective layers. The proposed III-V alloy materials and the proposed device structure and their growth techniques make them as attractive to overcome the limitations associated with Turner's tandem cell using GaAs PV and $GaInP_2$ semiconductor electrode.²⁰

1.5. Objectives of this study

The main goal of this project is the growth of epitaxial or nearly epitaxial III-V films based on $\text{GaSb}_x\text{N}_{(1-x)}$ and $\text{GaSb}_x\text{P}_{(1-x)}$ towards developing a stable photoelectrochemical (PEC) water splitting cell capable of un-assisted photoelectrolysis at 15% STH efficiency, comprising a single semiconductor or a photoanode+photocathode configuration based on these new III-V materials and earth-abundant semiconductors as silicon or Cu_2O . An objective of this dissertation is to discuss the technological aspects related to the incorporation of Antimony in epitaxial films of $\text{GaSb}_x\text{N}_{(1-x)}$ grown at high temperatures.

The specific objectives of the proposal are the following:

1.5.1 Specific Objectives

- a) Improve the quality of synthesized materials through epi-growth for $\text{GaSb}_x\text{P}_{1-x}$ and single crystal $\text{GaSb}_x\text{N}_{1-x}$ alloys.
- b) In the Sb low-incorporation regime, fundamentally understand what concentration of Sb will narrow the bands to a degree where the band edges no longer straddle the redox potentials of water splitting half reactions and start introducing mid-gap states.
- c) Study the fundamental optoelectronic properties of $\text{GaSb}_x\text{P}_{1-x}$ and $\text{GaSb}_x\text{N}_{1-x}$, specifically its work function and absorption coefficient to enhance the understanding of processes such as carrier generation and transport to the solid-electrolyte junction.

- d) Investigate the band structure of the alloys in relation to the photoelectrochemical characteristics of photoanodes based on these III-V materials.
- e) Discuss protection and enhancement strategies for the intrinsically unstable semiconductor p-Cu₂O.
- f) Carry out a preliminary evaluation of a proof of concept for un-assisted water splitting using n-GaSb_xP_{1-x} and p-Si.

1.6. Organization of thesis

This dissertation consists of 8 distinct chapters.

Chapter 1 presents a motivation to study and develop materials and devices for photoelectrochemical water splitting in the context of current energy and environmental challenges. An introduction to the fundamentals of water splitting, including the working principles of this technology are reviewed along with the physicochemical constraints of the system that need to be considered for designing functioning device to hydrolize water using only the energy input of sunlight. Additionally, the challenges associated with the material properties for absorbing visible light, and spontaneously driving the redox reactions in a stable and efficient way are considered. The proposed approach to solving these challenges and the objectives of the study are set forth in the introduction.

Chapter 2 presents a review of techno-economic analysis of the systems under study, and a comprehensive review of the state of the art of materials for water photoelectrolysis. Relevant growth techniques to fabricate single crystalline semiconductors are discussed.

Chapter 3 presents an overview of the experimental methods and materials employed in this study, including specifics of III-V growth methodologies, instruments and data analysis procedures for determination of key optical, physical and chemical characteristics of the samples. The main electroanalytical chemistry tools and techniques for assessing the performance of the materials are discussed.

Chapter 4 presents work done with anteriority to the main subject matter of this dissertation (III-V films), to enhance the photoactivity of another well known semiconductor Cu_2O . This work is an example of the importance of gaining good control over the chemical composition of semiconductors, through processing techniques to extend the durability of unstable photoabsorbers and also improve charge separation at the solid-liquid interface by means of p/n junctions.

Chapter 5 presents the results of metalorganic vapor deposition experiments for fabrication of GaSbN films and electrochemical performance thereof.

Chapter 6 presents the results of experiments leading to growth of $\text{GaSb}_x\text{P}_{1-x}$ by halide vapor phase epitaxy. Discussion of the inter-relationship between processing, material structure and relevant opto-electronic properties is provided.

The conclusions from the study and recommendations are included in chapter seven and eight, respectively.

CHAPTER 2

BACKGROUND

2.1. Introduction

In this chapter the state of the art of water splitting materials is examined by semiconductor class. A review of the thermodynamic fundamentals of PEC and the techno-economic aspects of production of hydrogen by PV powered electrolyzers versus PEC are presented. A classification of different PEC architectures is presented along with the most relevant examples that have lead to high-performance devices, and the advantages and drawbacks of each type of device are considered. This chapter puts the present work into context, and provides a rational for focusing on III-V materials which happen to be among the best performing semiconductors to date. Finally, key aspects of heteroepitaxy and crystal growth are put forth.

2.2. PEC water splitting fundamentals

Band bending at an ideal semiconductor-liquid junction is analogous to band energetics at the interface of a semiconductor and a metal. Initially, before the solid semiconductor comes in contact with the liquid, the Fermi level E_f of the n-type SC is separated from the electrochemical redox potential, μ , of the solution by certain value $\phi_{sln} - \phi_{sc}$ (Figure 2.1a). When the solid comes in contact with the liquid, this potential imbalance forces electrons in the conduction band to drift towards the SCLJ

(semiconductor liquid junction) in order to equilibrate the Fermi level and the electrochemical potential, thus establishing an electron depletion region with upward band bending in the semiconductor (Figure 2.1b). In the dark, the concentration of holes is much smaller than that of electrons (in the case of an n-type material) and a potential barrier prevents transfer of electrons from the solution to the conduction band, that is, the oxidation of water is thermodynamically impossible. When photons more energetic than the band gap, E_g , of the semiconductor strike the surface, they are absorbed, and metastable excess holes h^+ are created. Under steady illumination, the optical electron-hole pair generation rate is added to the thermal generation, thus the carrier concentrations n and p will increase to new steady state values. This departure from equilibrium caused by optical excitation defines excess carrier concentrations δn and δp . Therefore, with respect to the population of carrier in thermal equilibrium, the excess hole population significantly affects the total minority carrier concentration, whereas the alteration of the total majority carriers caused by the excess electrons is negligible. In other words, while the percentage change in the majority electron concentration is minute, the majority carrier concentration changes several orders of magnitude. With the addition of sunlight, the quasi-Fermi level splits because of the excess concentration of holes, and shifts substantially compared to the electrons quasi-Fermi level. Oxidation of water becomes feasible under illumination as electrons forming the bonds in water are transferred to the valence band (exo-energetic process) of the semiconductor.²¹ In this process, positive particles (holes) moving towards the junction are consumed. With enough light power the bands can become completely un-bent, defining the flat band potential, E_{fb} (it is the energy level of the conduction band). Illumination separates the

Fermi level from the electrochemical redox potential of the solution by an amount V_{oc} (photovoltage) of the semiconductor in that particular electrolyte (Figure 2.1c). A reverse biased n-type (working electrode biased positively with respect to the counter electrode) will bend the bands (from the flat band situation) in the opposite direction as the illumination (Figure 2.1d).

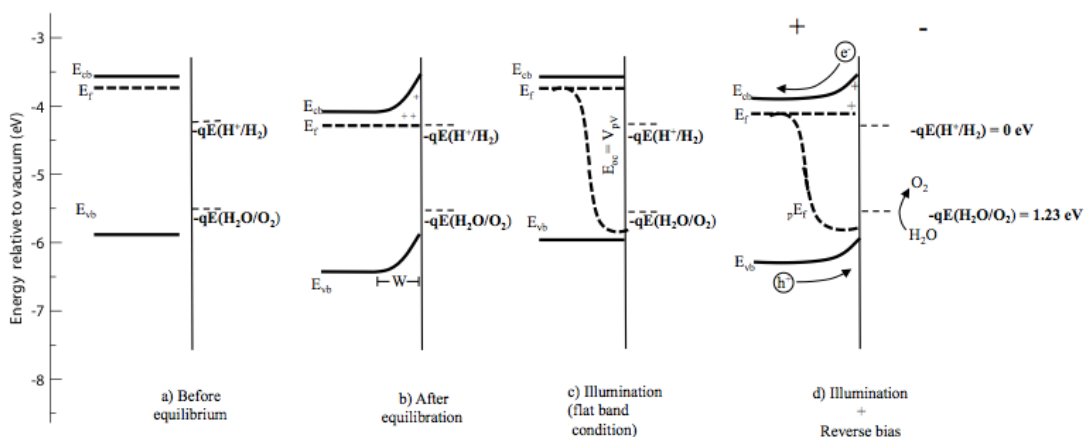
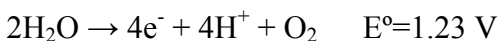


Figure 2.1. Band energetics of an n-type photoabsorber in contact with an aqueous electrolyte.

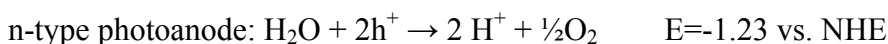
Adapted from **Lewis et al.**²²

In this condition, where there is a high concentration of holes and band bending creates a built-in electric field near the junction, photogenerated carriers can be separated; electrons drift toward the back contact, whereas holes are swept towards the semiconductor liquid junction and recombine with electrons coming from an oxidation reaction, such as:



In principle, in a n-type material if the conduction band is more negative than the hydrogen evolution potential and its valence band edge is more positive than the oxygen

evolution half-reaction potential, majority carriers could go around the circuit to a counter electrode and into the solution to carry out proton reduction. The following half-reactions illustrate the concept of water splitting in a full cell:



TiO₂ and some binary III-Nitrides have energy bands that straddle the water-splitting chemical potentials and withstand photocorrosion under photolysis conditions^{23,20}, however they have band gaps > 3.0 eV. In addition, for unassisted water splitting the photo-electrode material must exhibit: (a) quasi-Fermi levels straddling the redox reaction potentials plus their kinetic overpotentials; (b) fast electrochemical reactions to reduce surface charge build-up; (c) low bulk and surface recombination from defect states; and (d) fast charge carrier mobility.

2.3. Review of techno-economic analysis

The baseline for a techno-economic analysis of PEC water splitting can be defined in terms of the operating cost of producing hydrogen electrolytically, particularly with PEM cells, as this is a well-established technology. Their efficiency is commonly referred to the specific electrical energy requirements for electrolysis. State-of-the-art electrolyzers present values as low as 47 kWh kg⁻¹ at nominal current densities of 1.5 mA cm⁻².²⁴ Assuming an average cost per kWh in the U.S. of 12 cents, one can estimate the cost of Hydrogen at around 5.6 \$ kg⁻¹. This figure is just about twice the cost of gasoline since the energy density of H₂ (used in a fuel cell) is comparable to that of gasoline in an internal combustion engine, between 500-1000 kJ kg⁻¹. In real life, this means that for the

same money, a driver can travel at least half of the range if he or she chooses to change their IC car for a HEV running on electrolytically produced H₂. In reality, the cost of hydrogen per kg is about US\$10 kg⁻¹ assuming an installation cost of \$2 per watt.²⁵ US\$5.7 kg⁻¹ is precisely the U.S. DOE target for 2020 for PEC hydrogen with an average STH of 20%. The specific energy cost of modern electrolyzers mentioned earlier, corresponds to an electric-to-chemical conversion efficiency of 83.8%. If a commercial PV panel with efficiency of 20% powered the optimized electrolyzer, a net efficiency of 16% percent should be achievable. Recent techno-economic studies done at NREL put the cost of electrolytically produced hydrogen (powered by wind farms) very close to the cost of the steam reforming method.²⁴

For both scenarios, PV+electrolysis versus direct PEC water splitting, the capital costs should be equivalent in order for the above analysis to make sense. A technical and economic feasibility assessment of facilities for solar hydrogen production via PEC done in 2013 concluded that the manufacturing cost of fixed-panel PEC cells with 10% efficiency and a 10-year lifetime must be less than US\$ 100 m⁻² in order to be compete with the PV+electrolyzer approach.²⁶

In 2016 Lewerenz and Atwater²⁷ published a study on the efficiency limits of single junction (and dual junction) PEC water splitting cells based on a model that takes into account the multicomponent nature of the devices including the semiconductor absorption fraction, external radiative efficiency, series and shunt resistance as well as catalytic exchange current. Their conclusions suggest that the maximum possible STH efficiency in high-performance realistic case would reach 15.1% with a semiconductor having a band gap of 2.05 eV. When the scenario includes only earth-abundant elements

this figure drops to 5.4% for a semiconductor with $E_g = 2.5$ eV. For the dual solid-liquid junction cell, the high-performance STH reaches 28% with top and bottom absorbers of 1.6 and 1 eV, respectively. In the more conservative scenario, the maximum efficiency was predicted to be 16% with materials of band gap 1.9 and 1.4 eV, respectively.

This analysis suggest that even if a holy-grail semiconductor was discovered, its efficiency in a single semiconductor PEC cell would at best match that of PV+PEM electrolyzer configuration.

On the other hand, dual junction cells show more potential for surpassing the efficiency baseline set by PV driven PEM electrolytical cells. However, the capital cost of a high-performance dual junction cell needs to be reduced so that it can be amortized through cost savings during the lifetime of the cell, that is, assuming a lifecycle of over 10 year.

2.4. State of the Art on Water Splitting

2.4.1. Taxonomy of solar energy conversion systems

Solar energy conversion systems can be classified based on whether they are fuel-forming devices or not. Solid-state photovoltaic cells typically comprise one or more p-n junctions and only create an external flow of electrons that does work on a load, but do not directly carry out electrochemical reactions on the semiconductor surface. These can be used in conjunction with electrolyzers (as the load) in order to store energy in the form of fuels (as discussed in Section 2.1). This combination is generally referred to as PV-biased electrosynthetic cell, an example of which is the PEM cell for hydrogen production.

Another category is the photoelectrosynthetic particulate system, where an anisotropically functionalized photoabsorber suspension or slurry of semiconductor particles are exposed to sunlight through a transparent medium for synthesis of H_2 . Out of all energy conversion devices photocatalytic water splitting with semiconductor slurries has the greatest scalability potential and appears to be the most economically viable large scale solution. The state of the art in particulate reactors is spearheaded by $SrTiO_2$ and $BiVO_4$ doped with La, Rh and Mo with conversion efficiencies of 1.1%²⁸

Photoelectrochemical cells can be divided into four categories as shown in Figure 2.2, namely, photoelectrosynthetic PEC cells, electrocatalytic cells, PV biased PEC cells and regenerative cells.

Only the first 3 systems on this list are fuel-forming devices, while regenerative cells exclusively generate electricity. Nonetheless, they're considered photoelectrochemical cells because they absorb light, and their functioning principle relies on a cyclic oxidation and reduction of a species in an electrolyte to shuttle carriers between the cathode and the anode. Dye-sensitized solar cells are a good example of regenerative PEC cells.

In photoelectrosynthetic PEC cells the oxidation and reduction reactions are carried out directly on the surface of one or more semiconductor(s) (or on a co-catalyst) and by definition have a semiconductor-liquid junction. In this kind of cell all the driving force comes from potential gradients in the semiconductors to carry out non-spontaneous reactions like water splitting. Honda and Fujishima's TiO_2 based device was the first recorded example of a photoelectrosynthetic PEC cell. Electrocatalytic cells carry out

reactions that are spontaneous, with a positive E° cell, but sunlight assists in catalyzing the rate of reaction.

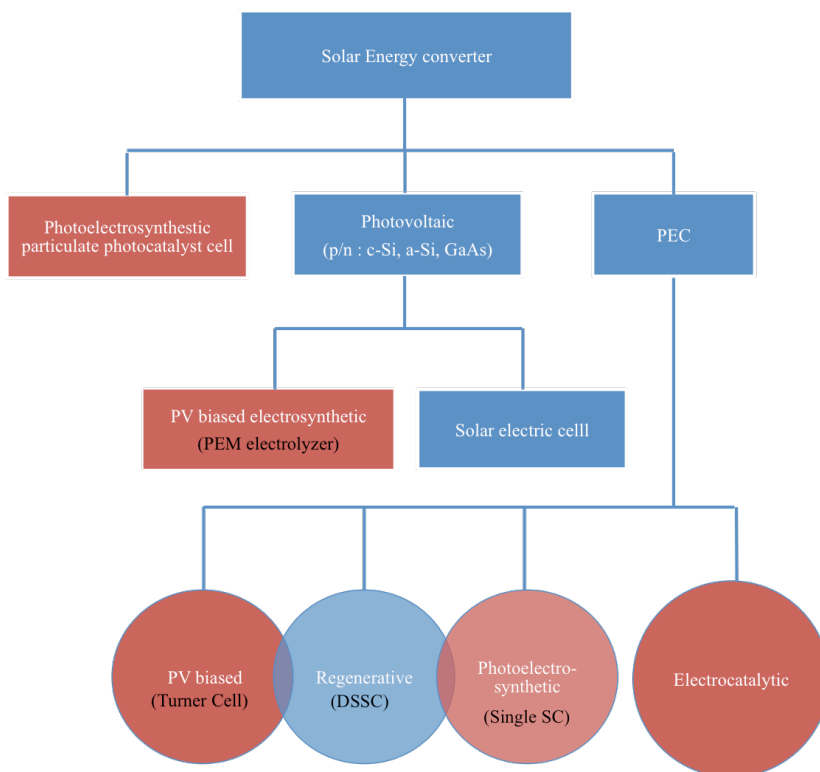


Figure 2.2 Simplified taxonomy of devices for solar fuels generation. (Adapted from Lewis et al.⁹)

Practically speaking, conceiving a PEC water splitting device based on a single semiconductor-liquid junction with stable STH efficiency over 10% has proven to be unattainable thus far, however at least theoretically there exists the possibility that a single semiconductor material could possess the optimum band-gap, conduction and valence band levels, stability, availability and low cost will be discovered.^{5,11}

In the absence of such a material, alternative PEC architectures have been proposed in the past four decades to harvest a broader portion of the spectrum with multiple photoabsorbers in tandem, or increasing the photovoltage of the cell by

incorporating multi-junction PV cells in monolithic electrode designs. These kinds of devices are classified as a PV-biased photoelectrochemical cell.

Other hybrid configurations incorporating regenerative cells, built-in solid-state and solid-liquid junctions have been proposed in an attempt to find a good compromise between complexity/cost and efficiency.

2.4.2. Single Semiconductor photoelectrochemical cells

For many years after Fujishima and Honda's groundbreaking discovery of water splitting using TiO_2 as a photoanode, the search for a single semiconductor able to do unassisted water splitting on its own, was mainly an effort of screening potential candidates among known materials that was centered on finding a common physical denominator: a wide enough band gap to straddle the reaction potentials. However, this finding proved to be elusive perhaps due to the oversimplified assumption that the band gap energy directly corresponded to the free energy available for driving the HER and OER reactions.²⁴

In fact due to the poor performance of the great majority of single semiconductor PEC cells and also due to the lack of standardized testing protocols and figures of merit (only developed in the last couple of years), most publications rarely present STH values, and typically only report their maximum photocurrent at rather arbitrary bias, sometimes neglecting to express the illumination conditions. Compiling intelligible information regarding STH values is almost impossible because it does not make any sense to compare current densities at different bias values and pH conditions. In the best cases, only biased IPCE data and rarely ABPE information can be found. It comes as no

surprise the lack of review papers on single semiconductor PEC cells. By comparison, the literature on Z-scheme architectures and tandem cells (with 2 junctions) more consistently reports STH values.

2.4.3. Tandem Cells

The solar-to-hydrogen efficiency (STH) of verified data was compiled by the author of this manuscript into the color coded contour plot shown in Figure 2.3. Figure 2.3 The horizontal and vertical axes of the plot show the top and bottom band gaps of z-scheme and tandem PEC cells. For comparison, some data points on single semiconductor PEC cells, are presented at the very bottom of the plot, because in a single semiconductor cell, the band gap of the Pt counter electrode is essentially zero, and does not absorb sunlight.

At first glance, it is clear that the devices having two WBG semiconductors present small STH values. As the band gaps shrink, one can find devices with higher Efficiency clustered around the central portion of the plot.

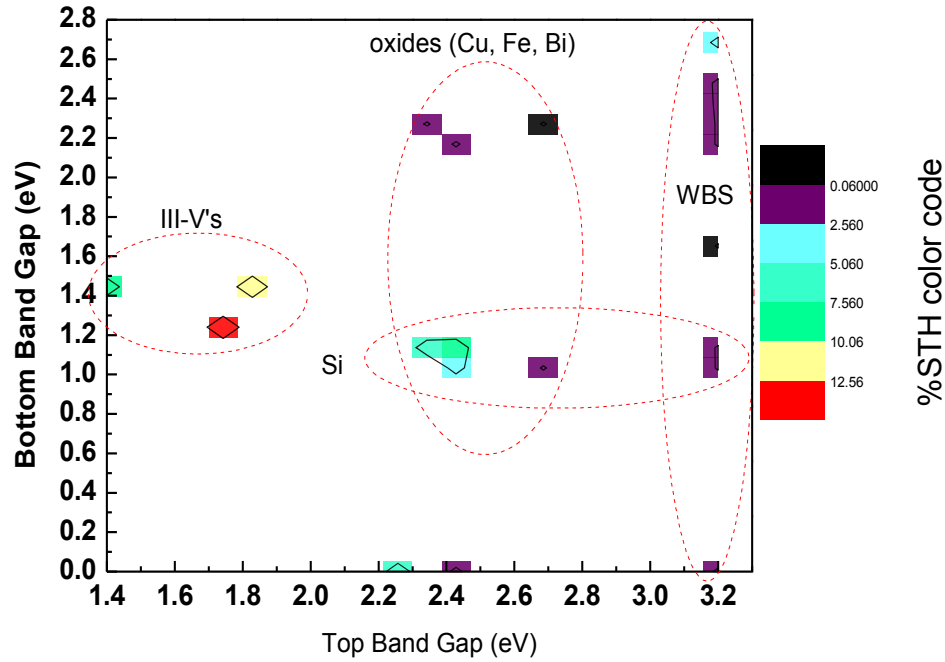


Figure 2.3 Contour plot of reported solar-to-hydrogen efficiency with single semiconductor and 2-Junction PEC Cells.^{20,29-40} The STH values range from 0.06 to 14% represented by color scale on the right.

In the bottom band gap axis of this diagram a big fraction of the data points are grouped around 1.1 eV and 2.3-2.4 because the state-of-the-art dual junction (2J) PEC heavily rely on silicon and wide band gap semiconductors like Cu_2O and BiVO_3 and to a smaller extent on TiO_2 . Among the 2J diagram, the III-V based cells stand out for their efficiencies over 10%. The more relevant examples are discussed in detailed in section 2.4.

2.5. Review of materials and their performance in un-assisted water splitting

Multiple semiconductors have been studied as photoelectrodes for production of solar fuels. These include simple elements like silicon and germanium, binary compounds especially the chalcogenide series (TiO_2 , Fe_2O_3 , Cu_2O , WO_3 , ZnO , SnO_2 , CdS , CdSe , CdTe , WSe_2), group III-V semiconductors (GaN , GaP , InP , GaAs , GaSb , InN , AlP , AlAs); and silicon carbide. Additionally, extensive works have looked at some ternary and quaternary compounds including III-V alloys (InGaN , InGaP , InGaAs , AlGaAs , GaAsP , GaPN , GaSbN , GaSbP), ternary oxides (BiVO_3 , TaON , CuWO_4 , SrTiO_2), and I-III-VI type compounds like CIGS and CZTS.⁴¹ Very recently perovskites (e.g. $\text{CH}_3\text{NH}_3\text{PbI}_3$) have started to be considered for water splitting, but a successful implementation of these is questionable since they typically undergo decomposition in humid environments.⁴²

2.5.1. Narrow band gap semiconductors.

Silicon and Germanium have band gaps of 1.12 and 0.8 eV, respectively. Consequently they cannot be implemented into a single semiconductor PEC cell, however Si is a ubiquitous and earth-abundant semiconductor, that presents adequate band edge energetics for use as a photocathode in a Z-scheme architecture with GaP.⁴³ Conformal pinhole-free barriers can cathodically protect silicon against passivation and has shown that it can operate at 30 mA cm^{-2} .⁴⁴⁻⁴⁶ For example a metal-insulator-semiconductor PEC photocathode comprising p-Si| SrTiO_3 |Ti|Pt achieved an STH of 4.9% and over 35h of continuous operation. Similar corrosion protection strategies with ultra-

thin insulating films have been successfully implemented by ALD with TiO_2 , Al_2O_3 , NiO_x , and even with native SiO_2 .¹⁵

The major drawback of narrow band gap semiconductors (Si, InP, GaAs) for dual cell PEC is their fundamental instability caused by photocorrosion and passivation in aqueous environments. This is especially true for narrow band gap n-type semiconductors because they have thermodynamic oxidation potentials above the OER redox potential. This results in self-oxidation and formation of an insulating layer at the liquid interface when implemented as photoanodes.¹⁵

Chen and Wang have reviewed the stability of multiple semiconductors in aqueous solution. Figure 2.2 is a useful tool to assess the stability of both photocathodes and photoanodes at pH 0. For example, for a photoanode, photogenerated holes will oxidize the material itself if its oxidation potential is below the OER potential or its valence band maximum. It is important to notice however the redox potentials, and the flat band potential for each half reaction and material shift according to Nernst equation as a function of pH.

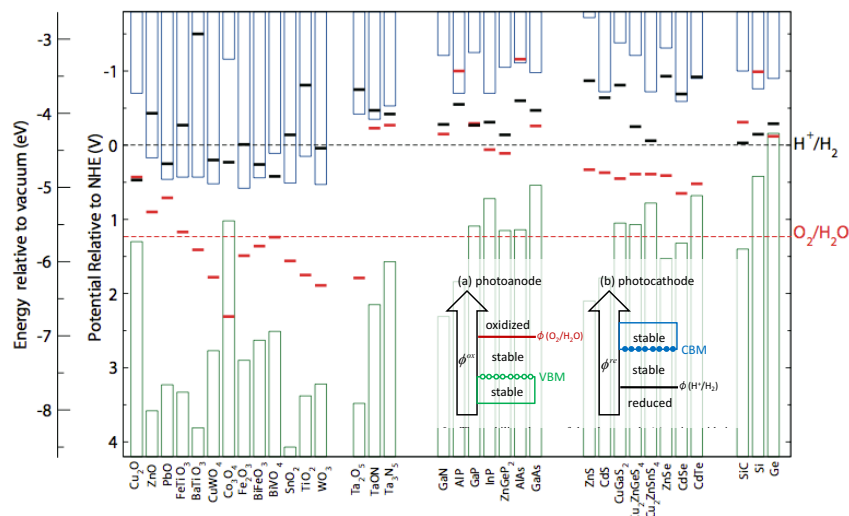


Figure 2.4 Calculated oxidation and reduction potentials for different semiconductors at pH 0. Adapted from Chen & Wang.⁴¹

Efforts to configure side-by-side photoanode + photocathode systems date back to the 1980's, employing traditional photovoltaic materials like p-InP and n-GaAs. Even so early in the history of PEC technology, the protecting ability of metal oxides was known. In a classical paper by Kainthla et al. InP was implemented as a photocathode with Pt and GaAs was protected with MnO_x for the photoanode side. This cell achieved a stable STH efficiency of 8.2% in 6M KOH for 10 hrs.^{37,40}

2.5.2. Wide band gap semiconductors

2.5.2.1. Oxides

Oxides have a huge historical significance largely because TiO_2 was the first material with which Fujishima and Honda demonstrated water splitting on a semiconductor surface in 1972.²³ Despite having conduction and valence band energy levels that provide enough driving force to perform HER and OER, an efficient

implementation of wide band gap semiconductors like TiO_2 , as other 3 eV and wider band gap metal oxide semiconductors such as ZrO_2 , KTaO_3 and SrTiO_3 is problematic because of the very limited absorption in the visible range restricting the maximum theoretical efficiency to less than 2%.²² In fact, the highest PEC STH efficiency with pure monocrystalline rutile TiO_2 was reported in 2011 to be 1.1%.⁴⁷

Even though p- Cu_2O (2.0 eV) is susceptible to reduction by photogenerated electrons, it has been engineered as a photocathode with protective multilayers to prevent photocorrosion for 1hr at 7 mA/cm^2 with 100% faradaic efficiency, which to date is the best performing material among the simple binary oxides. However, the STH efficiency was not stated in the paper, probably due to the observed partial degradation of the sample.⁴⁸⁻⁵⁰ Based on the light intensity and current density at 0V vs. RHE, the efficiency of said Cu_2O cell would be about 9.2%. More recently, Hu & Morales claimed a STH efficiency of 7% with a Cu_2O photocathode coated with amorphous MoS_2 .⁵¹ In general metal oxides (except for Cu_2O , Co_3O_4 , and Ta_2O_5), are thermodynamically stable as photoanodes and are normally n-type, however, their band gaps happen to be too wide, have poor light absorption coefficients and present low hole mobilities.

Among the oxides, BiVO_4 has drawn much attention because its band structure is well suited for use as a photoanode despite that it is widely accepted that it suffers from poor electron-hole separation. Nanoporous films and heterostructures of this vanadate, along with water oxidation co-catalyst layers, have been used to suppress bulk recombination and reduce interfacial recombination. These advances have led to a photocurrent density of 2.7 mA cm^{-2} at a potential of 0.6 V vs RHE with an ABPE of 1.7%^{52 53}

Dual band gap cells with oxide photoabsorbers have generated much interest because their availability and comparably inexpensive deposition methods could advance towards lowering the cost of manufacture to about 100 US\$ m⁻² as this is one of the US DOE goals. A wired Z-scheme cell comprising oxides with a relatively simple structure of FTO/AU/Cu₂O/Al:ZnO/RuO_x photocathode + FTO/W:BiVO₄/Co-Pi photoanode and presents a STH of 0.5%.²⁹ The authors cite the operation instability with current loss of 20% after 2 minutes of testing.

Another efficient device benefiting from the dual band gap approach employs a 3-dimensional photoanode composed of a Si/Hematite core/shell nanowire array decorated with plasmonic gold nanoparticles, with a platinum counter electrode as cathode. The efficiency was 6.0% under AM 1.5G light for at least 40 minutes.

Multi-junction tandem cells have become increasingly complex to get the most out of Earth abundant materials but compromising on performance. Such is the case of the triple junction cell developed by Han et al. consisting of Co-Pi|BiVO₄|a-Si|nanocrystalline-Si|Pt with a device efficiency of 5.2%. In that cell the limiting factor was the BiVO₄ absorber precisely due to its high resistivity, parasitic light absorption by the catalyst and surface resistance.²⁷ It is still noteworthy to observe high-performance with this absorbent layer that was deposited by spray coating, and for that reason it would be less expensive to produce and scale-up compared to processes requiring vacuum. To improve upon the poor-carrier separation efficiency that characterizes BiVO₄, Han et al. implemented a multi-step tungsten concentration gradient in the material.³³

2.5.3. II-IV and III-V with tunable band gaps

Early examples of III-V or II-IV based cells with solid-liquid junctions include dual photoabsorber cells comprising p-GaP, p-CdTe and n-TiO₂ or SrTiO₂. P-n photoelectrolysis cells were developed by Nozik with GaP achieved efficiencies of 0.25%.^{38,54}

In_xGa_{1-x}N has been studied extensively by Yang et al., synthesizing the material with a slightly reduced band gap of 3.1 eV on silicon substrates, in the form of nanowires and as planar electrodes. The theoretical maximum photocurrent of this alloy is 1.3 mA cm⁻². Despite vast efforts, the measured photocurrent was limited to about 1% of the theoretical value. The authors cite fast charge recombination at surface states and a highly resistive charge transfer process to the solution as responsible for the poor performance.⁵⁵

InN nanowires grown by the vapor –liquid-solid technique have been studied for their structural and electronic properties. The as-grown materials show degenerate n-type behavior and XPS studies suggest that electrons accumulate at the surface of the nanowires.⁵⁶ Photoluminescence data of InN and InGaN with high In is consistent with upshift of the band to band emission, and thus suggest that these very highly doped semiconductors suffer from the Moss-Bernstein effect due to electron confinement.⁵⁷

Among all the classes of materials, III-V semiconductors show the most promise and could very well offer a qualitative leap in the state-of-the-art, as opposed to the incremental changes that we have seen in the last two decades with the bulk of the research focused on metal chalcogenides. III-V materials can be alloyed to tune their band gaps, raise or lower their band edges, control the carrier concentration, and grow

good quality crystals with low defectivity. Major drawbacks that need to be addressed in III-V materials are the photocorrosion issue in aqueous solutions, and the fact that precursors are not quite earth-abundant and the substrates are expensive. III-V alloys (in tandem architectures) have shown efficiencies closer to their theoretical potential more than any other class of material, and therefore the extra cost of production could be offset by high efficiency or light concentration.^{46,58-60}

In tandem PEC cells two solid-state junctions in a pn-pn configuration are stacked in a monolithic device as a way to maximize light absorption and increase the driving force for splitting water. Lewis and collaborators have shown that such a configuration, with band gaps of 1.0-1.1 and 1.6-1.9 eV, for the p- and n-type semiconductors, respectively, can yield an STH efficiency of 29.7% with a photocurrent density of 25.3 mA cm⁻².^{61,62} Because of the massive abundance of silicon and the maturity of silicon-related technologies, Z-scheme architectures comprising silicon photocathodes coupled with a 1.8 eV n-type anode, seem to be technically and commercially viable with an estimated STH of 25%.⁶³ The outstanding challenge, however, is identifying a suitable n-type material that has required band gap, good light absorption and low recombination. Poor charge carrier transport properties have hampered the practical implementation of the most heavily studied wide band gap metal oxides, e.g. WO₃, in a tandem cell with silicon.^{31,64} Despite its advantages, silicon presents an indirect band gap, which results in inefficient absorption of the incident photons hence it could be replaced with a direct band gap semiconductor. III-V semiconductor-based photoanodes, especially their ternary alloys, are expected to offer a transformational change in water splitting technology due to their high absorption coefficient and most importantly because their

band gaps are composition dependent. Therefore, the band positions, with respect to the cathode valence band edge, can be engineered in a dual photoabsorber arrangement to separate excitons, control recombination, and force a built-in voltage sufficient to self-catalyze water oxidation.

Previous studies on III-V absorbers have demonstrated that most of them need a high biasing for splitting water and therefore need an additional photovoltaic (PV) device in tandem. Relevant examples of dual-junction tandem devices with HER and/or OER co-catalysts include GaAs/GaInP₂, GaAs/GaInP, and AlGaAs/Si, the first of which holds the record STH efficiency of 12.4% for photoelectrochemical cells with semiconductor/liquid junctions.^{20,62} However, the progress of tandem cell technologies for water splitting has been slowed down by a lack of intrinsically stable photocathode materials with a band gap in the 1.2-1.4 range.⁶³

Recently Verlage & Atwater fabricated a stable integrated prototype having a tandem junction of GaAs/InGaP coated with amorphous titania and Nickel based electrocatalysts. This device exhibited a STH of 10.% at 1 sun illumination for over 40 h of operation.⁶⁵

When the band edge positions of the semiconductor are pH dependent or the stability of material is limited to certain pH range, physical separation of the electrodes in different solutions will certainly be beneficial.⁶³ This is another advantage of III-V's over metal oxides: the III-V band edge positions are pH dependent relative to HER and OER, therefore n-doped III-V absorbers can act as photoanodes in a broader pH range with enough driving force for water oxidation.⁶⁶

Nonetheless, the record-holding tandem structures (for cells with Semiconductor liquid junctions) comprising single crystalline films of and buried InGaAs/InGaP junctions are typically expensive to produce and are hardly scalable. Consequently, it is crucial to envision new electrode architectures with novel materials to solve the remaining challenges. An example of another successful photohydrolysis system, that holds the record STH (among all kinds of fuel forming cells irrespective of the configuration) was reported by Licht in 2002.^{27,67} The device comprised a bipolar semiconductor configuration of $\text{Al}_{0.25}\text{Ga}_{0.85}\text{As}$ ($E_g=1.6$ eV) and Si ($E_g = 1.1$ eV) in tandem, combined with RuO_2 and Pt_{black} electrocatalysts. Such device sustained unassisted water splitting at 18.3% conversion efficiency for 12 hrs. In that cell, no semiconductors were directly in contact with the electrolyte and required two p-n multijunctions stacked together with ohmic contacts directing charge carriers laterally in opposite directions to the electrocatalyst layers. This additional structure complexity makes the device quite expensive to fabricate and thus limits its potential for commercial applications. For new III-V materials, the charge carrier transport, recombination, and choice of the electrocatalyst will play a key role in maximizing the STH, so the processing-structure-property inter-relationship of new water splitting cell devices and materials need to be studied in detail.

$\text{Rh}|\text{GaInP}|\text{GaInAs}|\text{RuO}_2$ cell is among these class of high-performance dual junction photodiodes that are monolithically integrated, use high-performance co-catalysts and operate completely immersed in an electrolyte solution.²⁷ This device by May et al. benefits from surface functionalization allowing 14% STH under zero bias in standard illumination conditions. Like other III-V's, these GaInP and InGaAs have

surface states that trap charge carriers as indicated by overshoots in the transient photovoltage. The surface functionalization provides an additional electronic surface passivation, but the main achievement in this configuration is having an AlInP window that transitions into an oxide/phosphate/phosphite, allowing efficient coupling with the co-catalyst, and reducing interfacial charge-carrier recombination.⁶⁸

In this regard, progress has been made in the recent years for fixing the misalignment of semiconductors like GaInP₂ to achieve a closer overlap with the water splitting redox couples by attaching an appropriate conjugated phosphonic acid to the surface of the semiconductor. Surface modification approaches like this one may allow for unbiased water splitting with a single photoabsorber with band gaps of 2 eV or lower.⁶⁹

Döscher & Lewerentz have reviewed the band gap energies of Silicon and classical III-V compound semiconductors as related with their lattice constants.⁵⁸

Figure 2.5a shows an adaptation of their analysis with additional information for the Sb bearing compounds that are the subject matter of this work. It can be seen that the growth of ternary III-V compounds enables simultaneously engineering the band gap and matching the epilayer to the lattice parameter of silicon in a monolithically integrated photoanode + photocathode architecture.⁹ Such a heterostructure could fall within the high-efficiency contours as shown in Figure 2.5b for photocathode + photoanode PEC.⁶²

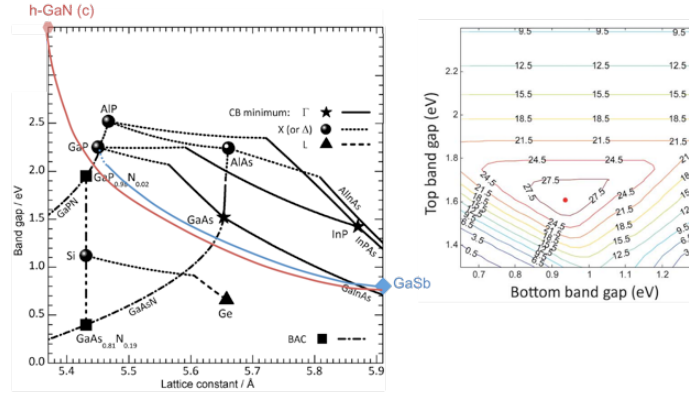


Figure 2.5 a) Band gap energies of elemental and III-V semiconductors versus lattice constants. (Adapted from Ref. ⁵⁸) b) Iso efficiency plot showing the STH efficiency limits of a photocathode + photoanode (Z-scheme) (Adapted from Ref. ²⁷)

2.6. Growth considerations

In heteroepitaxial growth of semiconductors it is quite rare to have perfectly lattice-matched substrate to the semiconductor layer. In most cases the differences between the lattice constants of both materials will cause strained or relaxed growth that can lead to interfacial defects. These deviations typically lead to abnormal mechanical, optoelectronic and thermal properties of the films. For solar energy conversion applications nearly matched lattices are desired in order to reduce defects and improve carrier mobilities. When the mismatch is large, the film may strain to accommodate the lattice structure of the substrate during the first stages of growth with materials of the same crystal structure.

In the cases of heteroepitaxial growth where strain accommodation is not possible then dislocations form at the interface leading to relaxed epitaxy, and the deposited layer returns to its original lattice structure beyond the first few nanometers of above the

interface.⁷⁰ These phenomena for strain relaxation are graphically represented below in Figure 2.6.

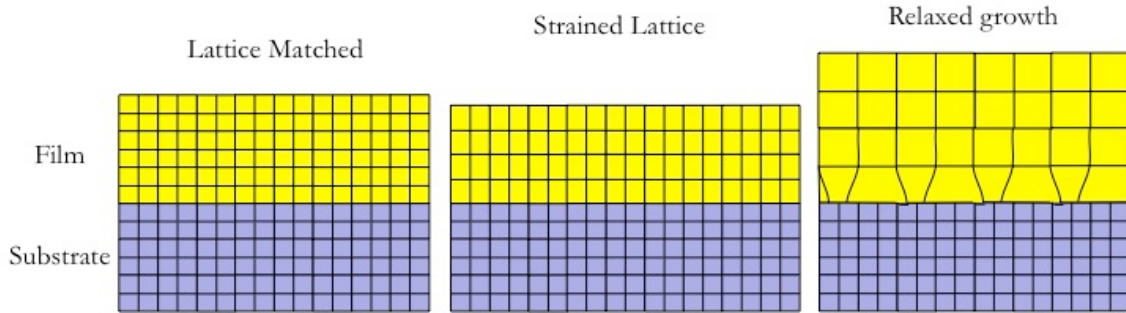


Figure 2.6. Strain relaxation in lattice mis-matched growth.

The lattice mismatch strain is defined by the following expression:

$$f = \frac{a_s - a_e}{a_e}$$

Where a_s and a_e are the lattice constants of the substrate and the epi-layer, respectively. The value of f can exceed 10% but it is typically much smaller for heteroepitaxial junctions of practical interest.

When the miss-match is low, i.e. less than 1%, the deposited layer grows in a coherent pseudomorphic fashion. Therefore, in thin films with low mismatch the pseudomorphic layer presents in-plane strain equivalent to the lattice mismatch. In other words, the lattice constant expands or contracts by the same percent as the mismatch strain, f . However when the epi-layer thickness reaches a critical threshold the compressive or expansive energy stored in the film is greater, and the creation of misfit dislocations at the interface begins to relax some of the strain. Thus in thick films the total relaxation is a combination of elastic and plastic strain.⁷¹

The Zinc Blende structure of GaP with lattice parameter 5.4505 Å is nearly a perfect match for the silicon lattice formed by two interpenetrating face centered (fcc) cubic lattices with parameter $a=5.44\text{Å}$ for heteroepitaxial growth as shown in Figure 2.7.

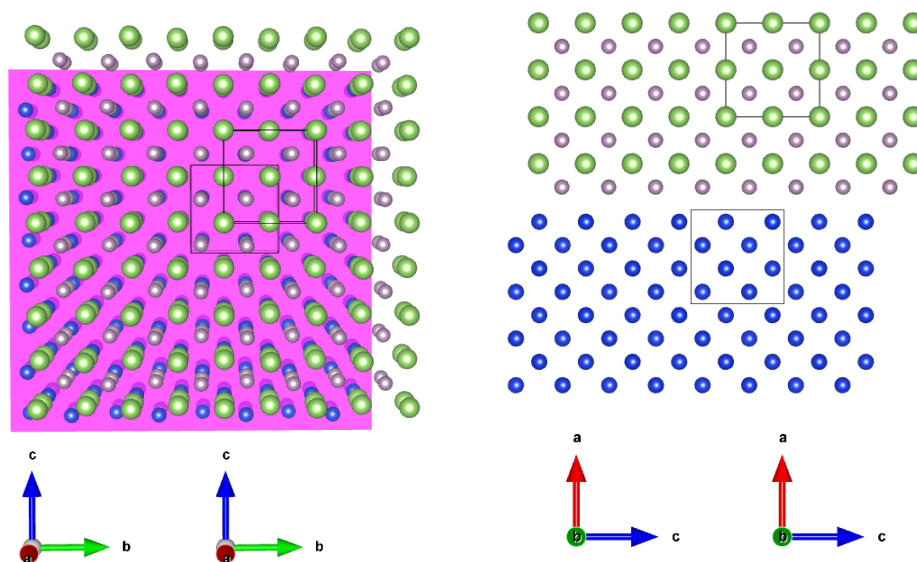


Figure 2.7 Epitaxial relationship between $\text{GaSb}_x\text{P}_{1-x}$ and (100) Si.

2.7. Antecedents of Metal Organic Chemical Vapor Deposition of GaSbN

III-nitrides can be grown using multiple different techniques, including molecular beam epitaxy (MBE), metal organic vapor phase epitaxy (MOVPE or MOCVD), halide vapor phase epitaxy (HVPE), high-pressure solution growth, and sputtering. The choice of one deposition technique over others depends on the specific application.⁷²

Previous studies on metal organic vapor deposition of GaSbN have been directed towards developing a new material based on alloys of GaSb and GaN. The bulk of the work by S. Sunkara was mainly focused on growth of ternary alloys on planar substrates like Si and Sapphire at low temperatures between 400 to 600°C. That temperature range

led to deposition of polycrystalline films. The scope of the work was expanded to growth of core/shell structures of GaSbN/GaN using a-plane GaN nanowire templates as a strategy to relax strain and obtain heteroepitaxial nanowire mats for water splitting photoanodes. Additionally, our preliminary work achieved growth of GaSbN textured films with incorporation of antimony at processing temperatures up to 800°C.

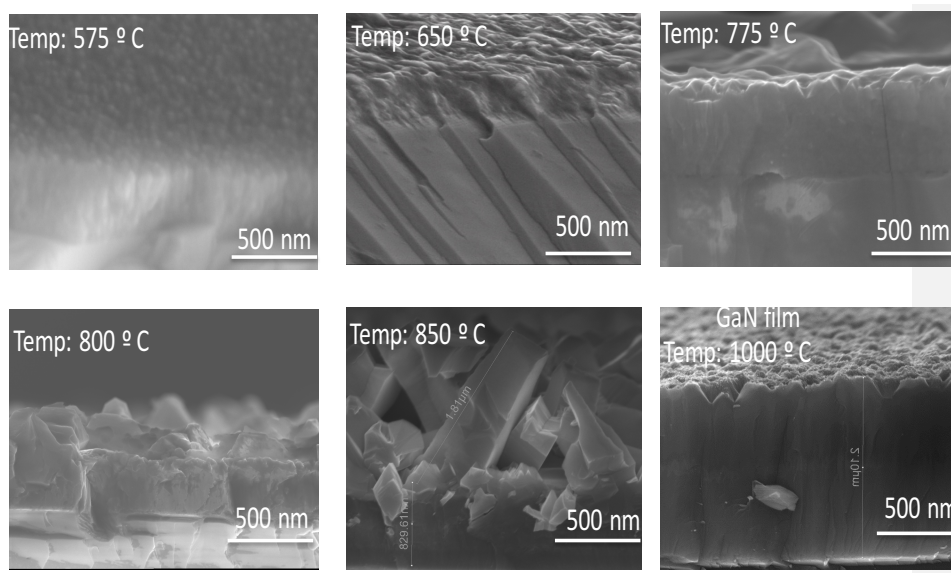


Figure 2.8 $\text{GaSb}_x\text{N}_{1-x}$ (575-800°C) and GaN (850-1000°C) films deposited by MOCVD. Adapted from Sunkara et. al., 2016.

However, the quality of the textured films (Figure 2.8) obtained in that temperature range was deficient, compared with similar III-V alloys reported in the literature such as $\text{InGaN}^{73,74}$, GaAsN , AlGaIn^{75-77} , $\text{GaPN}^{58,59,78,79}$ that have an epitaxial morphology with low defectivity.

Among these set of prior experiments, the best performing samples were thick polycrystalline samples, with flat band potential of about -0.0 V vs. RHE and moderate donor concentrations of about 10^{17} cm^{-3} . The maximum photocurrent density in these

polycrystalline samples was about 0.25 mA cm^{-2} at a bias of 1.23 V vs. RHE. (Figure 2.9) The theoretical maximum photocurrent density of a semiconductor of 1.8 eV band gap based on the Shockley-Queisser limit is over 20 mA cm^{-2} . This incongruence between the actual current outputs of the photoelectrodes vs. their theoretical capacity required an explanation.

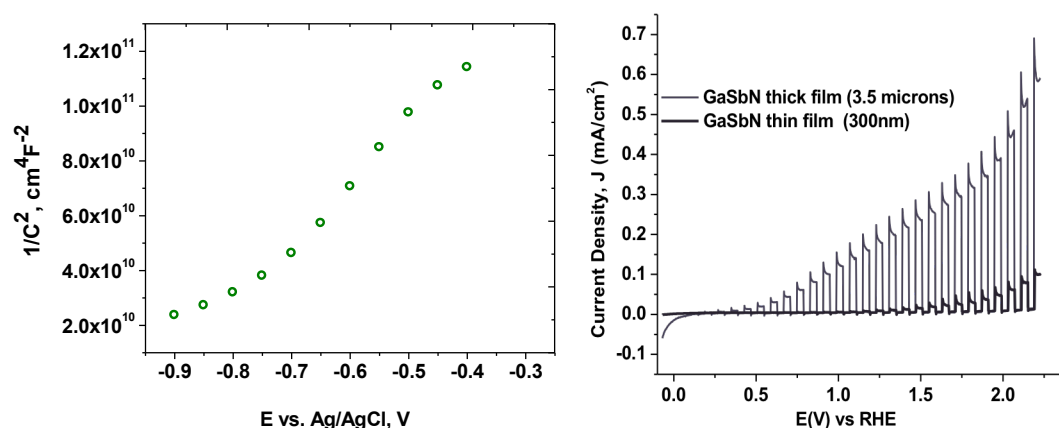


Figure 2.9 Photoelectrochemical characterization of polycrystalline $\text{GaSb}_x\text{N}_{1-x}$ films. Adapted from Sunkara.⁸⁰

It was speculated, based on the morphology and crystalline quality of these preliminary films that recombination at grain boundaries and defects in the films with a proper band gap were limiting the amount of current and voltage output of the GaSbN photoanodes. Improving the quality and composition of this material to test the aforementioned hypothesis was a motivation for the present work.

CHAPTER 3

EXPERIMENTAL METHODS

The experimental methods and materials used for the completion of this work are presented in this chapter.

3.1. Computation techniques

Previous work by Russell, Sunkara and Menon reported computational predictions using First-principles density functional theory (DFT) for the theoretical study of $\text{GaSb}_x\text{N}_{1-x}$ and $\text{GaSb}_x\text{P}_{1-x}$ systems.^{16,81-84} In the case of the nitride system such studies revealed that small amounts of Sb incorporation could cause band bowing from 3.4 to 1.8 eV, while the band edges, even with the narrowed band gap, would straddle the redox potential for the water splitting reactions. The predicted band structure of the phosphide suggested that at incorporation levels of 1% Sb the band gap would transition from indirect to direct.

3.2. Metalorganic Chemical Vapor Deposition of III-Nitrides

Metal organic chemical vapor deposition has been the method of choice for growth of III-V materials because it facilitates deposition of epitaxial layers and heterostructures with low defectivity using a wide palette of metalorganic precursors even on non-matching lattices. MOCVD provides multiple fabrication advantages like

enabling the deposition of single crystalline ternary alloys with very accurate control of the composition, doping, electronic properties, thickness, and uniformity of the films by carefully manipulating the process parameters and deposition steps. The main weakness of MOCVD, however, is the typically low growth rate that results from reaction rate limitations and/or mass transfer across the boundary layer.

Lately, photovoltaic and photoelectrochemical materials based on III-V chemistries for solar energy conversion have shown enormous promise and have led to record-breaking efficiencies. Yet, in order to bring the cost down of epitaxial III-V films it is necessary to significantly increase MOCVD throughput while preserving film composition and quality.

GaN and GaSbN samples were grown in a MOCVD reactor having a vertical configuration with cold walls and a total volume of 5.5 L. A resistive 2-inch boron nitride susceptor was used as the heater to set the deposition temperature of the substrates. All precursors were fed to the growth chamber through a showerhead located at the top of the chamber, as shown in Figure 3.1. The reactants and carrier gases flow downward perpendicular to the substrate surface. All growth experiments were carried out at a chamber pressure of 70 torr and a gas velocity such that the flow is laminar in the chamber.

$$Re = \frac{\rho V d}{\mu}$$

The distance from the shower to the susceptor was varied between 4.5 and 2.5 cm, to minimize radial non-uniformity in the growth caused by asymmetry in the design and

characteristics of flow over the stagnation point. The optimal showerhead-to-substrate gap was determined by simulating the growth conditions in Ansys Fluent (Figure 3.1).

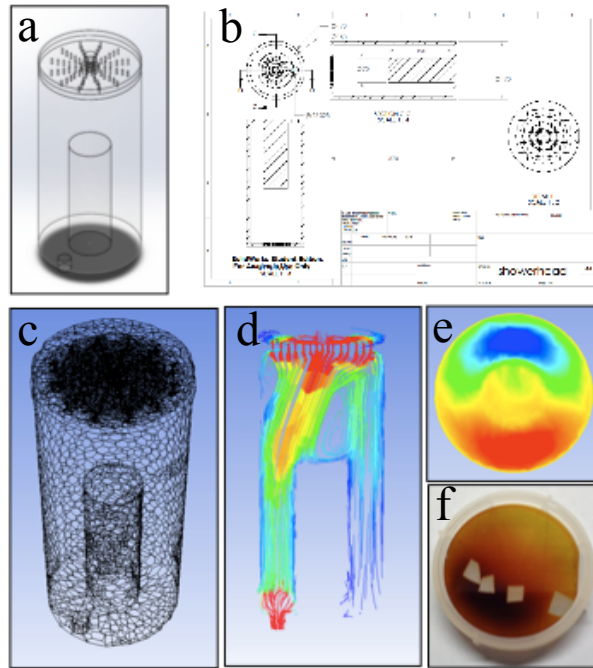


Figure 3.1. a) 3-D rendering of MOCVD chamber used for CFD analysis at the stagnation point
 b) drawing of the chamber with dimensions c) meshing d) streamlines e) radial velocity contours
 f) top view of GaSbN wafer

A simplified P&ID of the MOCVD tool is presented below in Figure 3.2.

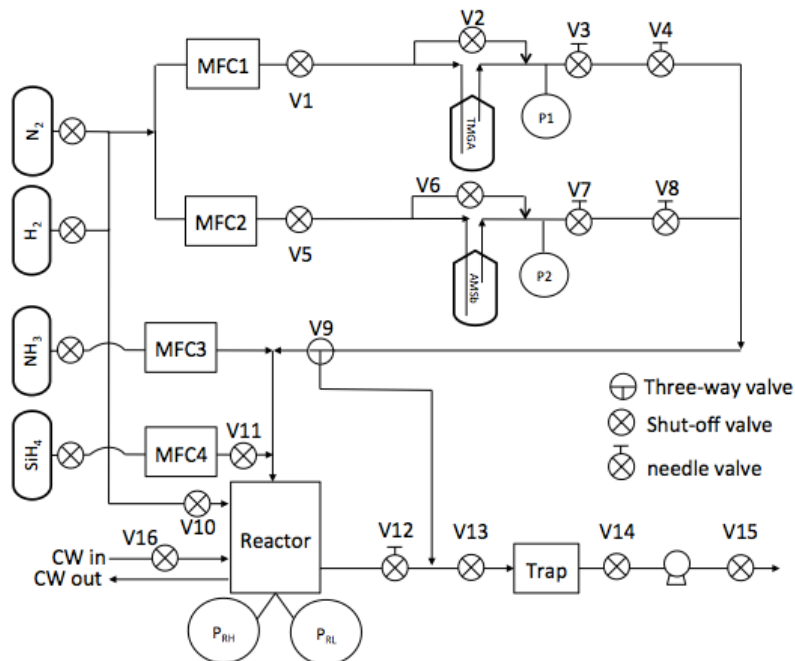


Figure 3.2 MOCVD reactor P&ID with gas-handling network.

Trimethyl gallium with formula $(\text{CH}_3)_3\text{Ga}$ is used as the metalorganic source of gallium for growth of the III-V films. For delivering antimony, TMSb was initially used until the precursor exhausted and was replaced for AMSb (Tris dimethyl amino antimony) due to lack of availability of the initial precursor. According to the reactant datasheet, vendor information, and information in the literature the only difference with TMSb is the temperature dependence of the vapor pressure. The molar flux was controlled by setting a temperature at the TMGA bubbler, the carrier gas flow rate, and the total pressure in the line. The total flux is estimated according to the following expression:

$$n_{TMGa \text{ or } AMSb} = \frac{P_{vap} [\text{torr}]}{P_T [\text{torr}]} \cdot \frac{Q_c [\text{cm}^3 \text{ min}^{-1}]}{22400 [\text{cm}^3 \text{ mol}^{-1}]}$$

Where Q_c is the carrier gas flow rate in SCCM, P_{vap} is the vapor pressure in Torr, and P_T the total pressure in each of the precursor bubblers. This vapor pressure was adjusted between 70-700 torr using a manual needle valve throughout the course of the experiments to regulate the partial pressure of the precursors.

The vapor pressures of each of the reactants follow the Antoine equation⁸⁵,

$$P_{vap [TMGa]} = 10^{8.07-1703/T[K]}$$

$$P_{vap [AMSb]} = 10^{6.23-1734/T[K]}$$

The flow rate of N₂, the carrier gas in the Sb line was constant for all experiments at 50 sccm, while the flowrate for the Ga precursor line was varied between 2 – 10 sccm. The bubbler temperatures for TMGa ranged between -7 to -15°C and for AMSb between 0 and 45°C. The Ga bubbler pressure was constant for all experiments at 700 torr in order to maintain a low TMGa partial pressure in the line, thus ensuring small molar fluxes compared to the Sb line, which was constant 100 Torr.

The leakage rate of air into the MOCVD chamber was calculated by measuring the pressure increase as a function of time as shown in Figure 3.3b. The rate of pressure increase in the chamber at operating pressure was estimated to be about 4.5 mTorr sec⁻¹ from the slope of graph (Figure 3.3b), which is equivalent to 0.6 Pa s⁻¹.

The leakage rate is calculated with the following expression:

$$Q_L = \frac{\Delta P}{\Delta t} \cdot V = 0.6 \text{ Pa s}^{-1} \cdot 5.5 \times 10^{-3} \text{ m}^3 = 3.3 \times 10^{-3} \text{ Pa m}^3 \text{ s}^{-1}$$

From the ideal gas law, we can estimate the moles of oxygen leaking into the chamber per min.

$$\dot{n} = \frac{Q_L}{RT} \cdot \frac{0.22 \text{ mol } O_2}{\text{mol air}} \cdot 60 \frac{\text{sec}}{\text{min}} = 17 \frac{\mu\text{mol } O_2}{\text{min}}$$

This leak rate is equivalent to about 1×10^{19} molecules of air leaking into the system every minute.

For preliminary experiments a one-step growth method was implemented but the core of the experiments leading to epitaxy were done with a two-step growth method, with an annealing step before growth as shown in Figure 3.3a.

Due to the vast differences in volumetric flow rates in the Ga and Sb line, the total line volumes were estimated using the dimensions of each line, and the residence times were calculated accordingly for each experimental condition. This consideration is essential to determine at what point during the experiments the bypass valve can be switched to run, instead of vent, thus guaranteeing that the composition in the line feeding the reactor is steady at a desired value.

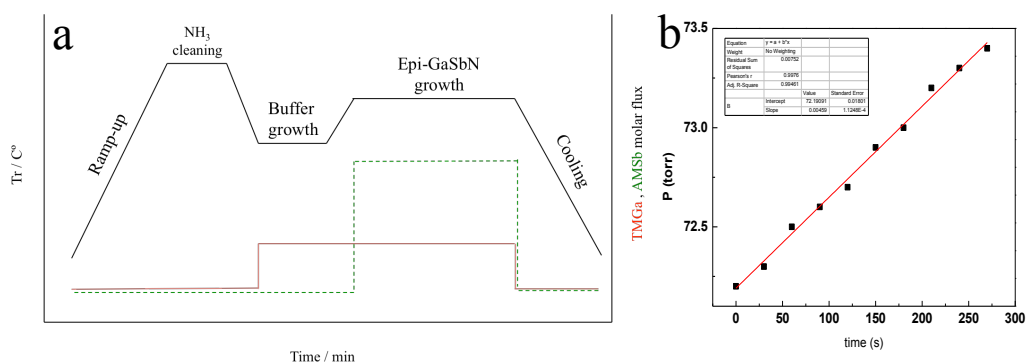


Figure 3.3 a) Two step growth process with Temperature and molar flux profiles, b) Air leak rate into MOCVD chamber at operating pressure.

In chapter 5 a vapor-liquid-solid (VLS) MOCVD method is presented for growth of highly oriented films of ternary alloys of GaSbN, that yields high growth rates and permits controlling the Sb incorporation in the alloy.

Copper nanoparticle suspensions in isopropyl alcohol were prepared by sonication, and subsequently drop cast on GaN/sapphire substrates and sonicated at room temperature until the liquid phase had fully vaporized leaving behind a thin film of copper nanoparticles. Then, the copper particles were reduced in a hydrogen plasma atmosphere for 1 hr., resulting in a uniform copper film on GaN/Sapphire substrates. These copper thin films were used as substrates for MOCVD growth of GaSbP. Details of the plasma-assisted reduction method and the experimental setup are presented elsewhere.⁸⁶

3.3. Halide Vapor Phase Epitaxy of III-Phosphides

3.3.1. Growth of $\text{GaSb}_x\text{P}_{(1-x)}$ films

$\text{GaSb}_x\text{P}_{(1-x)}$ samples were grown using halide vapor phase epitaxy (HVPE) technique in a quartz tube reactor with two heating zones where metal precursors are placed at different axial positions along the length of the furnace heater. Gallium (Ga), Antimony (Sb) metal powders and liquid PCl_3 were used as precursor materials. 10 g of each metal were measured and contained in separate boron nitride crucibles. Silicon substrates were cleaned by sonication for 15 minutes in methanol:water:HF:methanol (1:1:1:1) solution to remove dust particles, organics, etch the native SiO_2 . The clean

silicon substrates were dried in nitrogen and loaded onto a graphite susceptor by means of a molybdenum nut-bolt assembly to ensure proper thermal contact.

Before starting growth, the air in the tube reactor was pumped down to a base pressure of 200mTorr. Three purging cycles were carried out with UHP nitrogen between 700 and 0.2 torr. For growth, the reactor pressure was maintained at 500 torr by means of an automatic throttle valve, and the PCl_3 bubbler pressure was held at 650 torr. The bubbler was kept at room temperature at an average temperature of $35^\circ\text{C} \pm 5^\circ\text{C}$. Sb and Ga zone temperatures $T_{\text{Sb}}=650^\circ\text{C}$ - 750°C , $T_{\text{Ga}}=970^\circ\text{C}$ were explored in these experiments. 300 and 30 sccm of hydrogen (H_2) gas were used to pressurize the reactor and as a carrier gas for PCl_3 precursor. All the samples were deposited on Si substrate $\langle 100 \rangle$ with 3° miscut which is mounted on a graphite susceptor and deposition temperatures were varied between 700°C to 900°C . The growth process was allowed to take place for an hour. A detailed description and schematics of reactor can be found in Figure 3.4

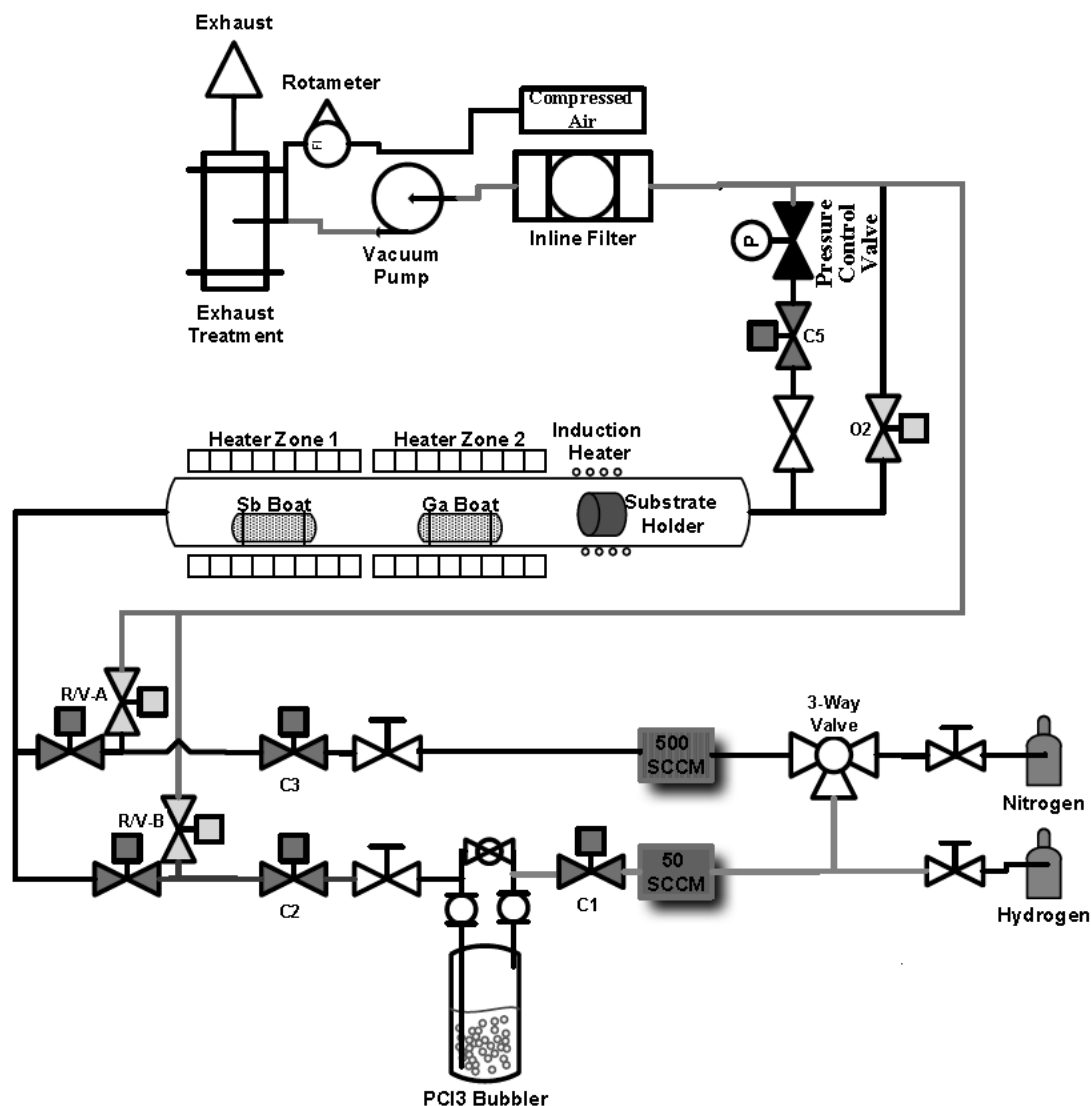


Figure 3.4 Simplified P&ID Diagram of HVPE System

3.4. Materials Characterization

All samples were characterized using X-Ray diffraction (a Bruker Discovery D8 system) utilizing Cu K α radiation (0.154 nm), between 10-80°, at a scan speed of 0.2 seconds per step, with angle steps of 0.01°. Reference GaP and GaN wafers were used as standards to validate the diffraction peak positions of the compounds. The reflections for

ternary alloys were assessed for the angle shift with respect to pure gallium phosphide and gallium nitride.

The average size of crystalline domains was determined using Scherrer's equation:

$$\tau = \frac{K \lambda}{\beta \cos \theta_b}$$

Where τ is the average size of the crystalline domains in nm, K is a dimensionless shape factor commonly assigned the value of 1. λ is the wavelength of the Cu α radiation. β is the Full Width Half Maximum (FWHM) of the 002 reflection (for GaSb_{1-x}N_x) in radians, and θ_b is the Bragg Angle of that reflection.

The sample morphologies at the top surface and cross-sections of the samples were studied by Scanning Electron Microscopy (SEM) using a (TESCAN VEGA3 SB-EASYPROBE) SEM in secondary electron mode.

Diffuse reflectance UV-Vis measurements were performed on each of these samples with a Perkin Elmer Lambda 950 UV-Vis spectrometer with a 60 mm integrating sphere and Tauc plot analysis was used to determine band gap. The spectral absorption coefficients and absorption depths were estimated using the Kubelka-Munk function and the scattering coefficient of the material, with the following expressions:

$$F(R_\infty) = \frac{(1 - R_\infty)^2}{2R_\infty} = \frac{K}{S}$$

$$L = K^{-1}$$

Photoluminescence and Raman measurements were taken from a single sample using a Renshaw Invia Micro Raman spectrometer with 442 nm laser. For cold PL, a liquid nitrogen cooling stage was used to cool the samples to ~77 K.

3.5. Electrochemical Methods

The 2- and 3- electrode potentiometric, amperometric, and EIS measurements were performed using a BioLogic SP200/Z-01 potentiostat, Pt mesh counter-electrode and Ag/AgCl reference electrode. All PEC tests were done in 1M H₂SO₄ aqueous solution (unless otherwise noted in a specific figure) using DI water of 18 mOhm/cm resistivity. The photoanodes were illuminated using a Xenon lamp equipped with a AM 1.5 filter and the light power was adjusted by changing the distance from the source to the photoelectrode.

3.5.1 Electrode fabrication

Electrodes were prepared by making top or bottom electrical contacts from nickel-plated copper wire to the semiconductor surface with In/Ga eutectic and silver epoxy. To create an ohmic contact between the metal and an n-type semiconductor, the work functions must be such that:

$$\phi_m < \phi_{sc}$$

The issue however, is that for the new material under study, the work function is not known so selecting a metal to avoid the formation of rectifying junction is in itself a problem. For this reason the In-Ga eutectic was selected as the contact material of choice

because it has the lowest work function among the common metals, i.e. 4.1 eV vs. Vacuum.

This consideration is important to prevent the formation of a potential barrier, with height ϕ_b , at the junction between the semiconductor and the wire that is connected to the potentiostat for measurements, or the counterelectrode in a working device. If the ohmic contact is not formed, the band diagram of the working electrode will prevent majority carriers from going to the back contact and the counter electrode. Such a phenomenon (in equilibrium conditions) is shown in Figure 3.5.

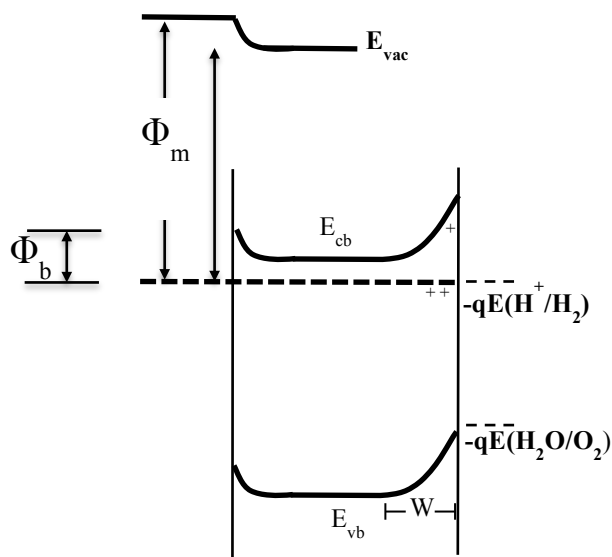


Figure 3.5 Band diagram of an n-type semiconductor in contact with metal forming a rectifying junction.

The depth of this potential well becomes even higher when the electrode is reverse biased, which is the normal operating condition of a PEC under illumination. The accumulation of majority carriers at the surface can limit the efficiency of the cell by a

phenomenon referred to as back-electron recombination, where majority carriers in the bulk of the material annihilate holes that could otherwise participate in oxidation of water.⁸⁷

3.5.2 Open Circuit Potential Measurements

Measurement of the open circuit potential in the dark under illumination and in the dark is an easy way to determine the energy level of the conduction and valence bands of an ideal semiconductor. The knowledge of the band positions with respect to redox potentials of water splitting is important because it will determine to what extent there is enough thermodynamic driving potential to oxidize and reduce water.

In this experiment, photoanodes were immersed in an electrolyte solution (1M H₂SO₄) and connected in 3-electrode setup to platinum working electrode and Ag/AgCl reference electrode. The intensity of the light shining on the photoanode (between 1 and 4 suns) was adjusted with a calibrated photodiode by defining the distance from the light source to the electrode.

Typically, one sun illumination (100 mW cm⁻²) is not enough to completely flatten the bands so more illumination is necessary even when the spectral characteristics of the lamp provide radiation that is more energetic than the band gap. The inability to remove any pre-existing band bending at the surface is caused by defects in the material causing slow recombination rates.⁸⁸

Intense illumination cancels out the band bending because excess majority carriers generate an electric field opposing that of the space charge layer. Thus, in an n-type material, excess electrons created by illumination make the conduction band level more

negative as the depletion region progressively disappears. The potential difference between the dark and illuminated conditions defines the photovoltage, V_{ph} , of the cell.

The electrode potential is measured against a reference electrode, like Ag/AgCl.

To compare the measured flat band potential of the photoanode against the electrochemical potential for hydrogen evolution, which is 0 V vs RHE, it is necessary to convert the measured potential to the RHE scale using a simplified form of the Nernst equation:

$$E_{RHE} = E_{Ag/AgCl} + 0.2 + 0.059 pH$$

In certain circumstances, it is not possible to measure the open circuit potential, and therefore the flat band potential, because the measured value is drifting in time. This problem is caused by photocorrosion of the sample, adsorption of ions on the surface of the electrode, or temperature increase of the electrolyte solution.¹⁷

3.5.3 Mott-Schottky

Potentiostatic electrochemical impedance spectroscopy (EIS) can also help map the semiconductor band-edge positions relative to the solution redox levels.

In this experiment the working electrode potential is swept in a range that spans around 1 V around the expected flat band potential. The expected E_{fb} is obtained either from illuminated OCP, as mentioned previously, or from the onset potential in the current-voltage characteristics of the photoanode as obtained by chopped linear sweep voltammetry.

This technique stems from the fact that the depletion region (at the SLJ) contains electrostatic charges, and thus it can be modeled as a double plate capacitor, with capacitance C_{sc} . A second capacitance in series, arising due to the Helmholtz layer in the solution, can also be modeled with a capacitance C_H .

In a very simplified case, the semiconductor depletion layer capacitance is modeled after Poisson's equation⁸⁹:

$$\frac{1}{C_{sc}^2} = \frac{2}{N_D e_o \epsilon_s} \left[(V - V_{fb}) - \frac{KT}{e_o} \right]$$

Where V_{fb} is the applied potential at which the conduction and valence bands are no longer bent. Thus when plotting $1/C_{sc}^2$ versus the applied potential, the intercept with the x-axis gives an estimate of the flat band potential, and the slope of the graph can be related to the donor concentration, N_D , and the conductivity type of semiconductor.

3.5.4 Linear Sweep Voltammetry

Chopped LSV plots are used in the context of photoelectrochemistry to assess the performance of the photoanodes for solar energy conversion. In this experiment the working electrode is wired to the 3-electrode cell, while simulated 1.5AM light is shone on and off, on the surface of the semiconductor, as the working potential is swept from cathodic potentials (negative of the E_{fb}) towards anodic potentials. In this way the turn on voltage of the diode (onset potential) can be determined under illumination. In the case of the photoanode, more negative onset potentials are desirable and give light into how catalytic the surface of the semiconductor is for lowering the overpotential for oxygen evolution. When the overpotential of the counter electrode reaction is handled by the

potentiostat and the efficiency of un-assisted water splitting can be evaluated under zero external bias. The solar-to-hydrogen efficiency, η_{STH} is determined according to the following expression:

$$\eta_{STH} = \left[\frac{|j_{sc}(mA\ cm^{-2})| \times (1.23\ V) \times \eta_f}{P_{total}\ (mW\ cm^{-2})} \right]_{AM1.5G}$$

Where P_{total} is the power density of the simulated light and η_f is the faradaic efficiency of the reaction. The faradaic efficiency is the ratio of minority carriers that participate in faradaic reactions (oxidation of water in the case of the photoanode) to the total number of carriers that are photogenerated.

Additionally, the general shape of the LSV curve, particularly its “squareness”, is also another important conversion efficiency property. The fill factor in PEC hydrogen production is important because it is desirable to maintain a high photocurrent to maximize production rate with a minimum voltage drop below the device’s maximum useable potential.¹⁴

3.5.5 Chronoamperometry

This electroanalytical technique can be used in both 2-electrode or 3-electrode cell setups. In the former, the reference is shorted to the counter electrode. In the later, a reference such as Ag/AgCl electrode is inserted in the cell along with the working and counter electrodes. In both cases, current is measured throughout the experiment as a function of time. In 3-electrode chronoamperometry bias can be applied to the working electrode with respect to the reference.

This technique is useful to assess the stability of photoelectrodes, by studying the current decay over time if the electrode is photocorroding or dissolving into the solution. It can be also used along with another analytical techniques, for example with an oxygen fluorescence probe to measure the amount of evolved oxygen simultaneously while performing the current measurements at any given potential. The results of chronoamperometry are normalized to the active area of the electrode to report current densities instead of currents, so as to have comparable data in terms of mA cm⁻².

3.5.6 Incident Photon-to-Current Efficiency and Photocurrent Spectroscopy

Incident Photon-to-Current Efficiency also known as the External Quantum Efficiency is an important metric to establish what is the spectral response of a photoabsorber. According to its definition, IPCE measures the ratio of electron flux that is extracted from the electrode to the photon flux that shine on the semiconductor, in a range of wavelengths. The IPCE measurements were done at zero bias in a potentiostatic measurement versus a shorted counter electrode. This measurement gives an idea of how many carriers are generated per incident photon, how efficiently they are transported to the SLJ and transferred through the interface.¹⁷

$$\text{IPCE}(\lambda) = \text{EQE}(\lambda) = \frac{\text{electrons/cm}^2/\text{s}}{\text{photons/cm}^2/\text{s}} = \frac{|j_{\text{ph}}(\text{mA/cm}^2)| \times 1239.8(\text{V} \times \text{nm})}{P_{\text{mono}}(\text{mW/cm}^2) \times \lambda(\text{nm})}$$

Photocurrent spectroscopy (PCS) uses the same experimental setup and procedure as IPCE, but it examines the photocurrent going through the external circuit of the PEC cell as a function of wavelength. This technique is complementary to UV-Vis spectroscopy to gain insight into the electronic band gap of the semiconductor and it

includes information about charge transport and interfacial transfer efficiencies. A Tauc plot of the PCS data also shows the type of electronic transitions caused by photoexcitation.^{5,17}

CHAPTER 4

P-TYPE Cu_2O NANOWIRE ARRAY PHOTOCATHODES

The photoactivity performance of Cu_2O has been a major concern, in addition to its rapid dissolution in aqueous solution. Recently, Grätzel and co-workers prepared a Cu_2O film (2-5 micron thick) electrode comprising electrodeposited polycrystalline films (2-5 microns thick) coated with several protective layers and a catalyst that yielded an impressive photoactivity but only half of the theoretical maximum current density⁴⁸. Even at this level, the observed photoactivity represents an order of magnitude enhancement over the past research till date. The reasons for such enhancement are not clear.

One-dimensional nanostructures such as nanowires have the potential to produce high photoactivity due to fast charge transport properties and reduced length scales for minority carrier diffusion expected in single crystalline nanowires. In our previous work, we developed a rapid two-step process for the scalable synthesis of copper oxide nanowire arrays on copper foils.⁹⁰ This involves a wet chemical oxidation of copper foils followed by oxidation in atmospheric microwave plasma. The nanowire arrays were subsequently coated with titania using atomic layer deposition to improve the aqueous stability. The photocurrents obtained with this method are much lower ($<0.4 \text{ mA cm}^{-2}$) but better than the data obtained with polycrystalline thin films to that date. The presence of a mixed phase of Cu_2O and CuO has been identified as a possible cause for the low

photoactivity. CuO has an indirect band gap of 1.4 eV leading to inefficient photon absorption and also cannot generate sufficient energy required to split water. Further, some of the recent reports have indicated that the conduction band edge for p-type CuO lies below reduction potential, making it an inefficient photocathode for water splitting^{35,64}. Hence, phase purity of Cu₂O is an important factor that needs to be addressed to improve the photoactivity of the Cu₂O NW arrays made through atmospheric plasma oxidation.

Prior approaches to improve both the stability and performance of Cu₂O use ultra-thin coatings of n-type wide band gap semiconductors to create a pn junction at the semiconductor-water interface.⁹¹ The low temperatures used in atomic layer deposition (ALD) typically result in amorphous layers with poor charge transport properties. Paracchino and co-workers⁹¹ discussed that presence of Ti³⁺ trap states in an amorphous TiO₂ film deposited by ALD as one of the major factors leading to loss of photoactivity. Furthermore, a subsequent annealing step is usually required to improve the crystallinity for getting good photoactivity.

Several recent efforts to improve the stability of Cu₂O have included using protective layers of NiOx, carbon, CuO, and TiO₂.^{64, 35, 92, 93} In general, these strategies are directed to benefit from electrocatalysis or band edge energetics that enhances the rate of electron transfer to water and diminishes the accumulation of charge carriers and their recombination. However, it is interesting to note that not much attention has been paid to synthesizing conformal coatings of high crystallinity which is essential for fast electron transfer at the semiconductor-water interface.

In this work, we investigated the use of n-type crystalline WO_3 and CuWO_4 conformal layers on Cu_2O nanowire arrays using hot wire chemical vapor deposition and studied their impact on photoactivity and durability. The use of Hot Wire Chemical Vapor Deposition (HWCVD) for obtaining conformal coatings of either WO_3 or CuWO_4 on nanowire arrays and for the deposition of CuWO_4 itself have not been achieved before.

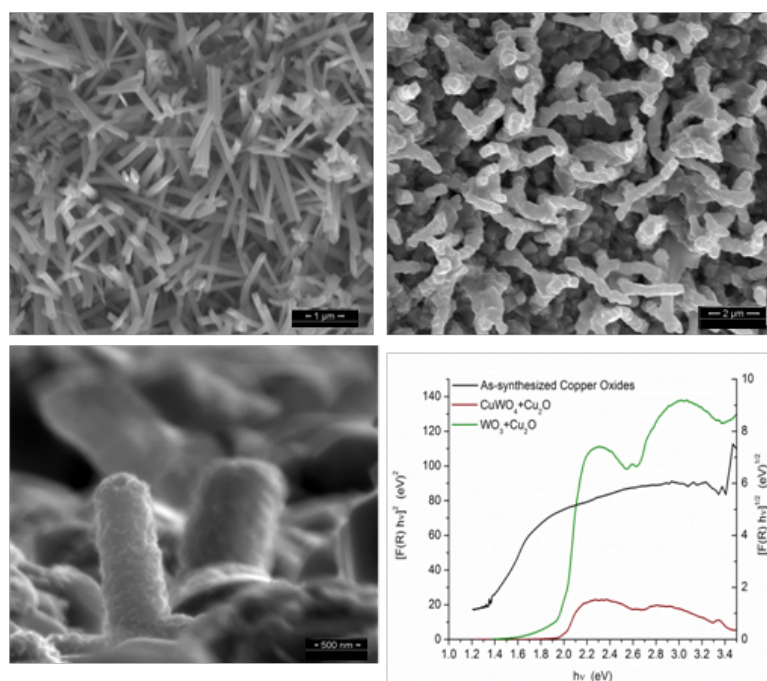


Figure 4.1 a) SEM of Cu_2O NW array (top view), b) SEM of Cu_2O nanowire array coated with CuWO_4 (top view); c) SEM of Cu_2O nanowire coated with WO_3 (tilted cross-section). d) Tauc plots for the as-synthesized Cu_2O , CuWO_4 coated Cu_2O NW arrays, WO_3 coated Cu_2O NWs and vacuum annealed Cu_2O NWs.

Copper oxide nanowire arrays were synthesized by wet chemical oxidation followed by short exposure to atmospheric plasma. The copper foil was cleaned in dilute HCl (0.1M) and rinsed in deionized water. The foils were immersed for 8 minutes in an

aqueous solution of sodium hydroxide and ammonium persulfate. A typical solution for the wet chemical synthesis was prepared by mixing 4 mL of 10 M NaOH, 2 mL of 1 M ammonium persulfate and 9 mL of deionized water.

The copper hydroxide nanowires produced were converted into copper oxide nanowires by means of exposure to an atmospheric plasma discharge (750 W) for 2 minutes. The details of the process are described elsewhere⁹⁰.

The deposition of WO_3 was performed in a HWCVD reactor using oxygen flow over a hot tungsten filament used as the source for tungsten oxide vapors. The filaments were resistively heated to a temperature of 800°C as measured by dual wavelength optical pyrometry, and the substrates were heated to a temperature of around 600°C. A detailed description of the reactor is described in an earlier publication⁹⁴. The deposition of CuWO_4 is attempted for the first time here. The procedure used is as follows: a 6 foot-long tungsten wire (0.5 mm in diameter) was coiled in the shape of a spring (10 cm in length and step size of 5 mm); then each loop of this main tungsten helical spring was used as the rotation axis of a secondary copper filament (0.25 mm in diameter, 18 ft long) that was wrapped around the tungsten wire loops. Thus forming a double spring assembly, where the core is tungsten and the wrapping is copper wire. It is worthwhile to point out that these dimensions are critical to controlling the relative resistance of the wires, to achieve a uniform filament temperature and prevent failure of the Cu wire by melting.

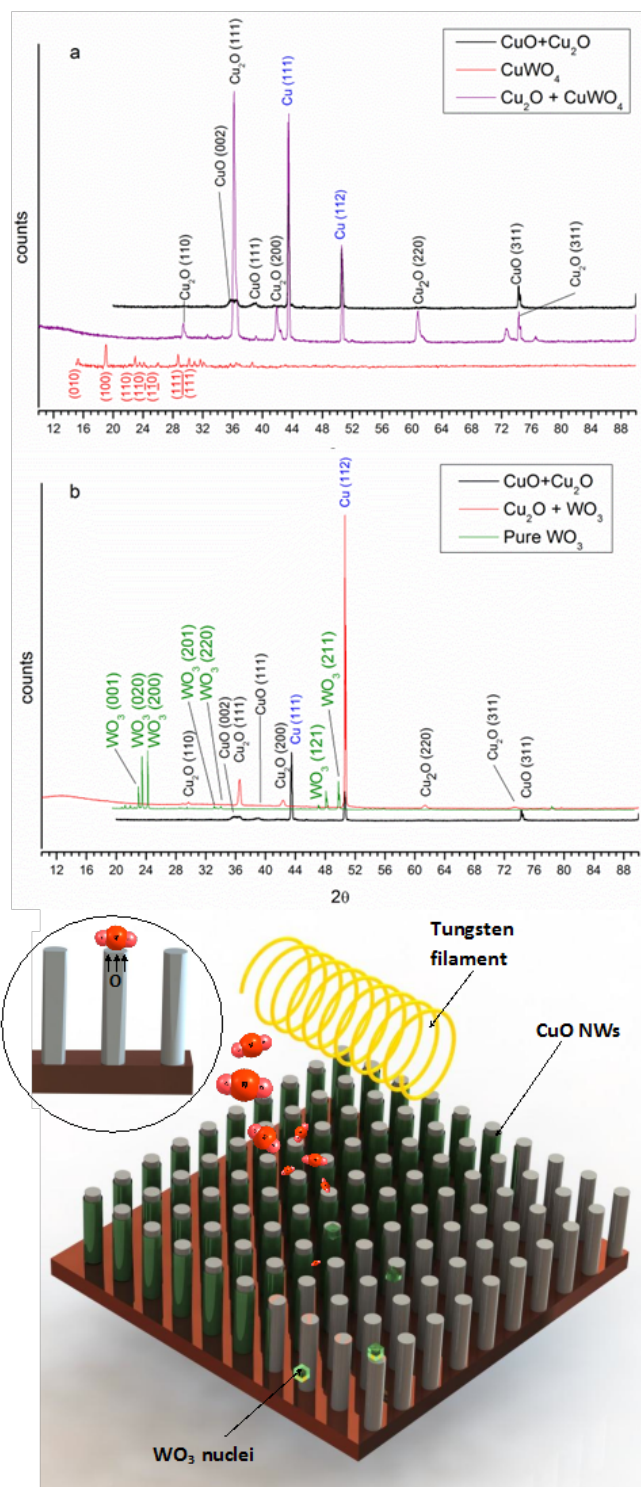


Figure 4.2 a) XRD of as deposited copper oxide nanowires (black), XRD of CuWO_4 film on fused silica (red), b) X-ray diffraction patterns CuWO_4 coated Cu_2O nanowire array (purple), c) redox model for copper oxide phase transformation.

The ends of this spring assembly were subjected to a potential bias of 20 VAC. With this configuration a uniform temperature was obtained throughout the whole filament assembly, achieving a stable source of both tungsten oxide and copper vapors for the deposition of CuWO_4 . At the filament temperatures obtained by resistively heating the wire assembly, metallic tungsten reacts with surrounding oxygen to produce volatile WO_x ; likewise red-hot metallic copper can release copper or copper oxide vapour. These vapors are transported at sub-atmospheric pressure towards the substrate where they react to form copper tungstate.

The WO_3 and the CuWO_4 deposits were made at a total pressure of 2.5 Torr in 16 sccm of 100% O_2 . The optical properties of the coated arrays were determined by UV-vis spectroscopy in diffuse reflectance mode using the Tauc plot method. SEM, EDAX and XRD were employed to characterize the morphology and composition. PEC characterization of the samples was performed with a three-electrode configuration in a PEC cell under 1.5AM illumination, using a Pt counter electrode and Ag/AgCl reference electrode (all measurements were carried out in pH 5 aqueous solution of Na_2SO_4 0.5M).

The as-synthesized copper oxide nanowire arrays appeared black and evenly covering the underlying metallic copper. Upon deposition of CuWO_4 or WO_3 the coating turned reddish-brown. Scanning electron microscopy (SEM) images show that the copper oxide wires (Figure 4.1 a) are typically between 1 and 2 μm long and around 20 nm in diameter. As shown in Figure 4.1b, the CuWO_4 coating on the Cu_2O nanowires present a faceted crystal shape, fully covering copper oxide wires from tips to bases. This type of growth suggests that an epitaxial layer is being deposited.

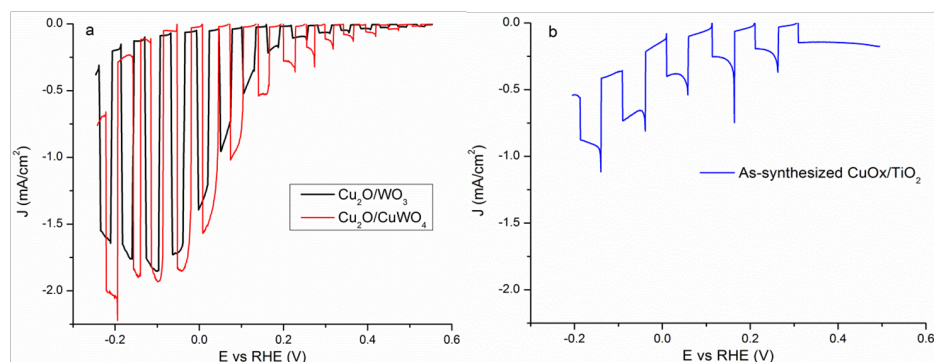


Figure 4.3 a) Linear sweep voltammogram for the WO_3 and CuWO_4 modified Cu_2O NW arrays and b) as-synthesized Cu_2O NW

The optical band gaps of the samples were determined by the Tauc plot method, shown here in Figure 4.1d. The black spectrum shows the indirect band gap of the copper oxide mixture of around 1.43 eV. This value is typical for CuO . Cu_2O nanowire arrays coated with CuWO_4 or WO_3 present direct band gap of around 2.0 eV. The increase in the band gap from 1.43 to 2.0, which results from annealing the as-synthesized copper oxide or from depositing WO_3 or CuWO_4 , suggests that the oxidation state of copper is reduced from Cu^{+2} to Cu^{+1} .

Analysis of the X-ray diffraction pattern (Fig. 4.2) showed that a mixture of CuO and Cu_2O phases results from the wet chemical oxidation and plasma treatment processes (shown in black). After deposition of either CuWO_4 or WO_3 , the underlying nanowires become essentially pure Cu_2O . A yellow film grown simultaneously on fused silica is triclinic CuWO_4 (Space Group: $\text{P}\bar{1}$). According to the diffraction pattern shown in red on Figure 4.2a, this material has cell parameters $a=4.668$ $b=5.792$, $c=4.881$ which are consistent with the values reported in the literature $a = 4.70953$, $b=5.84516$, and

$c=4.88492$ (PDF 088-0269). The experimental lattice parameters are in general agreement with the literature but slightly different owing perhaps to lattice mismatch. Elemental composition analysis using energy dispersive X-ray spectroscopy showed that the W to Cu ratio in this sample is 1:1. This ratio is consistent with the stoichiometry of CuWO_4 . The XRD patterns of polycrystalline films of CuWO_4 and WO_3 grown on planar substrates at the same temperature used for NW substrates are shown in

Figure 4.2 for comparison. The grain sizes of copper oxide before and after deposition of WO_3 were estimated using the Scherrer equation to be 4.5 and 9.0 nm, respectively.

Nn-heterojunctions of WO_3 and CuWO_4 on other photoabsorbers like BiVO_4 ⁵³ have been reported to aid in charge separation. In our prior work, we showed that titania coated Cu_2O nanowire photocathodes could produce a low current density of 0.26 mA/cm^2 , (at 0 vs. RHE) due to the presence of CuO as phase impurity. In addition, the amorphous titania coating deposited by atomic layer deposition could not minimize photocorrosion of the NW arrays probably due to poor charge transport. The current-potential (J-V) characteristics of n- WO_3 /p- Cu_2O and n- CuWO_4 /p- Cu_2O are compared in Figure 4.3a. Both electrodes performed similarly, with a maximum photocurrent of around 1.7 mA/cm^2 at a bias of -0.1 V vs. RHE, and their photocurrent onset are around 0.6 V vs. RHE, in either sample, which is comparable to the onset of Grätzel's multilayers with platinum catalysts.⁴⁸ By contrast, Gaillard et al. reported the onset of photocurrent at around 0.5 V vs. RHE. Correspondingly, $\text{Cu}_2\text{O}|\text{NiOx}$ nanocomposites³⁵ exhibit the onset voltage of photocurrent at 0.4 V vs. RHE.

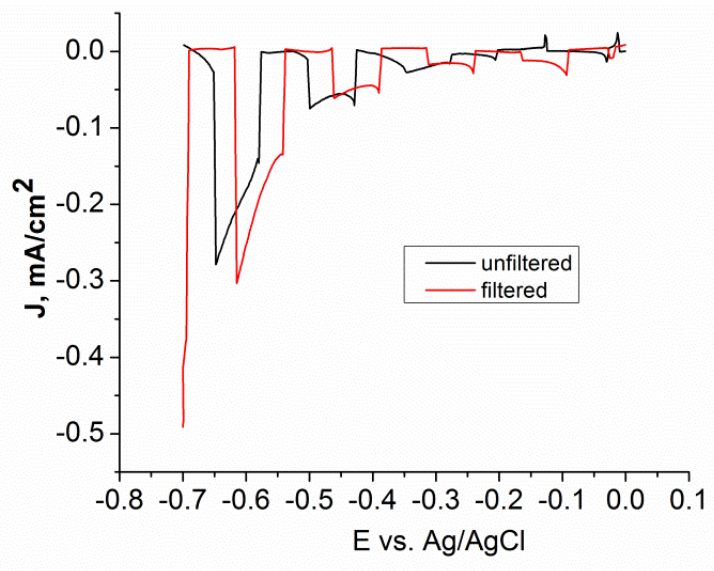


Figure 4.4 Chopped J-V curves for $\text{WO}_3/\text{Cu}_2\text{O}$

Also, the electrodes here presented outperform previous CuWO_4 coatings on CuO nanowires which present a photocurrent density of only -0.6 mA cm^{-2} (at about 0 V vs. RHE)⁹⁵. The J-V curves for the as-synthesized copper oxide nanowire arrays coated with titania is also included for comparison in Figure 4.3b. The reduced dark currents also suggest the lowering of photocorrosion due to the protective coating. Several factors could be responsible for this improvement in photocurrent density- (i) light absorption in the protective layer (ii) phase purity of Cu_2O (iii) improved charge separation caused by the pn junction. To investigate the contribution of charge carriers generated in the protective layers, we irradiated the $\text{WO}_3/\text{Cu}_2\text{O}$ electrodes with filtered light having wavelengths larger than 500 nm (2.5 eV), i.e. to limit the generation of carriers in WO_3 . It is apparent from Figure 4.4 that current densities in the filtered and unfiltered linear sweep voltammetry are very similar. Therefore, a contribution to the cathodic current coming from the WO_3 or CuWO_4 layer can be ruled out.

Phase pure Cu_2O samples were prepared by an approach suggested in the literature, comprising annealing copper hydroxide nanowires in nitrogen for 4 h ⁶⁴.

Figure 4.5 shows the scanning electron microscopy image, Tauc plot, X-ray diffraction pattern and chopped linear sweep voltammetry of the annealed samples.

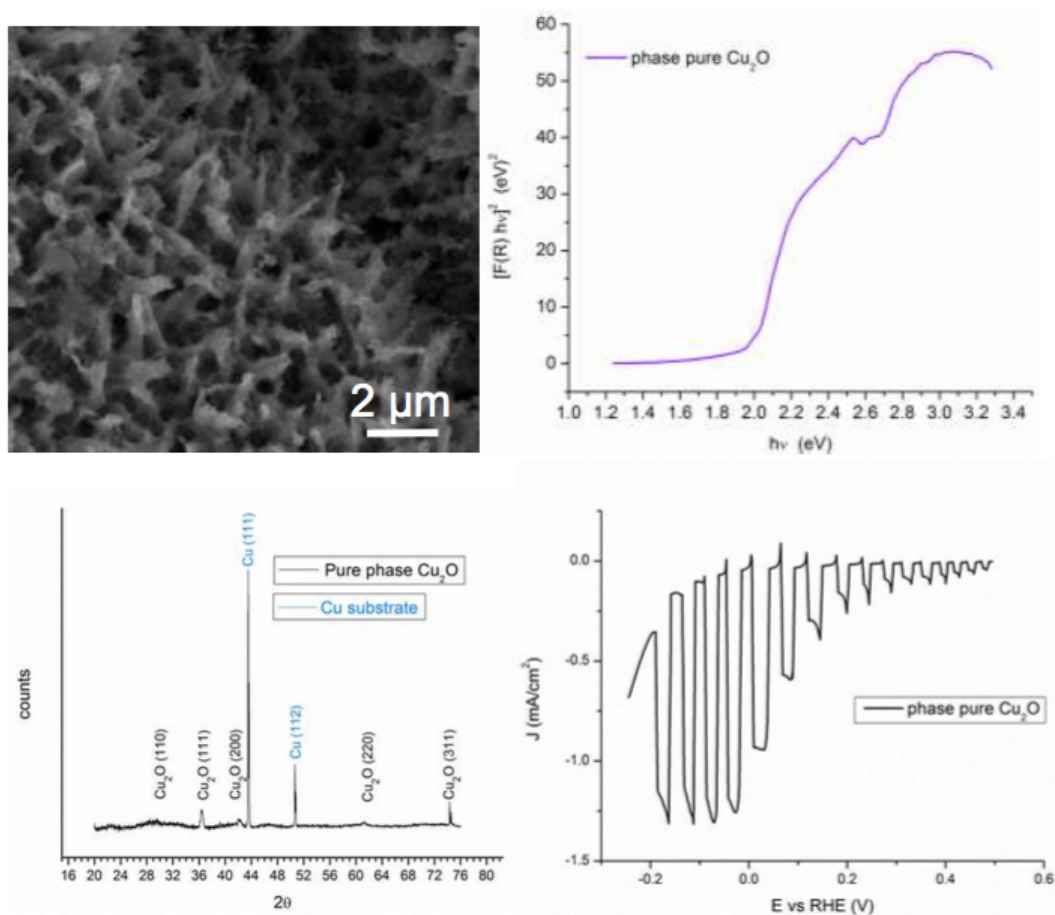


Figure 4.5 Phase pure Cu_2O a) SEM (tilt 45°), b) Tauc plot c)XRD, d) LSV at pH 5.

Although the process yielded phase pure Cu_2O , SEM imaging indicates the nanowire morphology is not well retained after the 4 h annealing treatment (Figure 4.5a). The J-V curve of a phase pure Cu_2O sample is shown in Figure 4.5d, and a current density of about 1.2 mA cm^{-2} is obtained at $\sim 0 \text{ V}$ vs. RHE. This result shows that

improving the phase purity has a tremendous effect on improving the photocurrent densities.

The deposition of WO_3 by HWCVD has shown that this process can easily fully reduce CuO to Cu_2O even when only pure oxygen is fed to the reactor, a condition that intuitively should make for a rather oxidizing environment. Interestingly, we have found that less than 10 minutes of exposure to a red-hot tungsten wire in oxygen can yield phase pure Cu_2O . This is extraordinary since reducing copper hydroxide in N_2 to Cu_2O is not straightforward (for it takes around 4 hours at 550°C to accomplish), let alone transforming CuO to Cu_2O in N_2 only.

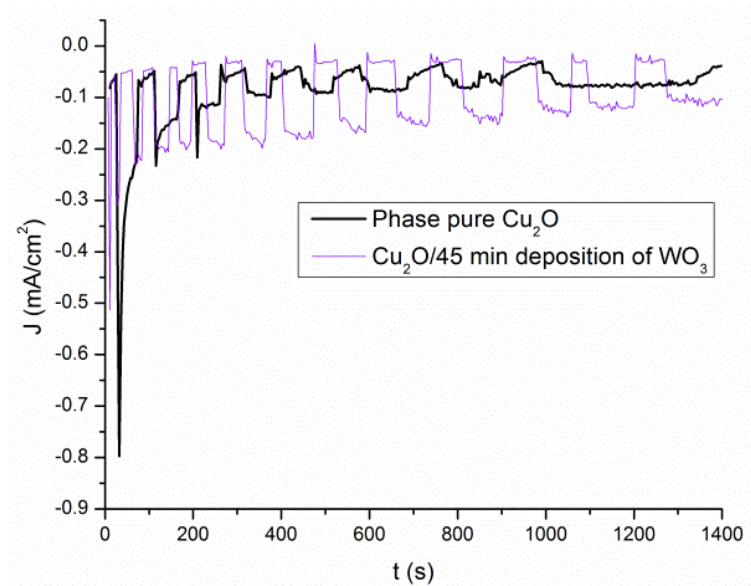
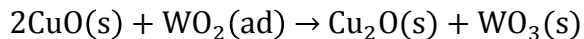
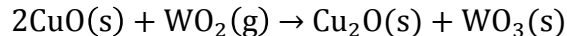


Figure 4.6 Chronoamperometry at -0.5 V vs. Ag/AgCl , for un-coated phase pure Cu_2O (black) and 45 minute deposition of WO_3 on Cu_2O (purple).

Thangala et al. has reported that hot tungsten filaments produce gaseous WO_2 , which diffuses at low pressure to the substrate where it is further oxidized to crystalline

WO₃.⁹⁶ This oxidation and condensation could be the driving force for the phase transformation of CuO, according to either of the following reactions:



We estimated the ΔG_r (at 673 K and a WO₂ partial pressure of 8×10^{-7} torr) for the former chemical reaction to be around -660 kJ/mol of WO₂, and of -130 kJ/mol for the later. The Gibbs free energy calculation also suggest that WO₂ could act as an oxygen scavenger at the CuO nanowire bulk where diffusion of oxygen over small length scales of the nanowires is easy and where gaseous WO₂ readily accesses a huge surface area due to the nanowire array morphology. To confirm this hypothesis, we annealed the as-synthesized mixed-phase copper oxide at the same temperature, pressure and oxygen flow conditions as those for WO₃ deposition, with exception of the hot tungsten filament. This experiment did not yield phase pure Cu₂O even after 3 hours of exposure.

The mechanism of formation of CuWO₄ is open for speculation. However, it is believed that in the conditions of these experiments, tungsten oxide vapors and copper vapors will be transported from the incandescent filaments to the cooler substrates where they react heterogeneously on the surface to produce CuWO₄. It is quite evident that using the W-Cu filament assembly leads to a yellow deposit on the reactor walls and on fused silica substrates, whereas only employing the W filament leads to a white but slightly green layer of WO₃. This observation is confirmed by the X-Ray Diffraction patterns of samples grown on fused silica (red diffraction pattern for CuWO₄ and green diffraction pattern for WO₃ in

Figure 4.2 a and b)

The transient open-circuit potential measurements of Cu_2O NW arrays with a crystalline WO_3 or CuWO_4 coating indicate that the illuminated potential is at more positive values than in the dark, as observed in Figure 4.7.

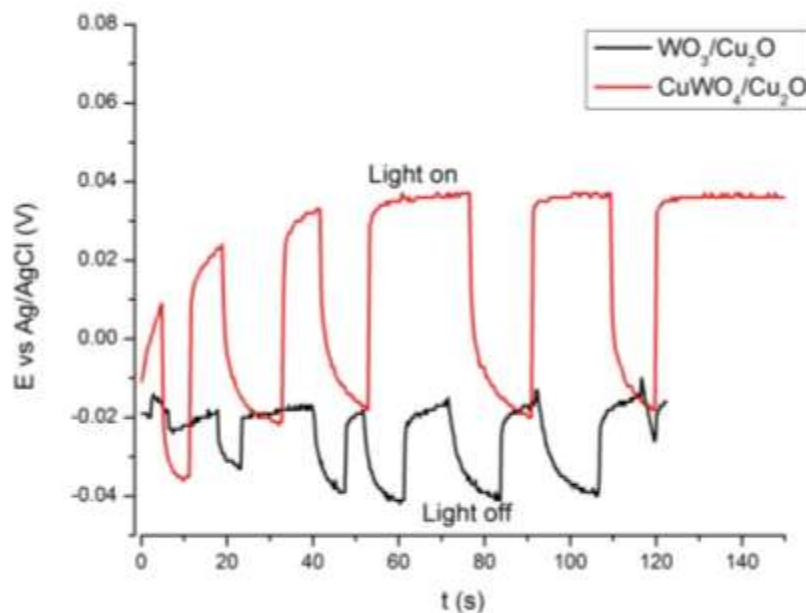


Figure 4.7 Transient open-circuit voltage for the CuWO_4 , WO_3 coated Cu_2O NWs.

This behavior is typical of p-type semiconductors, where excess photogenerated holes dominate the conduction processes in the material. Current density – potential characteristics under chopped illumination were performed on Cu_2O arrays coated with WO_3 of increasing thickness obtained by depositing WO_3 onto Cu_2O for 15, 45, and 120 minutes, respectively. Thus, the resulting WO_3 film ranged from thin epitaxial layers to thick films that fully buried the Cu_2O nanowire array. It is readily apparent from Figure 4.8 that the highest photocurrents are present in the $\text{WO}_3/\text{Cu}_2\text{O}$ sample (15 min deposit).

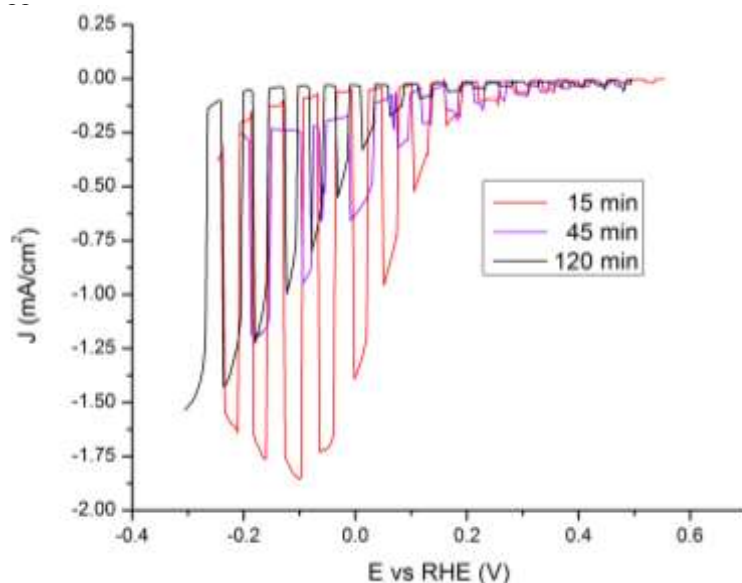


Figure 4.8 LSV for $\text{Cu}_2\text{O}/\text{WO}_3$ photocathodes; 15 min deposition of WO_3 (red), 45 min deposition of WO_3 (purple), 120 min deposition of WO_3 (black)

This suggests that the electron-hole pairs generated in the p-type semiconductor drift in the field and are more effectively separated by the bent bands than in the non-depleted regions within the bulk of the thicker films (120 minute deposit) where recombination is more prominent. Also the thick films grown during 45 and 120 minutes are more likely to be polycrystalline, which would present abundant traps at the grain boundaries.

Figure 4.6 presents chopped chronoamperometry for an un-coated phase pure Cu_2O and also a $\text{Cu}_2\text{O}/\text{WO}_3$ electrode (45 minute deposit). The current density in the uncoated Cu_2O sample (black) decayed very quickly to around 15% of the initial value in less than 100 seconds.

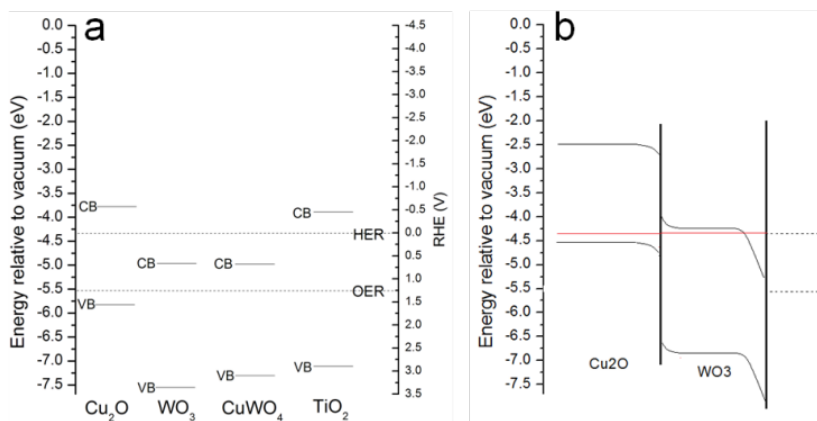


Figure 4.9 a) Band edge positions of Cu_2O , WO_3 , CuWO_4 , TiO_2 and at pH=5 before equilibration; b) Band diagram after equilibration in the dark at 0 V vs. RHE.

This results from the reduction of Cu_2O to metallic copper caused by photogenerated electrons and the limited injection of same to the electrolyte. Upon coating with WO_3 a protective effect is seen as evidenced by the retention of 30% of initial photocurrent to about 1400 seconds. This improvement might be a result of limiting the accumulation of electrons at the Cu_2O interface and injection of these into the WO_3 bands. Interestingly, the uncoated Cu_2O presents marked spikes in each illumination cycle being this evidence of carrier accumulation at the Cu_2O interface. This feature can be explained qualitatively as follows: in the uncoated sample, photogenerated electrons tend to build up in Cu_2O near the interface as they are swept in the space charge region, until they are transferred or undergo recombination. Before a steady state concentration is reached under illumination, majority holes – that would normally move towards the counter electrode – recombine, thus creating the spike⁹⁷.

Figure 4.9a shows the conduction and valence band positions relative to the oxidation and reduction potentials of water. Figure 4.9b presents the band diagram of a

pn-heterojunction formed by Cu_2O and WO_3 , in equilibrium with the electrolyte. In illumination the Fermi level at the pn-junction splits and application of forward bias shifts the bands of Cu_2O such that the potentials for hydrogen and oxygen evolution are straddled. In this condition photogenerated electrons move towards WO_3 and into the electrolyte. Holes travel around the circuit to the counter electrode where they perform water oxidation. The Fermi level lies above of conduction band of WO_3 thus promoting uptake of electrons by the electrolyte.

It is apparent from the results of this study that the coated Cu_2O electrodes benefit from the protective effect of WO_3 as a barrier is formed to prevent the dissolution of Cu_2O in the electrolyte, thereby extending the durability. Further, WO_3 is more resistant to photocorrosion by minority electrons owing to the fact that, unlike Cu_2O , the WO_3 reduction potential is above its conduction band minimum⁴¹. Additionally, the high crystallinity of the n-type WO_3 provides for faster charge transport and better carrier separation. Phase purity of Cu_2O - that results from the reducing effect of WO_2 during deposition of WO_3 – is key to bettering the current density of the electrodes. The current densities and durability can be further improved by depositing a HER catalyst.

CHAPTER 5

GROWTH AND PHOTOELECTROCHEMICAL CHARACTERIZATION OF GASB_xN_{1-x} FILMS FOR PEC

5.1. MOCVD Tool improvement

In order to have a sharp compositional control at the interfaces of the samples, the MOCVD tool was revamped to enable venting the lines during the course of the experiment until proper growth conditions are attained in the reactor run lines. For epitaxy it is desired to precisely regulate the amount of precursors into the growth chamber. Factors to be considered in the redesign of the gas handling systems included minimizing transients caused by perturbations in pressures, temperatures and carrier gas flows to facilitate the two-step growth methodology. The gas distribution network should ideally have minimum dead space, and should be easy to leak check.

5.1.1 Run/vent operation

The lengths of the precursor lines were reduced to minimize the dead space and residence times. A three-way valve (V9) was added right before the gas manifold (which mixes the process gases) to adapt a vent line connected directly to the reactor exhaust, in order that the precursor gases could be bypassed when the composition transients were still present.

The reasoning for this new network arrangement is that the line pressure and carrier gas flow in the metalorganic bubbler can be maintained at constant values during growth, and steady precursor flows can be established in the lines, therefore eliminating the transients when the source is switched into and out of the reaction chamber.

5.1.2 Extrinsic doping

New gas connections were added to the main manifold of the gas-handling network for feeding controlled amounts of Silene in H_2 .

5.2. $GaSb_xN_{1-x}$ characterization

Preliminary deposition experiments performed without buffer layers were carried out at an GSR of 1:42 and high TMGa flux, led to the deposition of a partially textured thick films with polycrystalline overgrowth, with poor incorporation of Sb and no band gap reduction beyond 800°C. A summary of typical deposits is presented in Figure 5.1.

The deposit grown at 775°C is approximately 1.5 micrometers thick. About the first 700 nm show polycrystallinity, but as the film grows thicker there are signs of initial stages of texturization because certain triangular facets are apparent near the surface.

The top view of this deposit (Figure 5.1c) shows two superimposed kinds of structures. The underlying layer is continuous and presents a high roughness giving the film the appearance of a network of “ridges and valleys”. On top of that surface, bigger, isolated crystals project upward and appear to be oriented randomly with respect to the others.

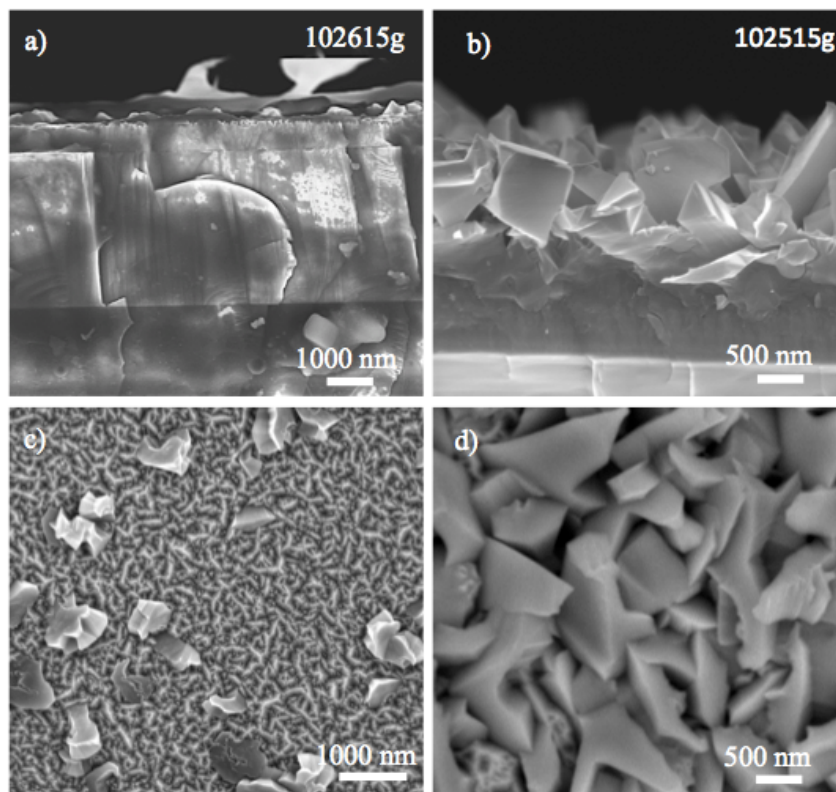


Figure 5.1 a) cross-sectional micrograph of $\text{GaSb}_x\text{N}_{1-x}$, 775°C c) Top surface of $\text{GaSb}_x\text{N}_{1-x}$ grown at 775°C without buffer layers b) Cross-sectional micrograph of GaN 850°C , d) GaN grown 850°C without buffer layers.

The sample grown at 850°C shows a polycrystalline film with large grains growing in random directions. This apparently very disorganized growth suggests that the concentration of adducts is too high, that there is formation of new nuclei at all the stage of growth of the film, and that the fastest growing planes of the seed nuclei are not aligned.

Photoelectrochemical characterization of films with this less-than-ideal morphology, but with 2 eV band gaps, showed that the open circuit potential was drifting negatively and stabilized under illumination at about 1.1 V vs RHE. The flat band potential according to Mott-Schottky measurements in sodium sulfate at pH 9 and 100

kHz was determined to be 1.2 V vs RHE. While these materials showed n-type conductivity, the maximum photovoltage obtained at 1 sun illumination never exceeded 40 mV and the maximum photocurrent density measured at 1.2V vs. RHE was $1 \mu\text{A cm}^{-2}$.

These results demonstrate that the band edges of this film, at pH 9, do not straddle the redox potentials of the water splitting half-reaction. In fact, the conduction band position is located just above the oxygen evolution reaction by about 30 mV.

Epitaxial growth of $\text{GaSb}_x\text{N}_{1-x}$ films has been attempted by carrying out a sensitivity analysis of the deposition temperature at the substrate.

Difficulty to incorporate Sb atoms into the lattice of GaN at high temperature results from differences between the adsorption/desorption rate constants of Sb and Ga adducts after the metalorganic precursors undergo pyrolysis in the MOCVD chamber. The present results suggest that the antimony adducts, have a lesser “stickiness” to step edges compared to gallium.

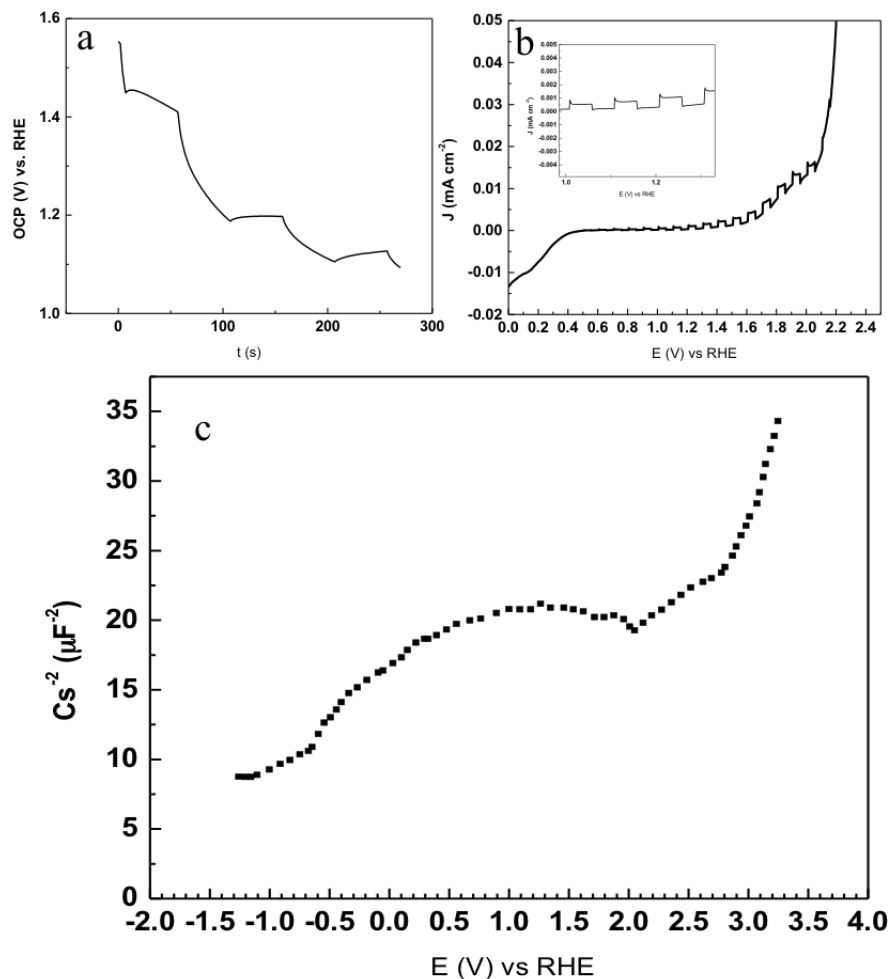


Figure 5.2 Photoelectrochemical characterization of textured films, $E_g = 2$ eV a) OCP, b) chopped J-V curve, c) Mott-Schottky Plot (dark), 100 kHz.

In an attempt to overcome this limitation, the TMGa to TMSb ratio (**GSR hereinafter**) was modified to compare the deposit morphologies grown in Sb-rich versus Sb-poor ratios. The GSR was studied from 1:1 to 1:18 at moderate temperatures between 800-900°C. A three-stage growth temperature profile was implemented, consisting of i) annealing of substrate for 20 min at 900°C in ammonia, followed by ii) buffer layer growth at 500 °C for 5 minutes, iii) film growth at target deposition temperature.

Figure 5.3 summarizes the results of the experimental matrix with two independent variables, Growth Temperature (GT) and Ga-to-Sb ratio (GSR), with 4 and 5 levels, respectively. Column 1 shows the SEM cross-sectional views of samples grown at 825°C at increasing levels of GSR's. As the SGR increases, the TMGA flux is reduced from 18 to 4 micromoles min⁻¹ due to constraints imposed by the metalorganic precursor vapor pressure, pressure in the bubbler and maximum carrier gas flow rate. Each micrograph is identified with a unique label (with six digits followed by the letters **s** or **g**). These denote the substrate: **s** for sapphire and **g** for gallium nitride. A more comprehensive set of images is presented in the discussion. Row 4 illustrates a set of samples grown at a constant GSR ratio of 1:12, at increasing substrate temperatures.

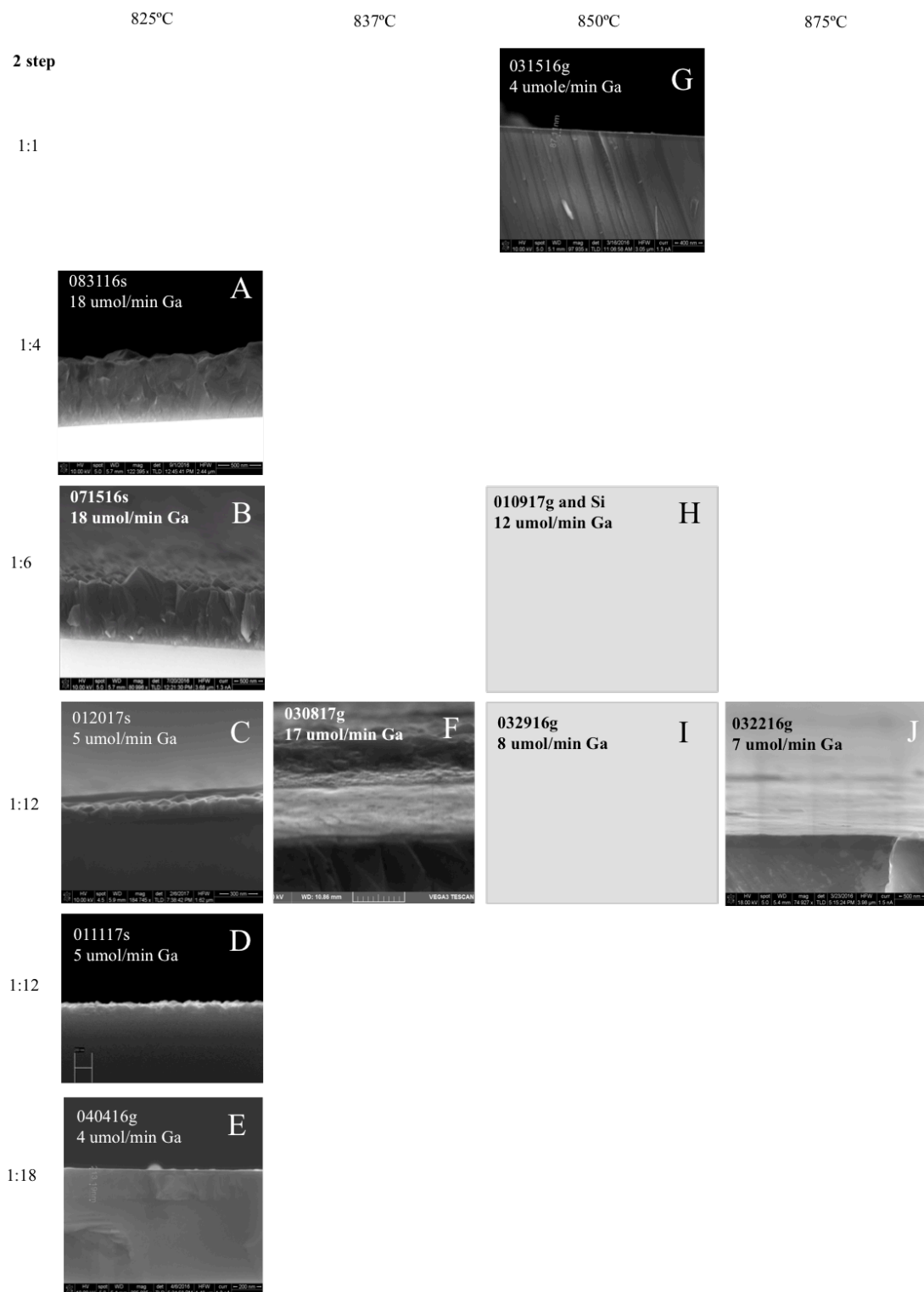


Figure 5.3 Matrix of experiments in the GSR and Substrate temperature space.

Sample A (083116), grown at a TMGa flux rate of 18 $\mu\text{mol/min}$ has an average thickness of 1 μm . The growth rate of this polycrystalline film was estimated to be 0.7 $\mu\text{m hr}^{-1}$. From the cross-sectional view it is apparent that initially there is a high nucleation density of crystallite seeds with size of around 10-50 nm, forming isolated islands. Layer by layer growth on the islands leads to localized epitaxy on each island and competitive growth as the grains coarsen. The x-ray diffraction pattern (Figure 5.4) reveals that this film grown on Sapphire has strong texturing or preferred orientation of the grains. The mechanisms controlling the development of the preferred orientation is referred to as the principle of evolutionary selection. In the absence of secondary nucleation, some of the grains in a growing polycrystalline film have an orientation such that the fastest growing direction is perpendicular to the substrate surface. This allows these isolated crystals to dominate the morphology as the film grows. The rest of grains that do not have that particular orientation die out as they grow into the sides of the favorably oriented grains.⁹⁸ In this thick film the crystal facets align with each other leading to larger crystals with a preferred orientation in the $\langle 002 \rangle$ direction perpendicular to the basal c-plane of GaN. The seed crystallite size was estimated to be 34 nm as Scherrer's equation provides an estimated of the lower bound of the particle size, which is consistent with the nuclei observed in scanning electron micrographs.

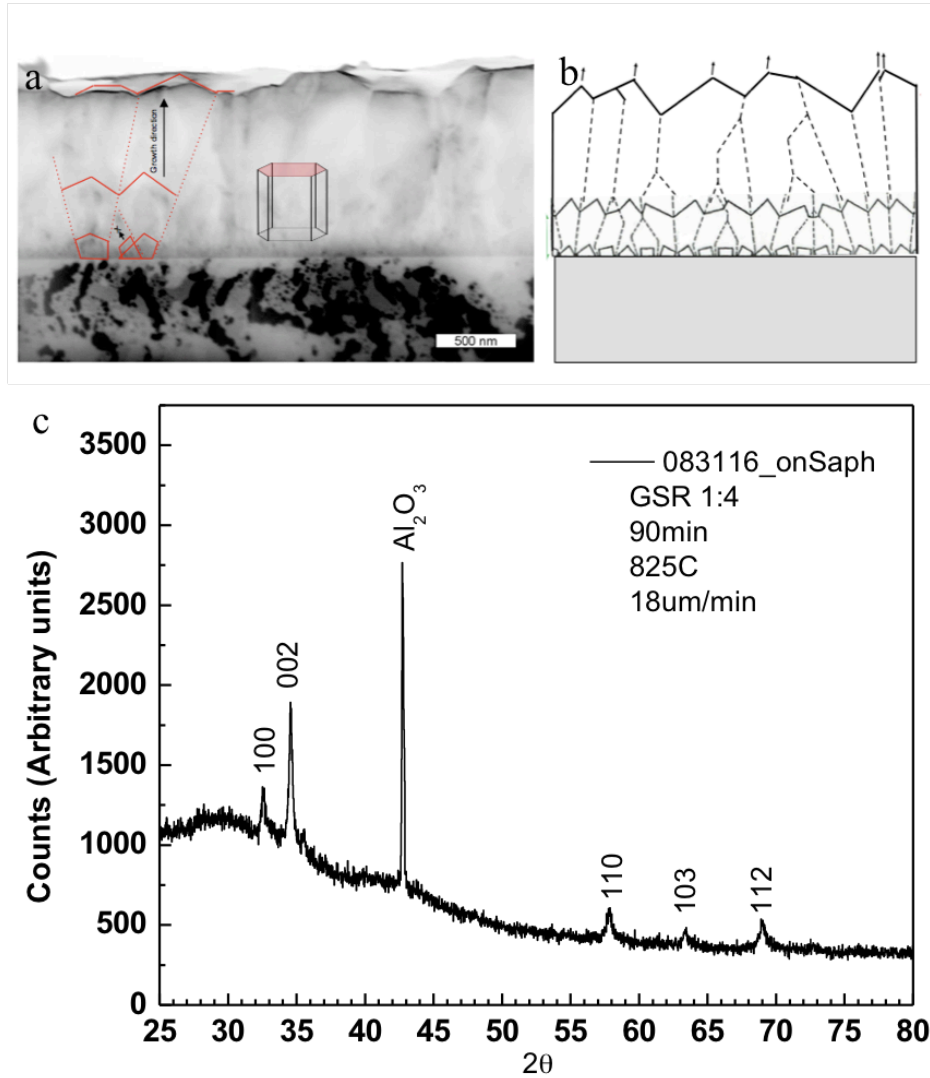


Figure 5.4 A) Sample A (083116) cross section, 825°C. b) evolution of microstructure in GaSbN, (Adapted from S. Sunkara⁸⁰) c) XRD

The preferred orientation in the $\langle 002 \rangle$ direction becomes apparent when noting that the most intense peak in a h-GaN standard powder is the 101 signal (with 100% intensity), followed by the 100 reflection (with 47%) (PDF 01-089-7522). In the present case, the most intense peak is the 002 reflection corresponding to the basal plane of $\text{GaSb}_x\text{N}_{1-x}$, as shown in Figure 5.4 above. The 002 peak is slightly shifted negatively 216

arcseconds (0.06°) with respect to epitaxial GaN/Sapphire. This fact along with the expansion of the lattice parameter by 0.2% suggest that at an GSR of 1:4 there is still very little incorporation of Sb.

Samples B, C, and D, grown at 825°C with increasing SGR's, all have optical band gaps between 1.65 and 1.75 eV. Samples B and B* (071516s and 071516g), were grown at a TMGa molar flux of $11\ \mu\text{mol/min}$. They contain around 2.5% Sb. On sapphire the average growth rate of the ternary film was $1200\ \text{nm hr}^{-1}$, with a thickness of 960 nm. The relative intensity of the 002 reflection (Figure 5.5) is even higher than of sample A, and presents a high degree of texturization on sapphire. Its smallest feature size was estimated to be 77 nm. Sample (071516g) (

Figure 5.6b) grown on GaN has a smaller thickness of about 400 nm, and appears more polycrystalline and due to its small thickness, the evolution of a preferred orientation observed in the sapphire grown sample is not as evident. A broadening of the 002 reflection of the underlying GaN substrate suggests that the smallest feature size of the $\text{GaSb}_x\text{N}_{1-x}$ layer is about 28 nm.

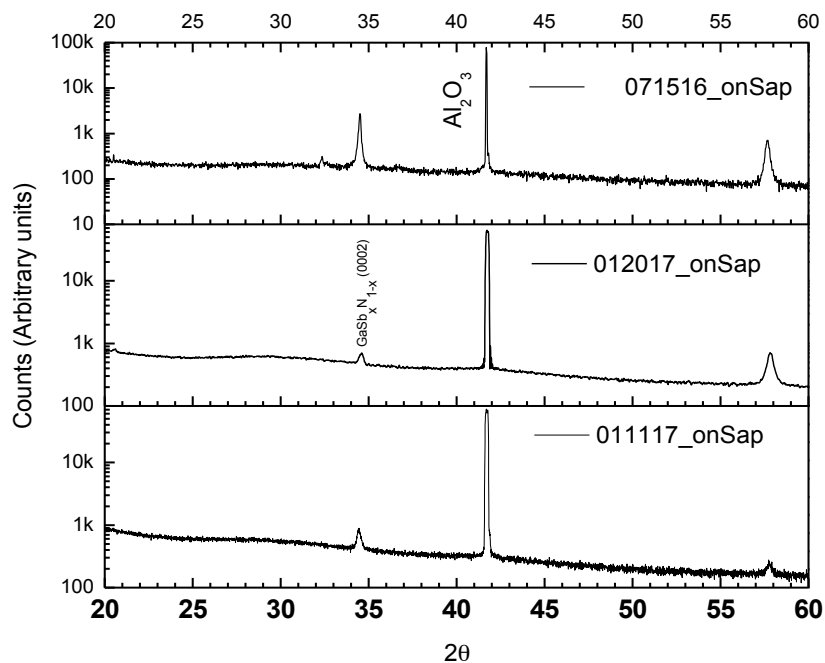


Figure 5.5 XRD of Samples B, C, D on Sapphire.

In order to maximize the SGR ratio, the flux of TMGa precursor fed to the reactor was restricted to $5 \mu\text{moles min}^{-1}$. While this solution favored the incorporation of Sb, it also considerably reduced the film growth rate to about 50 nm hr^{-1} , which limited the deposits to ultra thin films.

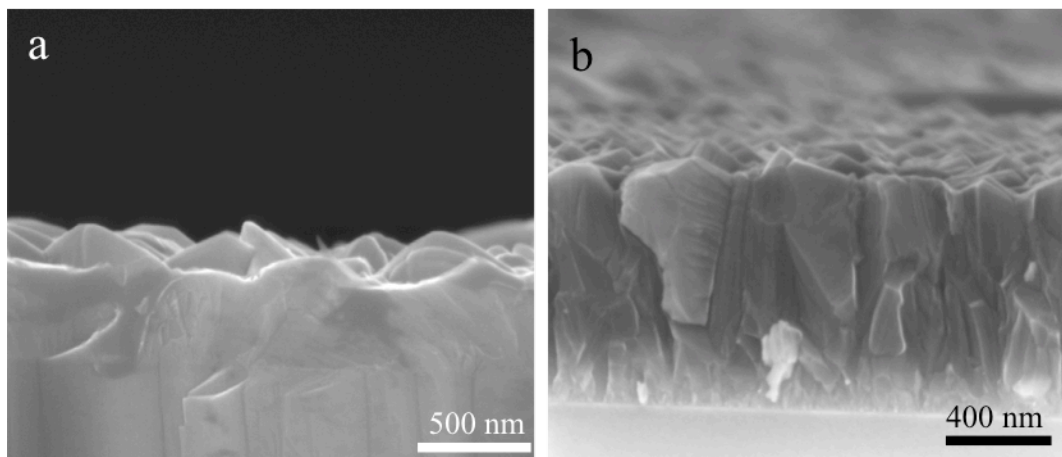


Figure 5.6 Cross-sections of Samples B, 071516g and 071516s, a) on Sapphire a) on GaN

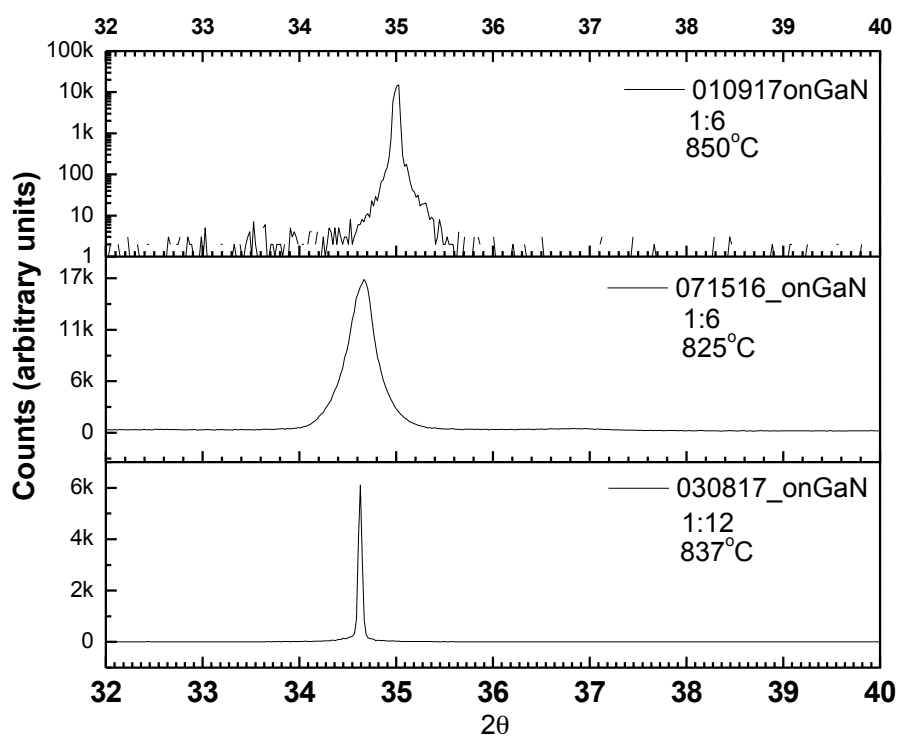


Figure 5.7 XRD 010916G and 071516g and 030817g

Sample C (011117g) and D (012017g) (see Figure 5.8) with thicknesses of about 50 nm only show the first stages of nucleation and initial crystallite growth of $\text{GaSb}_x\text{N}_{1-x}$

on GaN. Both samples were grown at 825°C with a GSR's of 1:12, Ga molar flux of 5 $\mu\text{mol}/\text{min}$, for 30 and 120 min, respectively. They both contain about 2.5% Sb and band gap of 1.75 eV. The average growth rate was estimated to be 50 nm hr^{-1} . This very slow growth rate is caused by the off-centered position of the substrates on the susceptor along with the suppressed flux TMGA precursor.

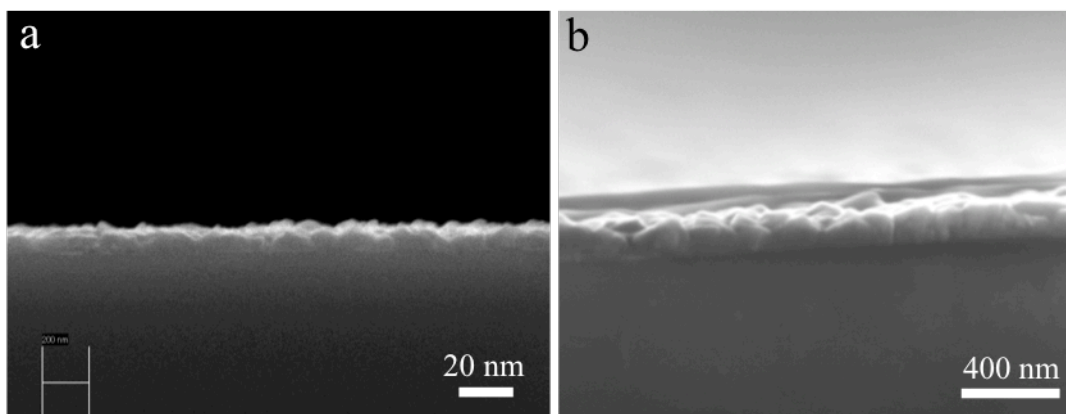


Figure 5.8 SEM of Sample C (011117g) 30 min reaction, Sample D (012017g) 120 min reaction.

XRD analysis was performed on these samples showing only refraction peaks for the basal plane of c-GaSbN and the (1120) plane located at 57.7 degrees, as well as the very intense sapphire peak (see Figure 5.5) above.

For Sample E, a low temperature amorphous buffer layer was grown on n-GaN for 10 min, at a temperature of 500°C. Later, the susceptor temperature was ramped up to 825°C and a SGR of 18:1 with 4 $\mu\text{mol}/\text{min}$ of TMGa were fed to the reactor for 1 hour. This process led to the growth of a single crystalline film (Figure 5.9) of $\text{GaSb}_x\text{N}_{1-x}$ with a band gap of 1.8 eV and an estimated Sb concentration of 2% (Figure 5.11).

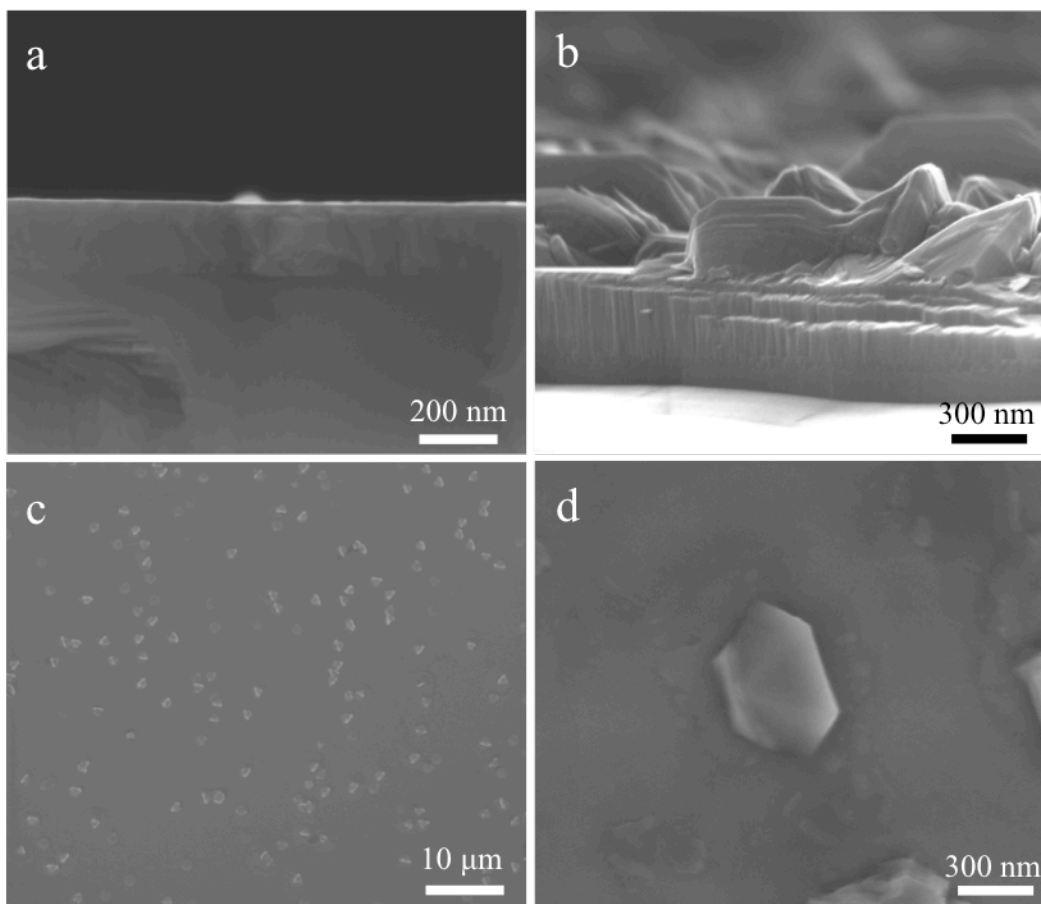


Figure 5.9 Sample E. 825°C, GaSbN on GaN, 18:1, 4 $\mu\text{mol min}^{-1}$. a) cross-section, b) tilted cross-section (overgrowth) c, d) top views.

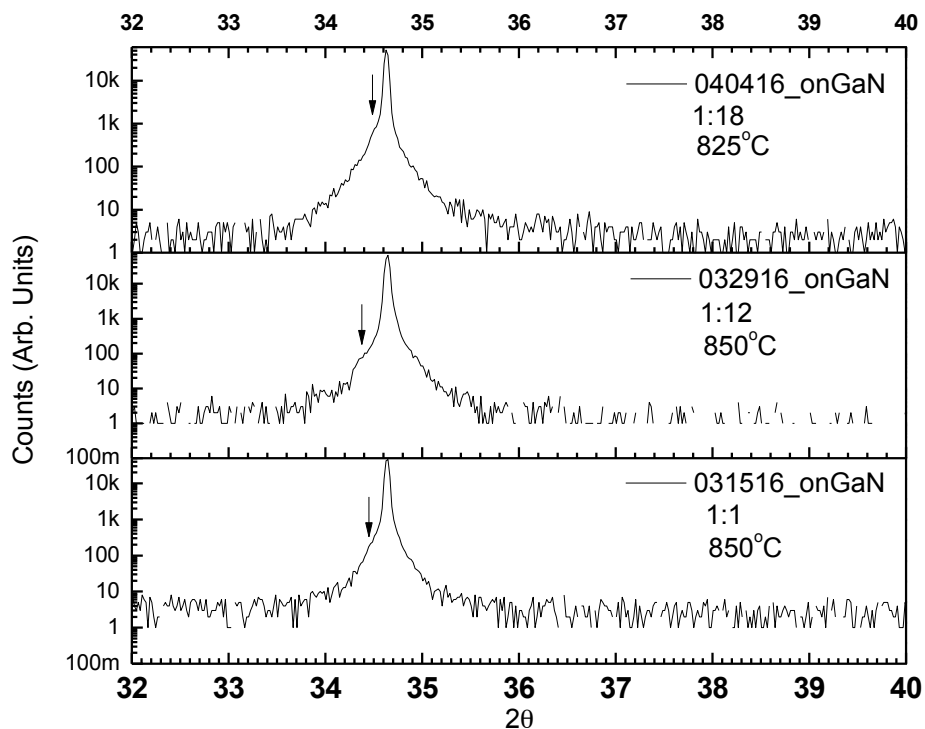


Figure 5.10 XRD pattern for Sample E,. 040416 825C, GaSbN on GaN, GSR 1:18, 4 $\mu\text{mol min}^{-1}$. Diffraction patterns of Samples G and I also shown for comparison.

The direct band of Sample E (040416g) on GaN was determined to be 1.8 eV.

To gain better understanding of the structure of the ternary layers deposited using the two-step growth method, the c-lattice constant for $\text{GaSb}_x\text{N}_{1-x}$ with different Sb concentration levels was calculated to determine the lattice mismatch strain f.

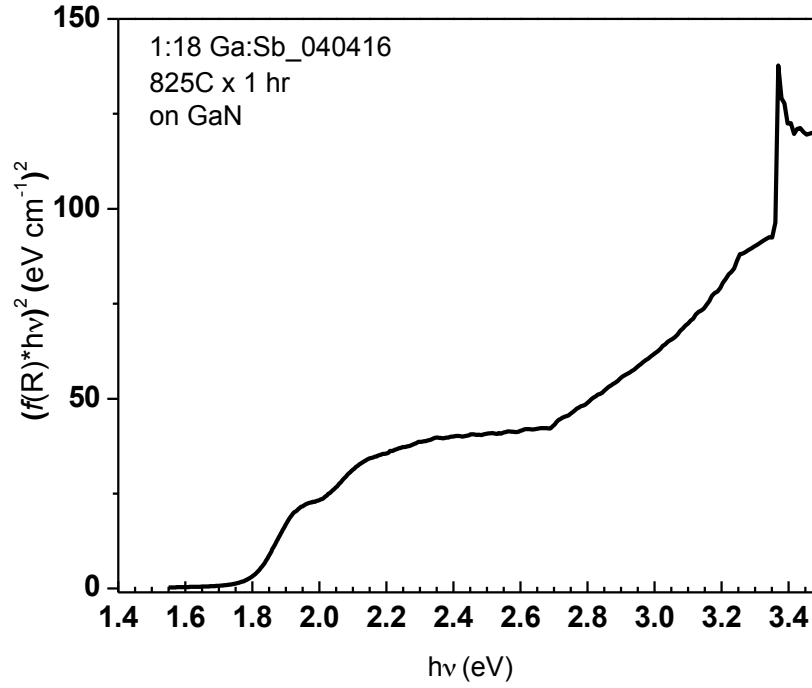


Figure 5.11 Tauc plot Sample E. 040416 825C, GaSbN on GaN, 18:1, 4 $\mu\text{mol min}^{-1}$.

From Bragg's law, and the interplanar spacing equation for hexagonal systems:

$$\sin^2 \theta = \frac{\lambda^2}{4d^2}$$

$$\frac{1}{d^2} = \frac{4}{3} \left(\frac{(h^2 + hk + k^2)}{a^2} \right) + \frac{l^2}{c^2}$$

We know that,

$$\sin^2(\theta) = \left(\frac{\lambda^2}{4} \right) = \frac{4}{3} \left(\frac{(h^2 + hk + k^2)}{a^2} \right) + \frac{l^2}{c^2}$$

For the (0002) plane in the Miller-Bravais index notation, simplified as (002)

(since $h+k+i=0$), Bragg's law for the hcp structure becomes (after factoring $1/a^2$):

$$\sin^2(\theta) = \frac{\lambda^2}{4a^2} \left[\frac{4}{3}(h^2 + k^2 + l^2) + \frac{l^2}{\left(\frac{c}{a}\right)^2} \right] = \frac{\lambda^2}{4a^2} \left[\frac{l^2}{\left(\frac{c}{a}\right)^2} \right] = \frac{\lambda^2 l^2}{4c^2}$$

$$4c^2 = \frac{\lambda^2 l^2}{\sin^2(\theta)}$$

Therefore,

$$c = \frac{\lambda l}{2 \sin(\theta)}$$

Where, $\lambda = 1.5406 \text{ \AA}$,

$l = 2$ and θ is the Bragg angle for the [002] peak.

For films of GaSbN on sapphire grown at 825°C it is possible to very accurately estimate the c-parameter of the unit cell in $\text{GaSb}_x\text{N}_{1-x}$. For these samples grown with increasing levels of GSR a change of 0.2% in the lattice parameter was observed, which is consistent with the band gap of between 1.7 - 1.8 eV observed by UV-vis spectroscopy. Estimation of the lattice parameter of the samples grown on GaN, particularly of the thin films below 200 nm thick, proved to be more challenging because only a few lattice planes of the GaSbN layer will refract and the penetration depth of the X-ray beam is greater than the thickness of the material, so the signal is dominated by the refraction of the underlying GaN substrate. The peak shift appears as a left shoulder of the main diffraction signal of epitaxial GaN. A similar of lattice expansion is observed for these samples grown on GaN as shown in Figure 5.12 below.

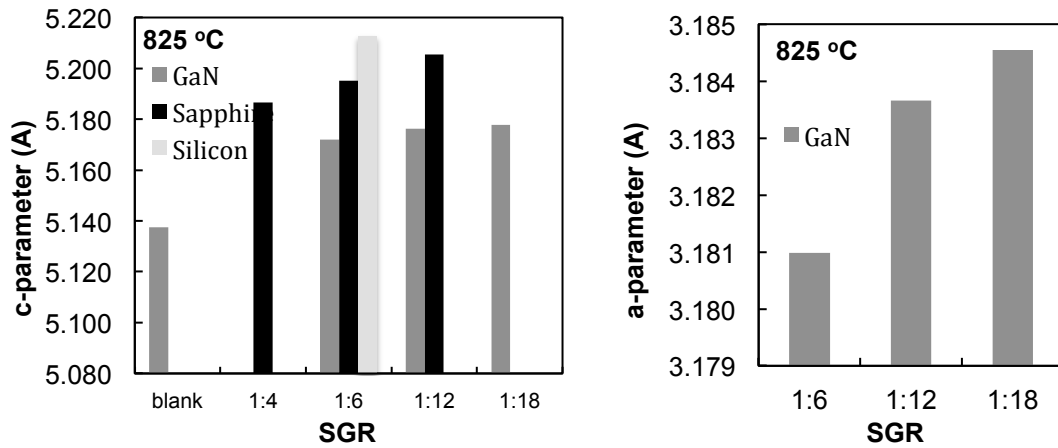


Figure 5.12 Lattice constants of $\text{GaSb}_x\text{N}_{1-x}$ films grown at increasing levels of TMGa to AMSb.

The lattice parameter of a $\text{GaSb}_x\text{N}_{1-x}$ sample grown on silicon wafer was estimated to be around 5.21 Å. All samples of this batch (GSR 1:12, 825°C) have the same lattice parameter irrespective of the substrate used, as shown by the bar graph, (Figure 5.12) above.

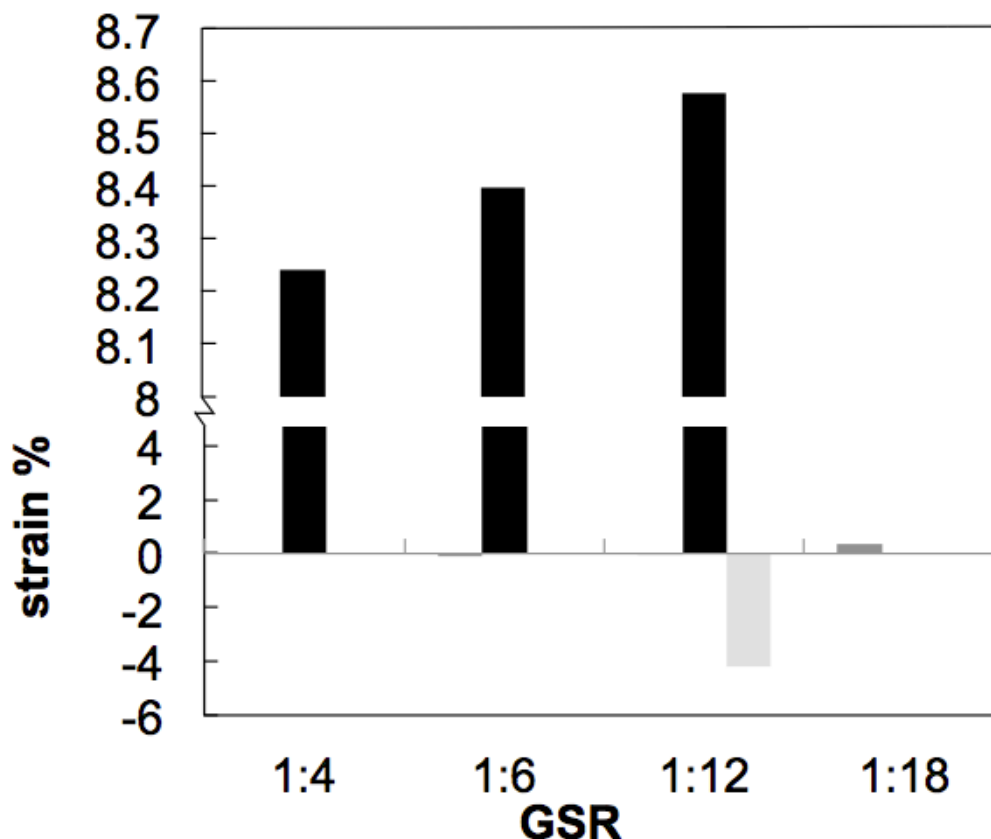


Figure 5.13 Percent strain in the c-direction of GaSbN films grown at 825C at different GSR values. (Black: Sapphire, dark grey: GaN, light grey: silicon)

The bar graph in Figure 5.13 for this set of these isothermally grown samples show an interesting difference between the percent strain of $\text{GaSb}_x\text{N}_{1-x}$ as a function of the substrate used for deposition. The GaSbN samples grown on GaN show almost zero percent strain as the lattice the sample and the substrate are quite similar. All samples grown on sapphire, however, are highly strained with a magnitude of about 8%. This value is very close to the limit commonly associated to onset of plastic relaxation, which induces propagation of defects in the c-direction. By contrast, the deposit grown on (001) Silicon presents a strain of 4% (negative in magnitude). This can be understood more easily visually in terms of the unit cells.

Silicon has a diamond cubic lattice with parameter $a=5.43$ Å, but the distance between co-planar atoms in the (111) plane is 3.84 Å. The projections normal to the (100) and (111) planes are shown below (Figure 5.14a and b, respectively).

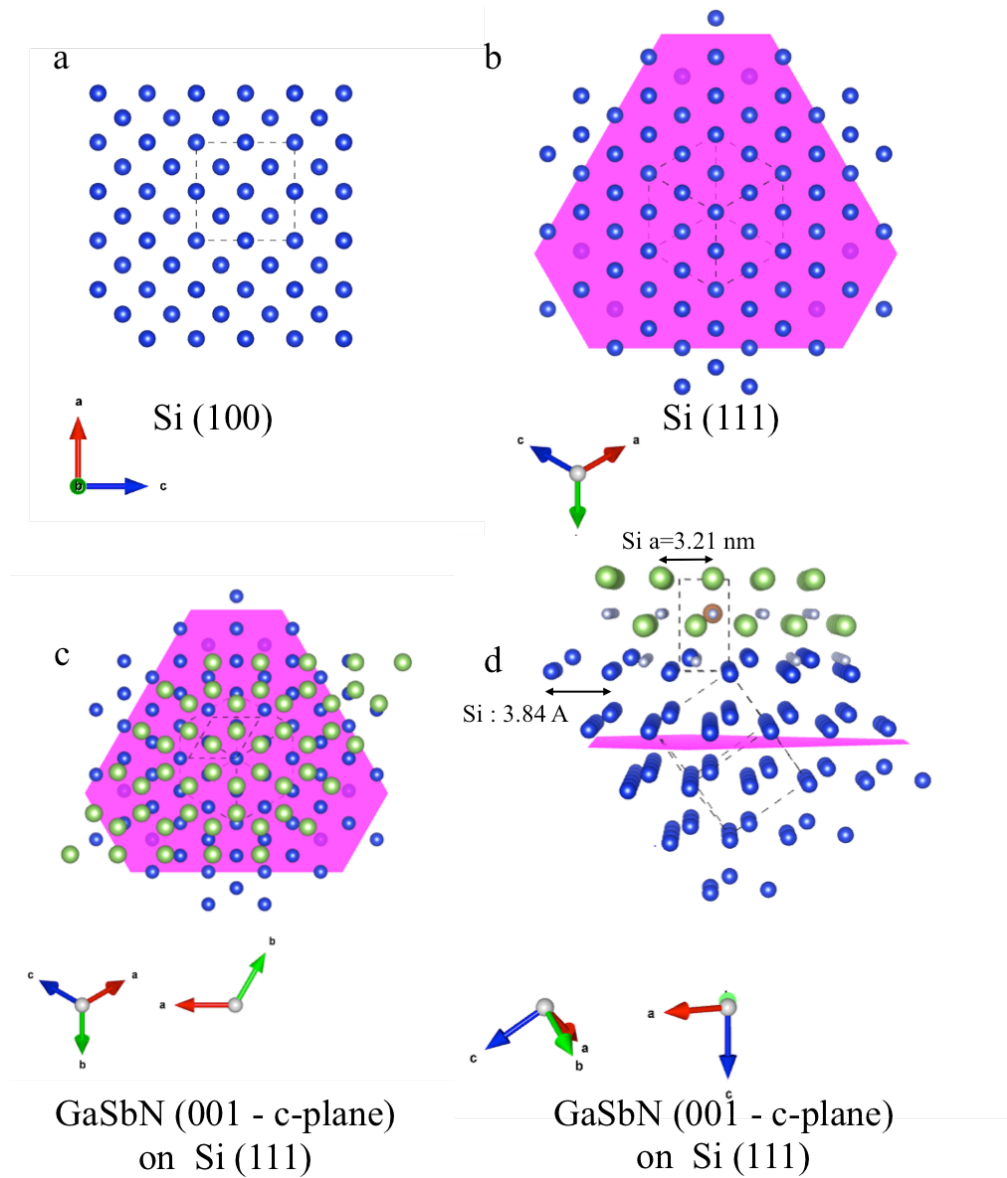


Figure 5.14 Silicon crystal, a) (100) plane, b) Si (111) plane, c-d) epitaxial relationship between c-GaSb_xN_{1-x} and (111) Si.

It is interesting to notice the projection of the (111) plane defines a hexagonal lattice of silicon atoms, which appears to be an adequate substrate for heteroepitaxy of a crystal with a wurtzite structure like $\text{GaSb}_x\text{N}_{(1-x)}$ as shown in Figure 5.14c-d.⁹⁹

As it was shown the $\text{GaSb}_x\text{N}_{1-x}$ materials have a larger unit cell than pure GaN, therefore the amount of strain in heteroepitaxial structures of $\text{GaSb}_x\text{N}_{1-x}$ on Si is smaller than in GaN on Si. This observation could have profound implications in the fabrication of thick epitaxial layers to minimize carrier recombination in a photoabsorber, as well as enabling the possibility of fabricating monolithic z-scheme dual semiconductor architectures on an inexpensive substrate as p-type silicon.

A summary of the minimum domain size of the 825°C isothermal series of experiments with increasing GSR is presented below in Figure 5.15.

First it is important to notice that samples grown at GSR's of 1:12 and 1:18 are less than 200nm thick and therefore the estimation of the domain size is most likely representative of the smallest domain in the substrate GaN, not the deposited $\text{GaSb}_x\text{N}_{1-x}$ layers. The films grown on sapphire and silicon have minimum domain sizes of 20 to 80 nm. These correspond to the seed nuclei from where the texturization of the films evolves.

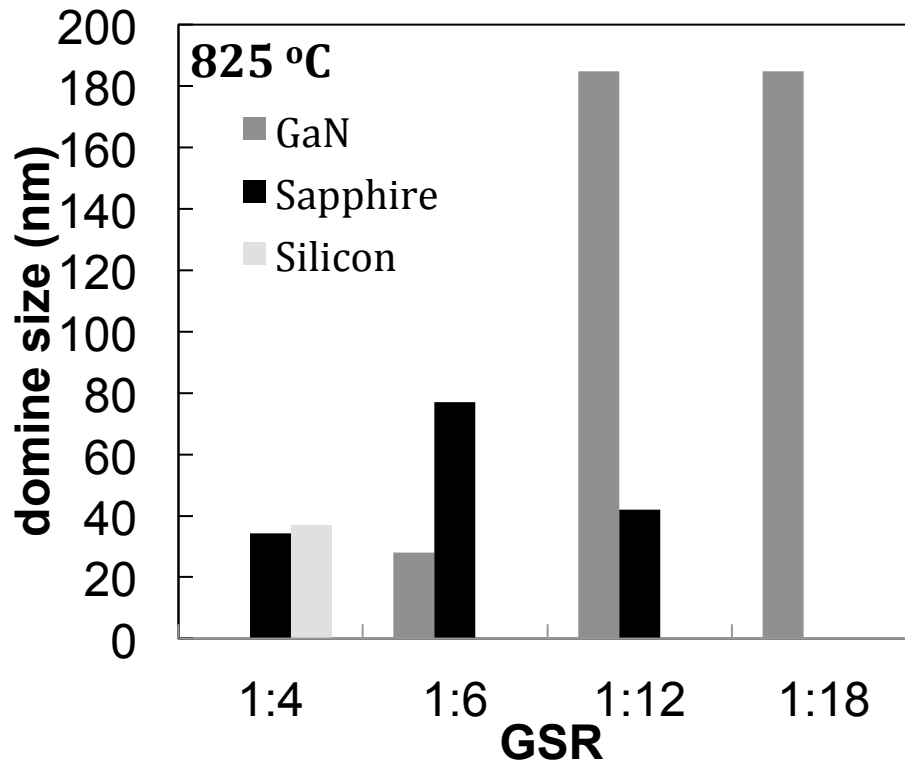


Figure 5.15 Domain size in $\text{GaSb}_x\text{N}_{1-x}$ at increasing levels of GSR.

Samples G and H, grown at low GSR's and a temperature of 850°C, present an almost negligible reduction in the band gap compared to that of pure GaN. The Sb content is below the quantification limit by EDS. The expansion of the lattice parameter in the $\langle 002 \rangle$ direction at 850°C does not directly correlate with the GSR as shown in Figure 5.17 .

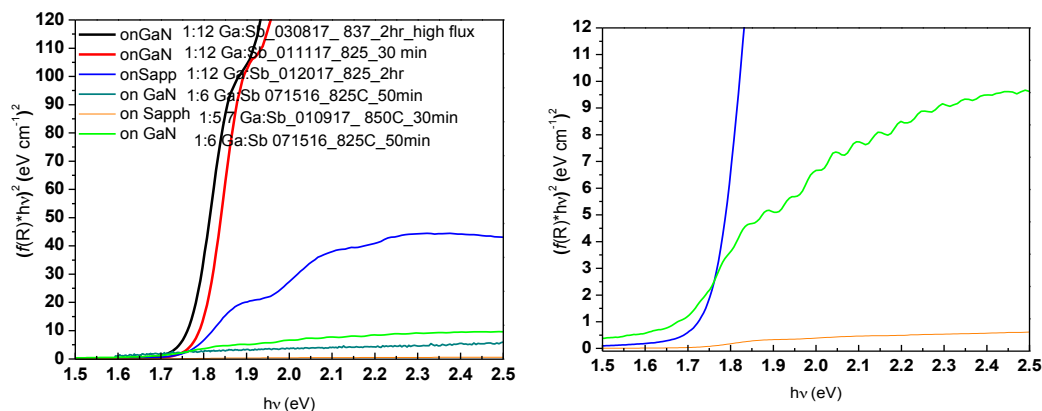


Figure 5.16 UV-vis Tauc plots of samples grown between 825 -850°C

Likewise, it is important to point out from the tauc plot of the uv-vis spectra shown Figure 5.16, that the samples containing higher concentrations of antimony present absorption coefficients in the visible range that are over 1 order of magnitude greater than that of the samples with smaller Sb concentrations.

The x-ray diffraction patterns and cross-sections of the samples grown at a constant SGR of 1:12 at increasing deposition temperatures (D, F, I and J) show how the crystallinity, and epitaxial quality of the films improve as the growth temperature is raised from 825 to 875°C. It is important to note, however, that the sample F (030817) presents re-nucleation on the epitaxial layer. This overgrowth is caused by the high flux of TMGa used (in an attempt to obtain thicker layers for PEC testing).

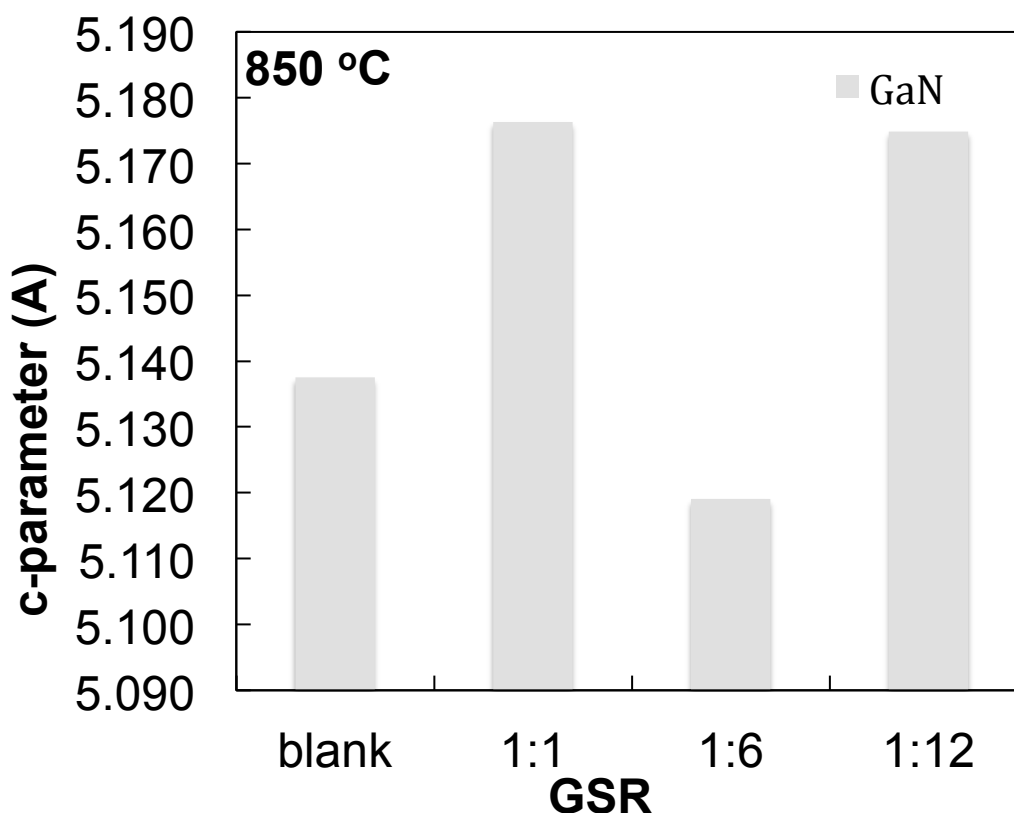


Figure 5.17 C-parameter of samples grown at 850°C at different GSR's.

Samples C and H were also deposited on silicon substrates. The diffraction patterns is shown below in Figure 5.18. The most intense peak on these diffraction patterns is located at 28.44° resulting refraction of the silicon (111) plane.

From the diffraction patterns it is observed that only the (002) planes of GaSbN produce diffraction signals at 34.3° . This represents a shift, with respect to epifilms of GaN, towards smaller angles by 0.3° or about 1000 arcsec. While the two samples grown on silicon have essentially the same lattice parameter of 5.22 Å, only the one grown at lower temperature of 825°C, ie. 012017Si, shows a band gap reduction to 1.7 eV, whereas the sample grown at 850°C presents its absorption edge at 3.2 eV. This observation

suggests that the highly textured or nearly epitaxial films are undergoing a strained growth due to the lattice mismatch between the layer and the substrate.

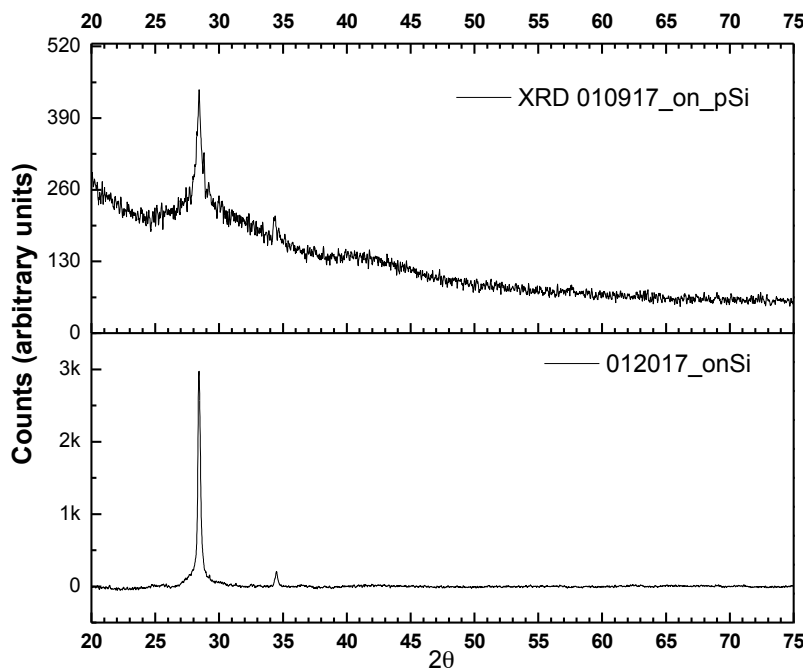


Figure 5.18 XRD diffraction pattern of GaSbN films grown on Silicon wafers

In other words, to accommodate the %strain in the basal lattice parameter, the c -parameter is also expanding even for layers with no band gap reduction, and minimal incorporation of antimony like Sample H (010916Si).

Sample J (032216g and 032216s) were grown at a GSR 1:12 and 875°C . The tauc plot shows the absorption edges for these films in Figure 5.19.

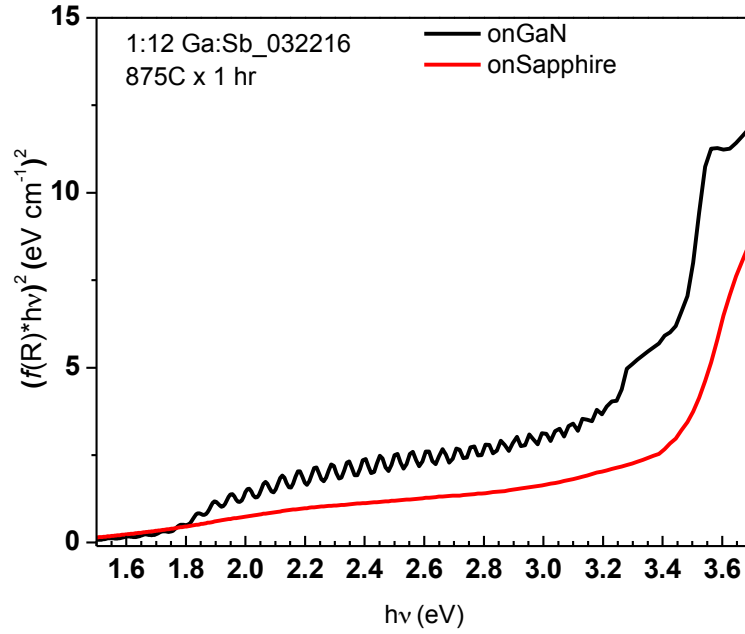


Figure 5.19 Sample J (032216g and 032216s) were grown at a GSR 1:12 and 875°C.

It was observed that, despite the high SGR ratio on that series of experiments, the improvement of the crystalline quality comes at a compromise of the band gap of the semiconductor as shown in Figure 5.19.

A trend line for band gap reduction is observed in Figure 5.20 for samples grown at constant GSR of 1:12 and different substrate temperatures.

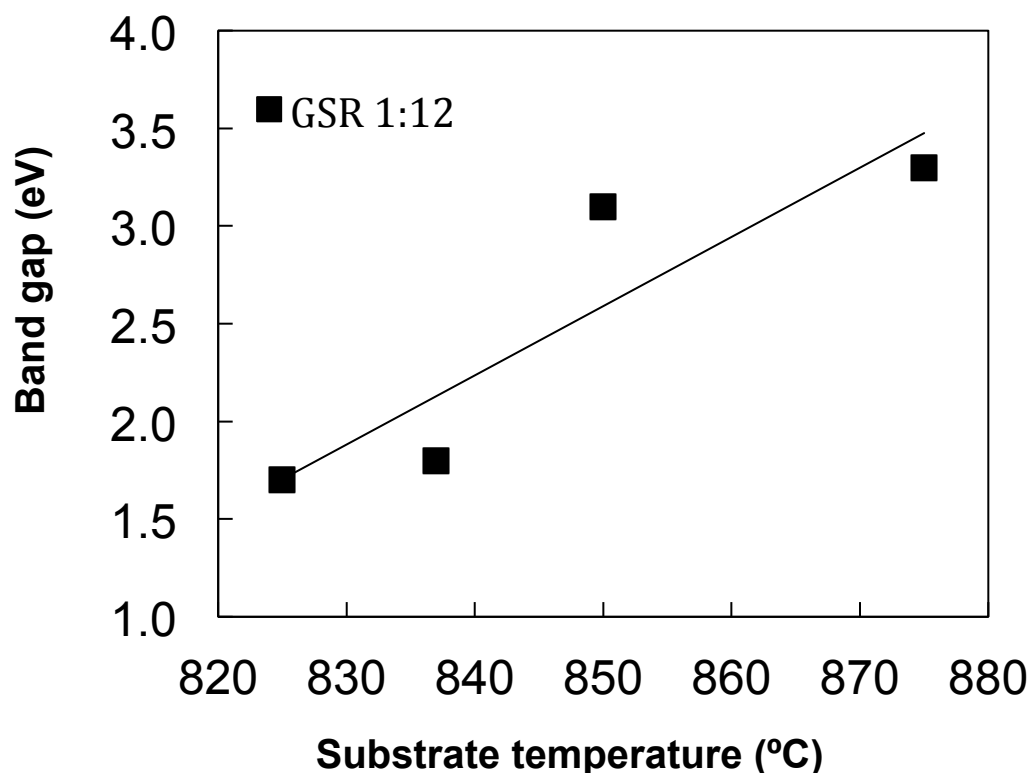


Figure 5.20 Band gap bowing in growth experiments performed at iso-GSR as a function of substrate temperature.

In the highest end of the range of the growth temperatures studied in this work it is possible to observe the best quality single crystalline epitaxial layers. The observed morphology of these samples (Figure 5.21a) grown on GaN suggests a layer-by-layer growth as described by the Frank-van der Merwe model. This mode of growth proves that at high temperature and low flux conditions there is fast diffusion on the crystal terraces, along the step edges and across steps. Given that Sb is not being incorporated during growth at these conditions, as suggested by the wide band gap of these sample grown at elevated temperature, it is noted that the present case is classical homoepitaxy of GaN. The same material was grown simultaneously on Sapphire (Figure 5.21b,d) with cleaning, annealing and buffer steps prior to deposition. The morphology of the cross-

sections evidences the evolution of the semi-sound zone consisting of trapezoidal crystal structures that appear by island growth around nucleation sites forming truncated hexagonal pyramidal mesas with low dislocation density. In heteroepitaxy of GaN this mode of growth is known as the Stranski-Krastanov model, where a combination of layer-by-layer growth is combined with growth of islands.

In general, it is observed that as the GSR is increased the relative amount of Sb in the film increases even for highly crystalline films grown at 837°C. These Sb rich films present absorption edges at higher wavelengths, demonstrating a band gap narrowing up to susceptor temperatures of 837°C. Beyond 850°C increasing the GSR ratio does not seem to have a notable effect in the narrowing of the band gap, and further suggests that there is no alloying with GaSb.

The temperature requirement to incorporate Sb into the lattice of GaN was not the only issue hindering the growth of epitaxial ternary films. The observed band gap bowing in $\text{GaSb}_x\text{N}_{1-x}$ is concomitant with an expansion of the c-lattice constant as shown in prior DFT calculations and peak shifting of the (0002) peak of polycrystalline films of $\text{GaSb}_x\text{N}_{1-x}$. The positive distortion in the lattice caused by Sb, compared to the substrate (GaN and Sapphire) induces further lattice mismatch with the substrate and thereby more strain as the content of Sb in the alloy increases, as it was shown in the strain bar graph.

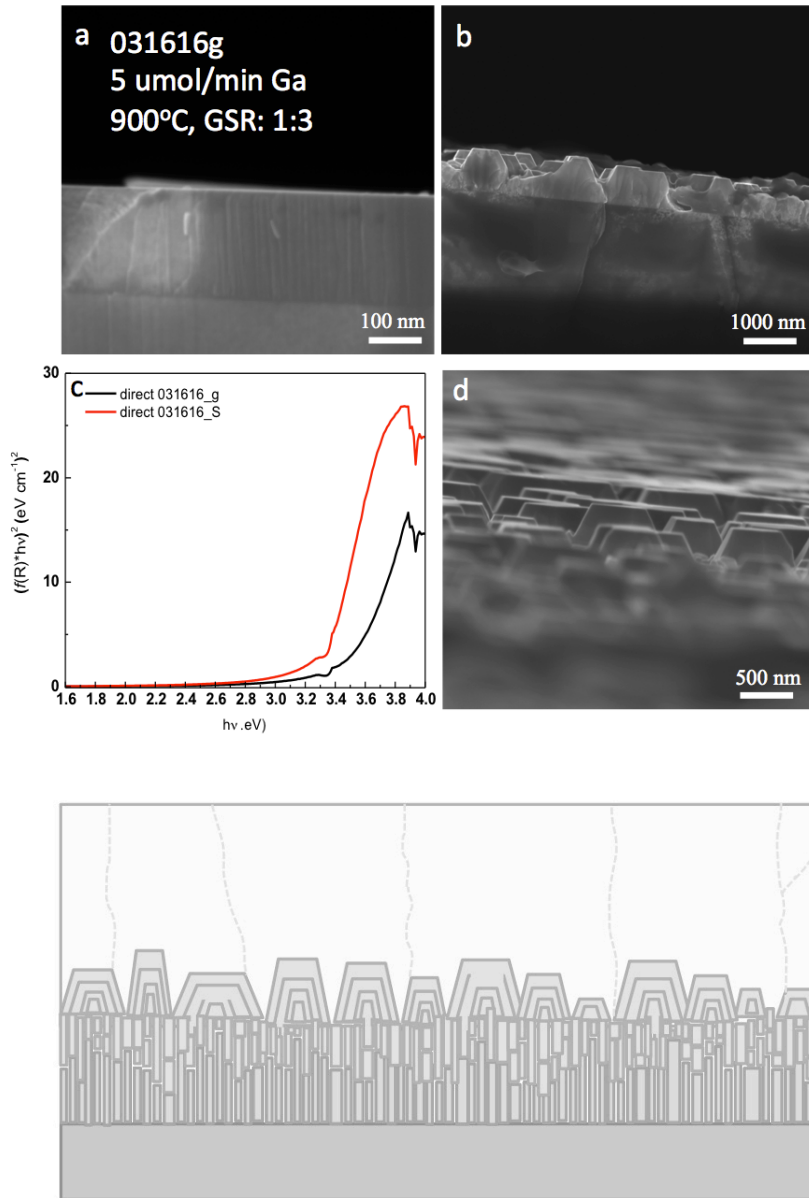


Figure 5.21 Scanning Electron Micrographs of GaN grown on (a) GaN, and (b,d) Sapphire, c) Tauc Plot of uv-vis spectroscopy of GaN in both substrates e) growth mechanism of GaN on Sapphire.^{100,101}

Therefore, the amount of strain that can be accommodated by elastic relaxation is reduced as more antimony incorporates in the films. Consequently, beyond the critical thickness, higher misfit dislocation density results with plastic relaxation at the interface

with increasing Sb concentration. These misfit dislocations result in threading defects that propagate throughout the crystal to release strain.

Table 1 summarizes the relevant experimental results.

Sample	Substrate	2 θ	0b	c-constant	a	E _g	T	GSR	f%	TMGA	FWHM	tau
GaN	wafer	34.65	17.325	5.173	3.182	3.4	1050	1:0	0.00			
010917	onGaN	35.03	17.515	5.119	3.148	3.3	850	1:5.7	-1.06	12.50	0.06	154
071516	on Sapphire	34.5	17.25	5.195	3.195	1.7	825	1:6	8.40	11.00	0.12	77
071516	on GaN	34.66	17.33	5.172	3.181	1.7	825	1:6	-0.03	11.00	0.33	28
011117	on Sapph	34.43	17.215	5.205	3.202	1.8	825	1:12	8.58	5.00	0.22	42
012017	on Si 001	34.38	17.19	5.213	3.206	1.7	825	1:12	-4.17	5.00	0.25	37
012017	on Sapphire	34.59	17.295	5.182	3.187	1.7	825	1:12	8.16	5.00	0.3	31
030817	on GaN	34.63	17.315	5.176	3.184	1.8	837	1:12	0.06	17.50	0.05	185
epiGaN_GaN	onGaN	34.65	17.325	5.173	3.182	3.4	900	1:0	0.00			
010917	onSi	34.32	17.16	5.222	3.212	3.35	850	1:6	-3.99	12.50	0.17	54
083116	on Sapphire	34.56	17.28	5.186	3.190		825	1:4	8.24	18.00	0.27	34
040416	on GaN	34.62	17.31	5.178	3.185		825	1:18	0.08	4.00	0.05	185
032916	onGaN	34.64	17.32	5.175	3.183	3.1	850	1:12	0.03	8.44	0.05	185
032216	on GaN						875	1:12				
031516	on GaN	34.63	17.315	5.176	3.184		850	1:1	0.06	4.00	0.05	185

The preceding results show that in the growth of epi-GaN, first stage of growth happens with high nucleation density at low temperature leading to a thin buffer layer (first 50 nm). On top of this buffer zone, GaN grows with a high dislocation density in a

faulted zone of about 50 nm. At a later stage, trapezoidal crystal structures evolve by island growth around nucleation sites forming truncated hexagonal pyramidal mesas with lower dislocation density (150 nm). These superstructures coalesce by lateral growth forming a semisound-zone. The evolution by this mode of growth is the same as reports by Nakamura et. al for growth of GaN.¹⁰⁰ Finally, nucleation and stabilization happens only at step edge sites where atoms have two nearest and six second nearest neighbor bonds.¹⁰² In this stage, low flux and high temperature are required to promote gallium atom desorption off the crystal terraces, and to drive surface migration to step edge nucleation sites, where ordered incorporation occurs (epitaxy).¹⁰¹ When a second metal, like Sb, is added to the reaction chamber, controlling the relative rates of desorption, migration and incorporation at step edges is further complicated. In fact, the incorporation of Sb into the lattice of GaN has proven to be quite challenging at substrate temperatures that are high enough to promote single crystalline growth during the lateral growth phase. Thus high temperature MOCVD with Sb and Ga metalorganic precursors typically results in pure epitaxial GaN with no Sb incorporation. By contrast, films grown in the low temperature range 650-700°C comprised substitutional Sb atoms but were at best polycrystalline with Sb concentrations up to 8%at.

Here it was determined that in order to deposit thick epitaxial films of GaSbN with adequate band gap for water splitting, it is necessary to feed TMGa at a molar flow rate no higher than $5 \mu\text{mol min}^{-1}$. The growth process is required to have a pre-cleaning step at 900°C for 30 minutes in ammonia to pyrolyze organic contaminants on the substrates. This step should be followed by a thin, low-temperature buffer layer growth for 10 minutes at 500°C. A gallium to antimony mole ratio of 1:12 is recommended for

growth between 825 and 838°C. These conditions will guarantee a band gap of 1.8 eV and a growth rate of about 200 nm hr⁻¹. In order to obtain thick enough films to efficiently absorb 100% of AM 1.5G light it is required to operate the MOCVD reaction at these conditions for about 5 hours, to obtain 1 µm of photoabsorbing layer.

5.3. Vapor-liquid-solid (VLS) growth of GaSbN

In view of the temperature restrictions and the issues with Sb incorporation in epitaxy of GaSbN described in the previous section, as well as the low growth rates that characterize vapor-solid epitaxy by MOCVD, a new VLS method was studied to overcome the aforementioned limitations. The rationale behind this method is that forming a liquid melt of eutectic composition of Cu-Sb, can significantly increase the concentration of Gallium and Antimony to enhance the growth rate, help incorporate more Sb and favor one particular growth orientation. In this study the VLS method is compared with the more conventional vapor-solid MOCVD where the concentration of Sb in the film is controlled by increasing the ratio of Sb to Ga metalorganic precursors that are fed to the reaction chamber.

For this VLS method, thin copper films can be prepared by multiple methods including dropcasting of Cu nanoparticles, followed by melting and microwave plasma reduction, or more conventional methods like thermal evaporation or sputtering on a substrates like GaN, Sapphire or Silicon.

Subsequently, the copper films are placed on the susceptor in the MOCVD reaction chamber the growth is carried out. For this growth experiment the reaction

temperature was 700°C at a GSR of 1:5 and the deposition step took 30 minutes at a pressure of 800 torr.

Figure 5.22 presents the films grown by the VLS method. These deposits grew as highly ordered, single crystalline bundles of GaSbN microrods that appear as pyramidal structures forming a compact film.

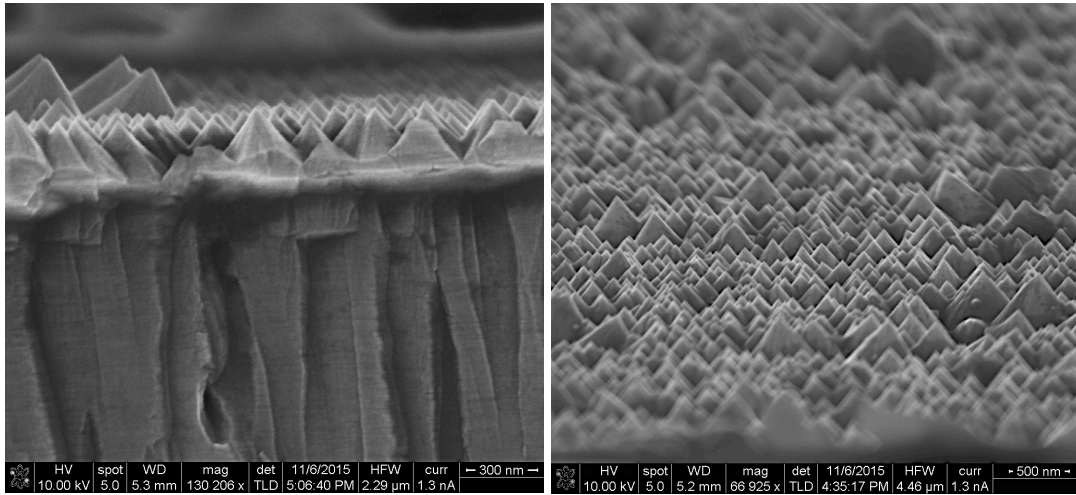


Figure 5.22 SEM of VLS-grown GaSbN a) cross-section b) tilted surface (5% tilt)

In this vapor-liquid-solid method Cu seeds or thin metallic films are used for growth of $\text{GaSb}_x\text{N}_{1-x}$. The use of metals allows for formation of molten alloy films with antimony. As the temperature of the substrate is raised, the solubility of Sb in Cu increases so the level of incorporation of Sb into the GaN lattice can be brought to higher values of around 7%. The film formation begins with dissolution of precursor species into a molten alloy. Once the melt reaches a supersaturated condition, the material precipitates as fused bundles of highly oriented, vertically aligned pillars (Figure 5.22). These pillars grow in the c-direction of h-GaN and form compact films with high Sb incorporation levels. The cross sectional area (Figure 5.23) and surface morphology (Figure 5.22) of

such VLS grown films reveal hexagonal pyramids with semipolar r-plane facets. Compared to conventional MOCVD vapor-solid methods, the approach discussed herein presents important advantages: i) higher and controllable deposition rate, ii) enhanced radial uniformity on wafer surfaces, iii) enabling p-type conductivity by Cu doping. As seen in Figure 5.23, the films present stacking faults seen as dark lines (see red arrows) parallel to the basal c-plane and grain boundaries between each pillar.

The stacking fault density was calculated through computer assisted image analysis by averaging the pixel greyvalue of the area selected the in yellow dotted line in Figure 5.23c, and estimating the number of stacking faults per unit length. The stacking fault density was estimated to be between 500 and 1600 μm^{-1} .

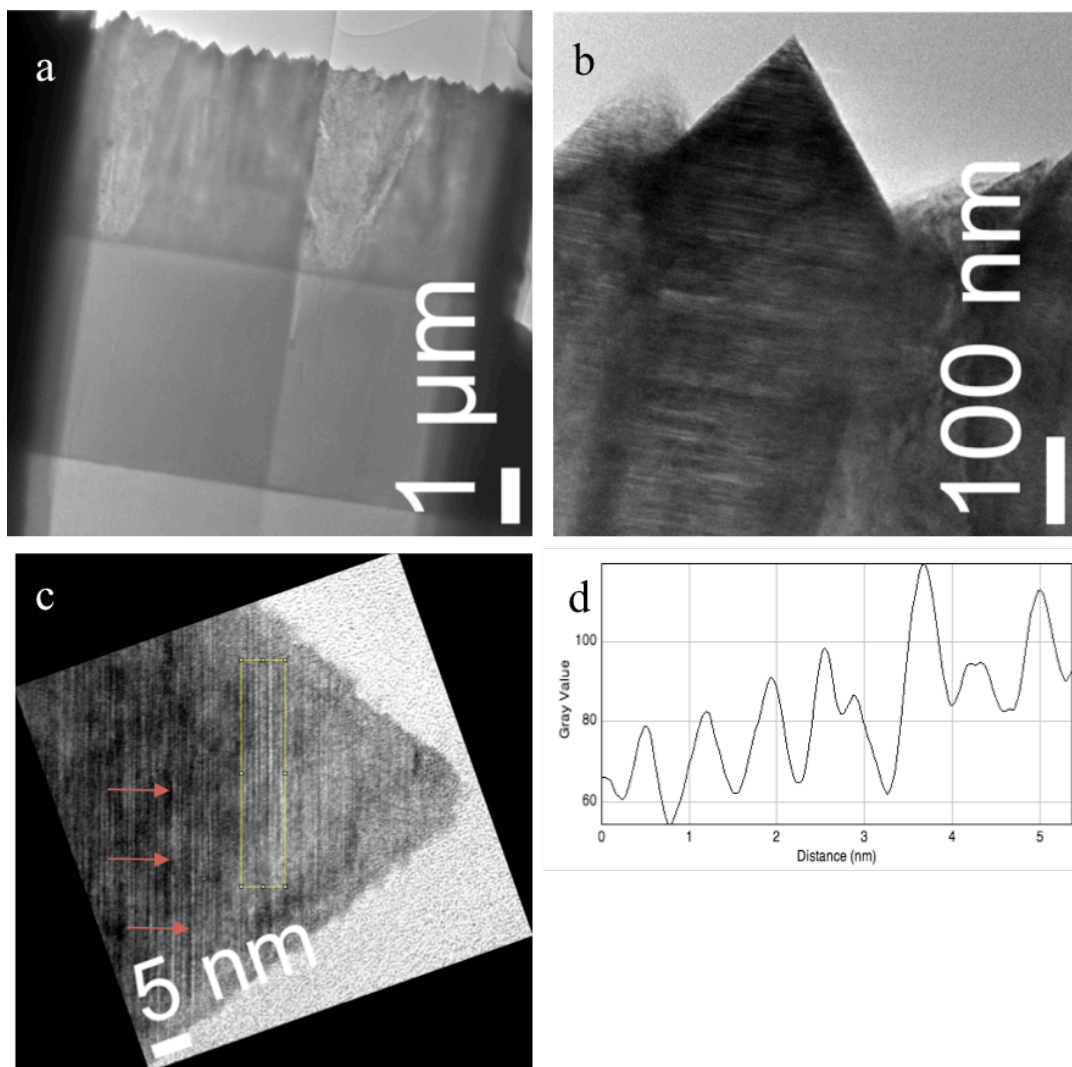


Figure 5.23 a) Brightfield TEM image of VLS grown GaSbN (cross sectional view) , b) Pyramidal facets at the surface (detail 1) c) area for calculation of stacking fault density, d) plot profile of GaSbP showing stacking faults as peaks of high grey value.

5.4. PEC Characterization

The photoelectrochemical properties of epitaxial $\text{GaSb}_x\text{N}_{1-x}$ films with a band gap of 1.8 eV were characterized to assess their ability to split water. First, compared to the

textured films, the open circuit potential of the epitaxial layers appears more stable and does not drift in time as much.

Figure 5.24, shows the open circuit potential under 4 sun illumination of an undoped GaSbN electrode at pH 0. The OCP in the dark is stable at about 0.4 V vs. RHE. When the sample is illuminated the potential rapidly shifts in the negative direction about 100 mV, defining the flat band potential condition for this photoanode.

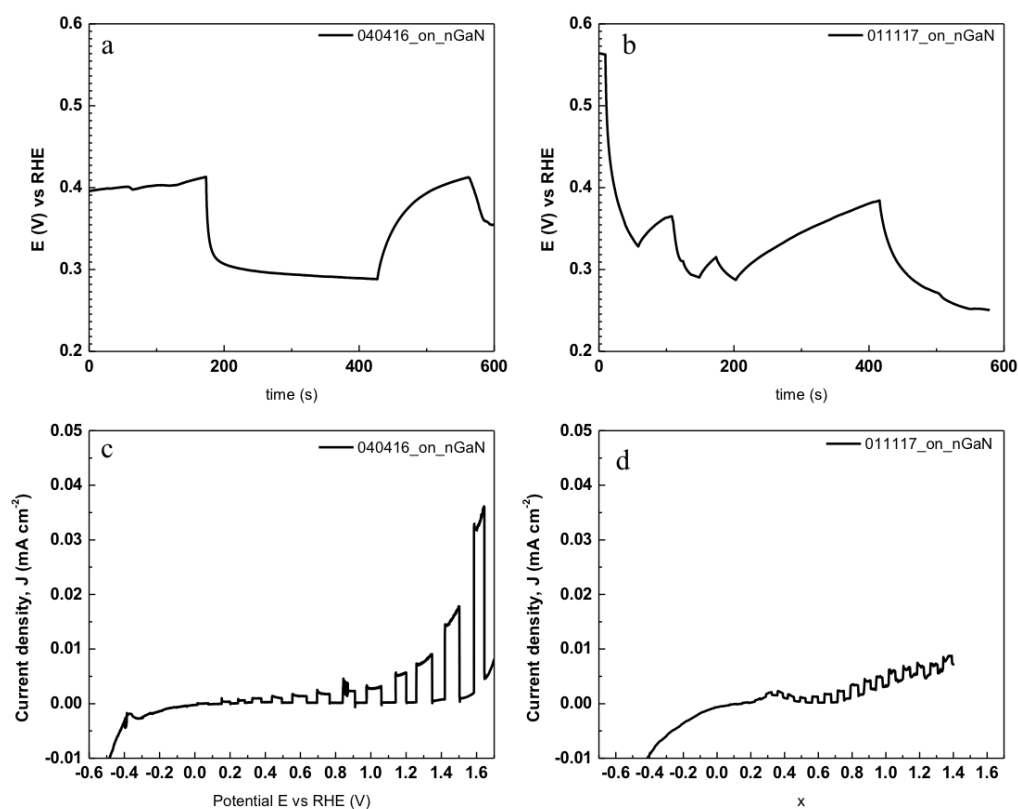


Figure 5.24 OCP and chopped J-V curves for a,c) undoped GaSbN 040416, b,d) Si-doped GaSbN 011117.

The bands in this photoelectrode bend back to their initial condition more gradually when the light is turned off. The accumulation of minority carriers at the semiconductor-liquid junction can be estimated as a function of the OCP from the

potential decay from a state of steady illumination. The defect density at the surface is correlated to the decay rate of the potential. The open circuit potential was normalized according to the following expression:

$$OCP^*(t) = \frac{E - E_{ill}}{E_{dark} - E_{ill}}$$

The transient decay profile of normalized OCP, ϑ , vs t , was fitted to a first order kinetic model to calculate a recombination rate constant:

$$OCP^*(t) = Ae^{-k_r t}$$

To fit this experimental data, this expression is linearized as follows:

$$\ln(OCP^*) = \ln(A) - k_r t$$

The linearized data is plotted in a semi-log plot as shown in inset of Figure 5.25.

Two linear regions are observed, the first one happens rapidly at the beginning when the light is turned off and after about 70 second the potential drop has a different characteristic decay constant.

These two decay regions were fitted to linear expressions thus obtaining the pre-exponential factor, A , and the exponential rate constant, k_r for each.

$$OCP^*(t) = -0.361 e^{(-0.1179t)}$$

$$OCP^*(t) = -1.6245 e^{(-0.004t)}$$

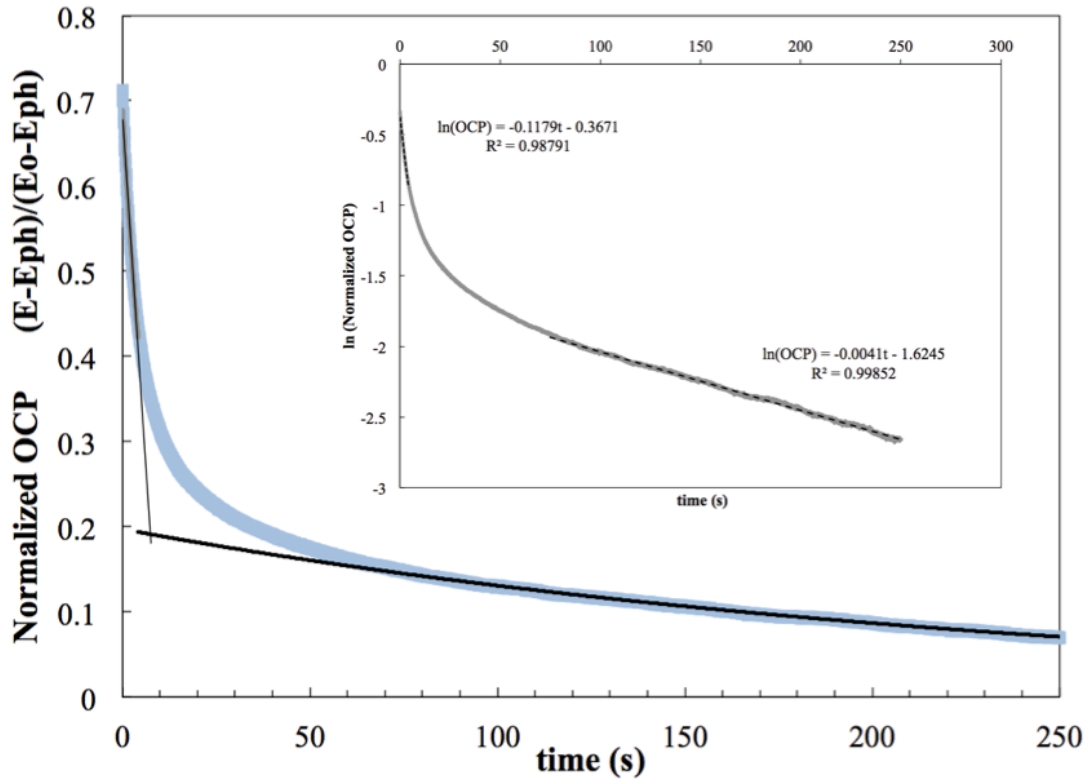


Figure 5.25 Normalized OCP for nearly epitaxial GaSbN film showing the potential decay when illumination is turned off inset (linearized data).

The existence of two distinct characteristic decay constants suggest that there are two different recombination processes with different recombination rates occurring after the optical generation suddenly becomes zero when the shutter blocks the light.

Direct band-to-band bulk recombination happens in a much faster time scale in the order of 10 to 40 of nanoseconds.¹⁰³ Thus, the recombination lifetimes $\tau = k_r^{-1}$ correspond to either surface recombination due to defects or depletion region recombination.¹⁰⁴

The low photovoltage under intense illumination was consistently observed in all samples studied, and in most cases would not exceed 30 mV. Such a behavior indicates

that something is preventing the formation of a depletion region at the interface with the electrolyte.

In an illuminated semiconductor the photovoltage is the difference between the hole and the electron quasi-fermi levels. An explanation of the quasi-Fermi is provided below. The *imref*, or quasi-fermi level can be defined in terms of the steady-state concentrations when excess carriers are present as is the case of a semiconductor illuminated with $h\nu > E_g$.¹⁰³

$$n = n_i e^{\frac{nE_F - Ei}{k_b T}}$$

$$nE_F - Ei = k_b T \ln\left(\frac{n}{n_i}\right)$$

$$nE_F = Ei + k_b T \ln\left(\frac{n}{n_i}\right)$$

We know that:

$$n_i = N_C e^{-\frac{(E_c - Ei)}{k_b T}}$$

So substituting into the previous equation:

$$nE_F = Ei + k_b T \ln\left(\frac{n}{N_C e^{-\frac{(E_c - Ei)}{k_b T}}}\right)$$

$$nE_F = Ei + k_b T \left[\ln(n) - \ln\left(N_C e^{-\frac{(E_c - Ei)}{k_b T}}\right) \right]$$

$$nE_F = Ei + k_b T \left[\ln(n) - \ln(N_C) + \frac{(E_c - Ei)}{k_b T} \right]$$

$$nE_F = Ei + k_b T \ln(n) - k_b T \ln(N_C) + E_c - Ei$$

Thus, the free energy available for water splitting is given by the electrochemical potentials of holes and electrons (i.e. their quasi Fermi levels) according to the expressions²⁴.

$${}_nE_F = E_c + k_b T \ln \left(\frac{n}{N_c} \right)$$

$${}_pE_F = E_v + k_b T \ln \left(\frac{p}{N_v} \right)$$

Where n and p are the carrier concentrations and N_c and N_v are the densities of states in each band.

Therefore the maximum photovoltage of an ideal semiconductor is:

$$V_{ph} = {}_nE_F - {}_pE_F$$

$$V_{ph} = E_c + k_b T \ln \left(\frac{n}{N_c} \right) - E_v - k_b T \ln \left(\frac{p}{N_v} \right)$$

$$V_{ph} = E_g + k_b T \left(\ln \left(\frac{n}{N_c} \right) - \ln \left(\frac{p}{N_v} \right) \right)$$

$$V_{ph} = E_g + k_b T \ln \left(\frac{n N_v}{p N_c} \right)$$

The term in parenthesis is a number between zero and 1, so the second term in this equation is always negative, which makes the photovoltage, or the separation between Fermi levels smaller than the band gap.

If we consider the material as an ideal semiconductor (with no surface or interfacial states) and the E_f is at the same energy level as the electrochemical potential for hydrogen evolution, then when the electrode is immersed in the solution there is no

disparity between the phases so no equilibration is required and the bands would not bend. The same ideal semiconductor with a higher donor concentration would present a V_{oc} that is non zero according to the following formula:

$$(V_{oc})_{max} = |V_{fb} - V_{redox}|$$

In order to put that hypothesis to test, $\text{GaSb}_x\text{N}_{1-x}$ samples were prepared while feeding silene (10ppm) in Hydrogen with a molar flow rate of 5 nm min⁻¹ to increase the donor concentration in the material.

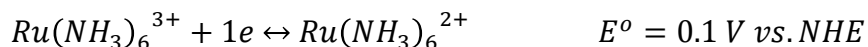
The behavior of a Silicon doped GaSbN electrode, having the same band gap, as the sample mentioned previously, has a more positive dark open circuit potential of 0.56 V vs RHE. Intense illumination also shows n-type conductivity but the magnitude of the photovoltage, between the dark and illuminated conditions, V_{ph} , is almost 300 mV in the first chopping cycle. However, the response to illumination, especially the rate at which the bands return to their initial bent condition in the dark, is much slower than in the un-doped epitaxial samples. In the following chopping cycles, in the dark the potential increases very slowly, defining a maximum photovoltage of 100 mV. The magnitude of photovoltage in the photovoltage after several chopping cycles is essentially the same as in the un-doped electrodes.

While the increase in the photovoltage in the first chopping cycle in the doped samples compared to more weakly n-type GaSbN would suggest that there is not enough disparity between the E_f of the samples not intentionally doped and the redox potential of HER; yet the positive position of the conduction band (below HER in the electrochemical scale) cannot be accounted for in this model, because the premise for that explanation is

that the conduction band lays negative of the HER potential (i.e. above HER in the electrochemical scale).

An alternative way of assessing the semiconductor energy level and determining whether there is a non-ideality in the material (such as surface or interfacial states) consists of studying the photovoltage in a redox couple having a different reduction potential.

When no other redox couple is present in solution, the Fermi level of an n-type semiconductor equilibrates with the electrochemical potential of hydrogen reduction at 0 V vs. RHE. However, if another redox couple present in the solution lays positive of HER, then the equilibration process ensues with such a redox couple especially if it has faster charge transfer kinetics, as is the case of the Ruthenium couple:



The open circuit voltage of textured GaSbN films was measured in a 3-electrode configuration at pH 9 with and without 1mM hexamine ruthenium chloride.

The solutions comprising HARC (III) were buffered with 0.1 M Carbonate / Bicarbonate as supporting electrolyte.

Table 2 summarizes the results of such experiments:

	$2\text{H}^+/\text{H}_2$	$\text{Ru}^{3+}/\text{Ru}^{2+}$
E_{fb} (V vs RHE)	1.1	0.78
Photovoltage	30 mV	40 mV

Interestingly, it was observed that the flat band potentials in these redox couples were different in magnitude, while the photovoltage was practically the same. However we notice again that the flat band position is located positive of the hydrogen evolution reaction, this means that the classical definition of Fermi level pinning (shown below in Figure 5.26) does not apply in the present case, because in the graph E_{fb} is negative of the hydrogen evolution reaction.

Fermi level pinning happens in semiconductors that have a *localized* density of states between the E_{vb} and the E_{cb}, when in contact with different electrochemical potentials they give the same out voltage output, and different flat band potentials.

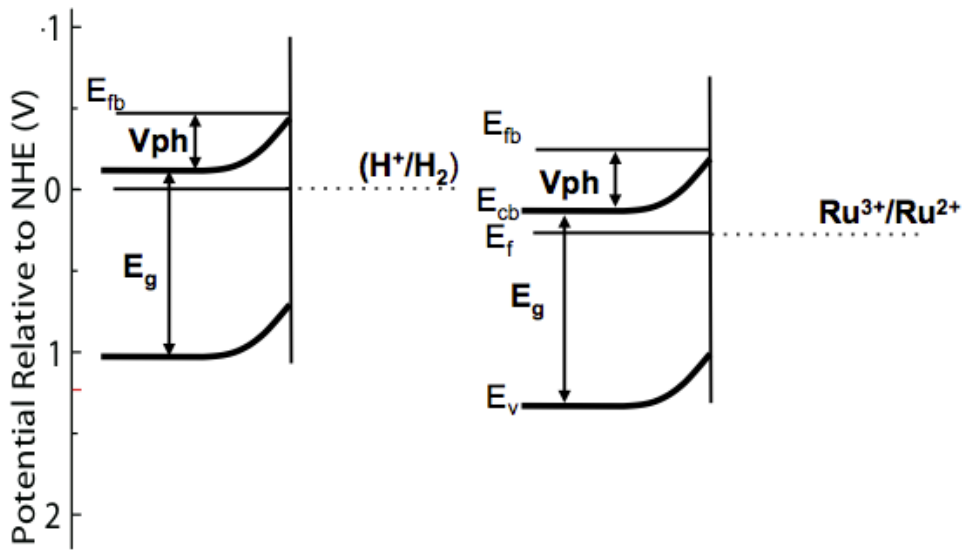


Figure 5.26 Band diagrams of textured $\text{GaSb}_x\text{N}_{(1-x)}$ electrodes in contact with two different redox couples, left) $2\text{H}^+/\text{H}_2$, right) $\text{Ru}^{+3}/\text{Ru}^{+2}$

While it might be tempting to argue that Fermi level pinning due to localized surface states is caused by the polar surfaces of epitaxial or highly textured GaSbN, the model does not adjust to the experimental observation of there being a flat band condition below the redox potential.

A third explanation arises if one considers the possibility of the semiconductor having a *large* number of states between the valence and conduction band. In this case, the charges extend throughout the band gap of the semiconductor resulting in a continuum of states such that the semiconductor behaves more like a metallic electrode thus giving little photovoltage, and no photocurrent. This kind of behavior is common in degenerately doped semiconductors that provide so many charge carriers that the space-charge region inside the semiconductor is not possible.¹⁰⁵ This observed high degree of degeneracy is common in other similar III-V materials like InN as well as in other

photoanodes including Sn:GaAs and W-doped BiVO₄.^{56,106 107} XPS studies of CVD-grown InN reveal that its Fermi level is located 0.91 eV above the conduction band minimum.

The donor concentration of un-doped nearly epitaxial films ($E_g = 1.8$) was estimated by fitting the Mott-Schottky plots to a linear expression, $y = mx + b$ such the slope m of the line represents the factor outside of the brackets in Poisson's equation normalized for the geometric area of the electrode:

$$\frac{1}{C_{sc}^2} = \frac{2}{A^2 N_D e_o \epsilon_s} \left[(V - V_{fb}) - \frac{KT}{e_o} \right]$$

Solving for N_D , one obtains the doping concentration:

$$N_D = \frac{2}{m e_o \epsilon_s A^2}$$

Where A is the geometric area of the electrode in cm^2 , e_o is the charge of the electron at rest, and ϵ_s is the permittivity of the sample.

In the absence of more information, the relative permittivity of pure GaN has used to get a rough estimated of the donor density in $\text{GaSb}_x\text{N}_{(1-x)}$. The donor density was estimated to be around **$1.2 \times 10^{21} \text{ cm}^{-3}$** .

In non-degenerate semiconductors the difference between the Fermi level and the intrinsic level can be estimated using the following expression:

$$n = n_i e^{\frac{E_f - E_i}{kT}}$$

Such a high donor concentration, however, means that the material is very heavily doped n^{++} and therefore its safe to assume that the Fermi level is located within $3KT$ of

the position of the band gap, but the above relationship is not applicable.¹⁰⁸⁻¹¹⁰ The electrochemical behavior of the GaSbN electrodes is consistent with the model of a metallic electrode immersed in an electrolyte solution, where light does not significantly affect the onset potential for oxygen evolution.

In the present case, both unintentionally doped and intentionally doped GaSb_xN_{1-x} epitaxial films have their onset potential for oxygen evolution when the electrodes are reversed bias more than 1.4 vs RHE, which is several hundred millivolts more than the standard oxidation potential for water (due to the OER overpotential).

In the doped GaSb_xN_{1-x} the metallic character of the degenerately doped semiconductor is even more obvious. As the electrode is biased positively the resistive linear behavior is observed to follow ohms law.

For metallic electrodes, the charge accumulated near the solid-liquid junction, as well as the associated potential drop, is concentrated in the first few Angstroms into the material. The high electronic conductivity of the metal does not permit an electric field to be supported. In consequence, when the n⁺⁺ GaSb_xN_(1-x) comes into contact with the solution, most of the potential drop occurs at the Helmholtz layer in the liquid phase. In other words the epitaxial films of GaSb_xN_(1-x) do not show a depletion region due to the high density of states between the valence and conduction bands.

The degenerately doped GaSb_xN_(1-x) can be thought of as semiconductor that has its Fermi level position above the conduction band minimum. This phenomenon is known as the Burstein-Moss shift, in which the apparent band gap of a semiconductor appears increased. In other words, for a degenerate electron distribution all states close to the

conduction band edge are populated. Therefore, a transition from the valence band cannot take place into such states.¹¹¹

Un-intentional doping of GaN and its alloys can result from native defects or foreign elements as impurities. These must be controlled to optimize the device performance, however such unintentional doping in GaN has yet to be understood.

Historically, high concentration of nitrogen vacancies was thought to be responsible for un-intentional n-type doping (with carrier concentrations in excess of 10^{19} cm^{-3}) in the first heteroepitaxial films of GaN developed in the 1960's. The evidence for this explanation was only circumstantial; GaN had to be grown at high nitrogen vapor pressures to stabilize the crystal at elevated temperatures, which made it plausible that nitrogen vacancies were created in GaN grown at lower pressures. The role of nitrogen vacancies acting as shallow donors was re-evaluated and it is now considered unlikely that nitrogen leads to n-type conductivity. In the 1980's, oxygen impurities arising from air leaks and/or moisture in ammonia were identified as a possible dopant causing the n-type conductivity.¹¹² Oxygen doping is now thought of as the main donor impurity that causes un-intentional doping, especially when no special precautions are taken to avoid oxygen resulting from air leaks. In the growth conditions of the present study the leak rate of oxygen is about $17 \mu\text{mol min}^{-1}$ (10^{19} molecules per minute) as discussed in the Chapter 4. For comparison TMGa is fed into the chamber at a rate of $5 \mu\text{mol min}^{-1}$. With this molar flow of oxygen into the chamber, despite the fact that excess ammonia creates a reducing atmosphere, free O incorporating onto nitrogen sites can act as a shallow donor.¹¹³

Carbon will act as a donor in GaN if it is located on gallium sites and as an acceptor in nitrogen sites.

VLS grown films presented p-type conductivity with compensation. The p-type character was observed as a positive potential jump in the open circuit voltage when the samples were illuminated. Compensation was detected in the I-V characteristics at anodic potentials, as small positive photocurrents in the order of microamperes per sq. cm. Negative photocurrents could be also measured when the electrode was biased cathodically and illuminated.

Doping GaN p-type is in fact quite difficult to achieve due the large acceptor ionization energy of about 200 meV resulting from the strong electronegativity of the nitrogen atom and low dielectric constant. The ability to dope GaN p-type with Mg through MOCVD was the main achievement of Amano and Akasakis's research, which resulted in the 2014 Nobel Prize in Physics award.¹¹⁴

While the observed p-type doping could be caused by native defects such as gallium vacancies (V_{Ga}), self-interstitial atoms (Ga_i) and antisite defects (Ga_N), the use of copper in the system as catalyst and presence of copper cations in gallium sites (Cu_{Ga}^{+1}) are almost certainly the source of acceptors.¹¹⁵⁻¹¹⁷

Additionally, in the GaSbN films, transport of holes to the liquid interface (or electrons to the contact) is further hindered by a large stacking fault density of up to $1600 \mu m^{-1}$ in the nearly-epitaxial films, since the light penetration depth of visible photons could be well beyond 1 micron in GaSbN.

CHAPTER 6

GROWTH AND CHARACTERIZATION OF GaSbP FILMS

6.1. Antecedents of Metal Organic Chemical Vapor Deposition of GaSbP

Previous work done in collaboration with Russell^{81,118} was the first realization of ternary alloys of GaP and GaSb. A plasma-assisted reactive vapor transport was implemented and led to synthesis of nanowire mats of GaSbP with non-uniform composition. The halide vapor phase epitaxy method was also studied as a proof-of-concept for preparation of GaSb_xP_{1-x}.

6.2. Reactor revamping

6.2.1. Run/vent operation

Run/vent capability was implemented by adding a bypass line between the bubbler exit line and the pressure control valve. This configuration enables discharging the gases into the gas abatement system, to avoid feeding them through the reaction zones of the reactor at the beginning and end of the deposition, during transient operation of system. That is, at the beginning of the experiment, when the temperature of zones 1 and 2 are being ramped up and towards the end while they cool down. Additionally this new capability permits a sharper compositional control of PCl₃ because the reactant can be discarded until a stable composition is attained in the main run line.

6.2.2. Substrate temperature control

Preliminary experiments with the HVPE system showed that un-reacted materials and by-products of the reaction cooled off while flowing through the last 4 inches of the quartz tube, downstream of the graphite susceptor. This rapid cooling led to the formation of a fine mist or cloud that obstructed the line of sight of the pyrometer controlling the induction heater through a temperature feedback loop. When the cloud becomes too dense, the pyrometer signals the induction heater to increase the power output, which overheated the susceptor. This situation created an offset between the actual temperature at the substrate and the temperature readout. During operation, the heater would have to be shut-off to avoid runaway heating of the system caused by the temperature sensing limitations. This happened within the first 10 minutes of operation when it was observed that the apparent temperature was dropping, while the susceptor became red-hot. In order to avoid this problem, the exit cross of the reactor was provided with a viewport that extends into the reactor through a quartz tube sealed at the opposite end, as shown in diagram x. This assembly will be referred to as a pyroscope.

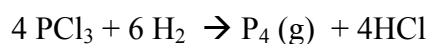
6.2.3. HVPE chemistry

Phosphine gas with formula PH_3 is the most commonly used source of phosphorus for growth of III-V semiconductors. However, due to its extreme toxicity, alternative chemistries have been looked at to provide P to the reaction chamber.

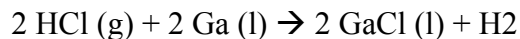
The following reaction sets represents the main chemical processes taking place in the HVPE system.

PCl_3 is used as the source for the group-V element to grow III-V $\text{GaSb}_x\text{P}_{1-x}$. Controlled amounts of this precursor can be fed into the reactor by carrying it with a carrier gas through a bubbler system as the chloride is vaporized at a controlled temperature and pressure.

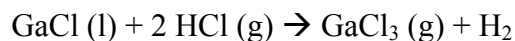
The vaporized PCl_3 and H_2 are un-reactive at room temperature, but once the mix enters into the first zone of the tube furnace the following reaction takes place:



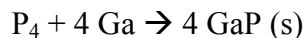
Hydrogen chloride, one of the by-product of the preceding reaction reacts with Gallium from the source boat located in zone 1.



Uptake of more chlorine atoms from HCl produces another halide intermediate, according to :



A parallel reaction competes with the desired product formation reaction. This leads to formation of solid Gallium Phosphide in the gallium source boat, as shown below:



Finally gallium trichloride is transported to the deposition zone where it reacts with P_4 to produce the III-V crystal, according to the reaction:

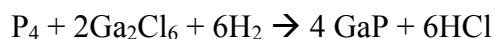
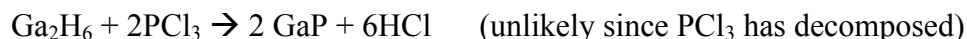
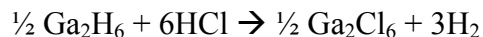
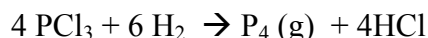


The preceding reaction set describes the chemistry of formation of binary GaP.

For deposition of ternary GaSbP, a similar mechanism involving Sb occurs through the formation of SbCl₃ in the first heating zone of the tube furnace, leading to transport of antimony to the substrate heater where the alloy grows.

Alternative chemistries have been referred to in the literature, involving the formation of intermediate metal hydrides. In this reaction set digallene is formed but the crystal forming reaction is also mediated by uptake of Cl atoms to form gallium hexachloride.

Hydride reaction set



In order to gain better understanding of the reactions that dominate in the growth of III-V alloys by HVPE, the two reaction sets were compared by reducing the amount of H₂ fed to the system, and using inert N₂ as the carrier gas for transporting PCl₃ to the reaction tube.

When small amounts of H₂ are fed, relative to the flux of PCl₃, at close to stoichiometric ratios the growth rate is considerably reduced from 200 um/hr to about 100 nm/hour. This suggests that while the formation of the crystal is in both cases

dominated by chlorine bearing species, a high concentration of digallene, Ga_2H_6 , is required to promote high growth rates.

6.3. $\text{GaSb}_x\text{P}_{1-x}$ characterization

Scanning electron micrographs of highly oriented $\text{GaSb}_x\text{P}_{(1-x)}$ films grown using HVPE are presented in Figure 6.1b and c. The as-grown samples delaminated from silicon substrates yielding thick free-standing films with dimensions of c.a. $150\text{-}200\ \mu\text{m} \times 1\ \text{cm} \times 2\ \text{cm}$. $\text{GaSb}_x\text{P}_{(1-x)}$ samples exhibited crystal sizes between 10-20 micrometers as observed from SEM images (Figure 6.1b and c). Cross sections of the free-standing films were exposed by cleaving the samples and analyzed using Energy Dispersive X-Ray Spectroscopy (EDS) (See Figure 6.2). At the cleaved area of that sample, the Ga:P:Sb atomic ratio ranges between of 47.6:48.5:3.8 and 48.5:49.1:2.3 for multiple deposit replicas. The Sb concentration, as estimated by EDS, ranged from 3% to 10%, for samples grown with the Sb source set at temperatures between 650-750°C, respectively. This observation demonstrates that the temperature of the boat containing metallic Sb is the key parameter for controlling the crystal composition by increasing the vapor pressure of Sb in the precursor zone of the reactor. X-Ray Diffraction (XRD) of $\text{GaSb}_x\text{P}_{(1-x)}$ samples show major peaks similar to GaP, but shifted toward those of GaSb. The absence of a diffraction peak at 25.3 degrees indicates lack of a GaSb phase but formation of a III-V alloy of $\text{GaSb}_{0.03}\text{P}_{0.97}$ with no phase segregation. For the (111) reflection, the observed Bragg angle shifts toward lower angles from 28.3 degrees expected for pure GaP (111) to 29.02 and 29.1; this peak shift can be used for estimating the Sb composition in the

GaSb_xP_(1-x) alloy using Vegard's law. The Sb compositions based on XRD peak shift for various samples were determined to be between $x = 0.03$ and 0.10 (Figure 6.1a).

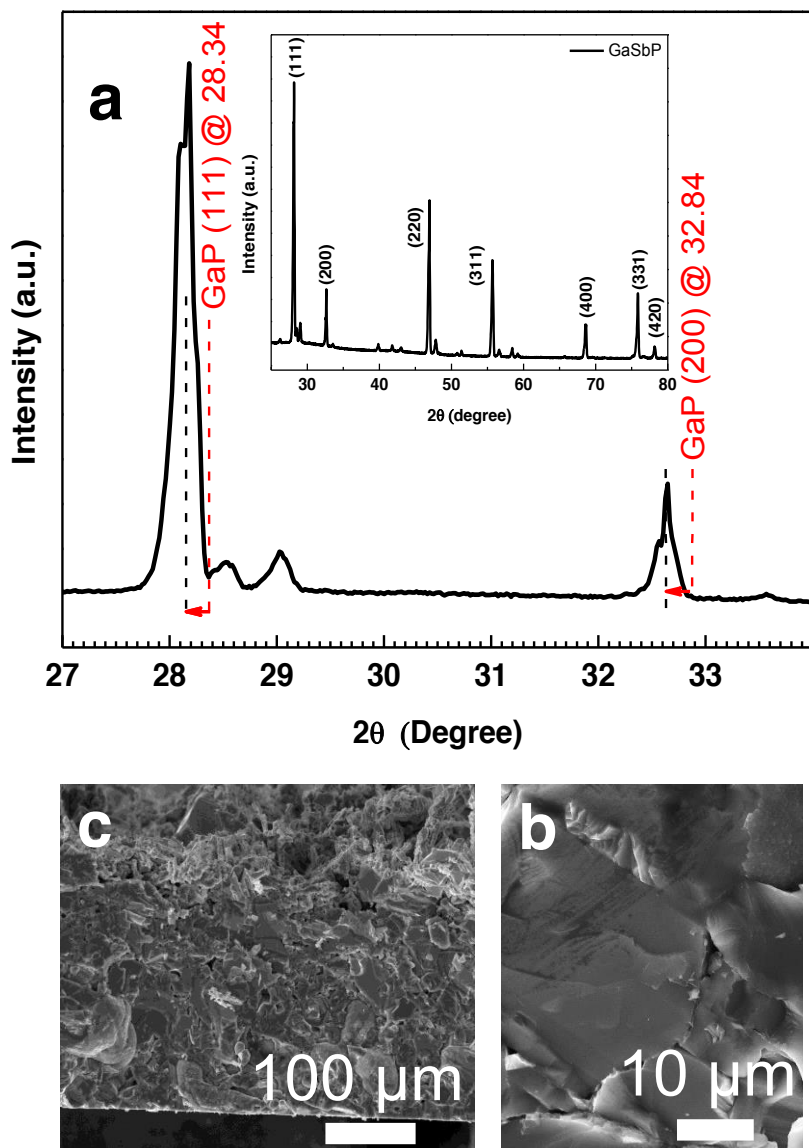


Figure 6.1 HVPE-grown GaSb_{0.03}P_{0.97} free-standing films a) X-ray diffraction pattern for GaSb_xP_(1-x) (GaP [PDF 01-0722146] shown for comparison), b)-c) SEM cross-sectional views

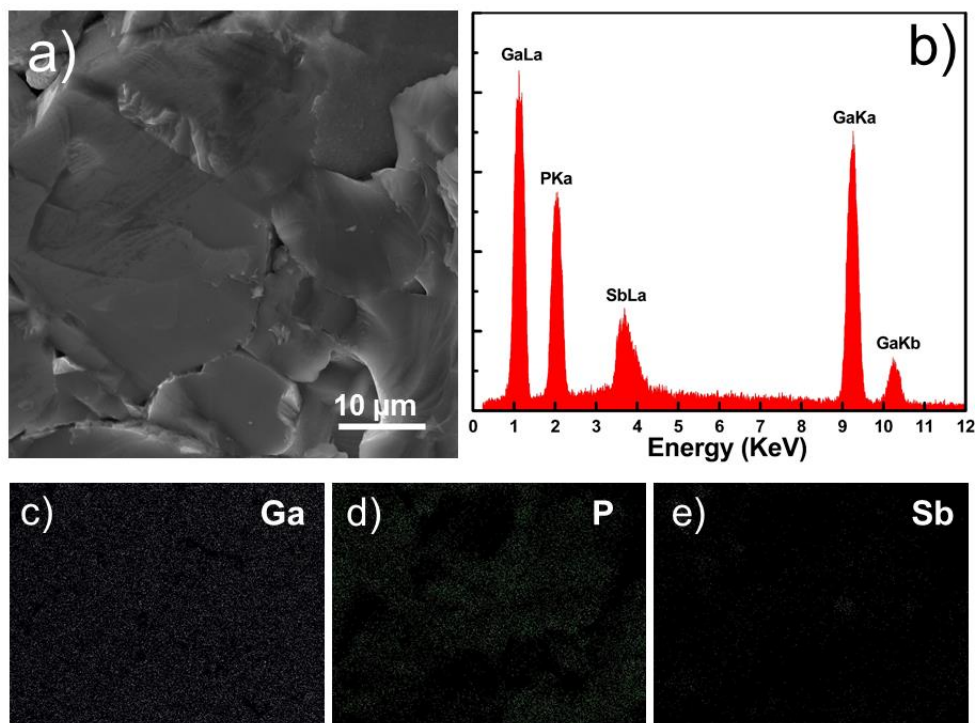


Figure 6.2 a) Cross-sectional scanning electron micrograph of $\text{GaSb}_x\text{P}_{(1-x)}$ film. b) EDX spectrum of selected area c-e) Elemental maps for Ga, P and Sb.

Diffuse reflectance ultraviolet-visible spectroscopy (UV-Vis) measurements for independently grown $\text{GaSb}_x\text{P}_{(1-x)}$ sample replicas were performed to estimate the optical band gap of the material. Tauc plots for the direct allowed transition indicate absorption edges 2.7 eV and an indirect transition at 2.2 eV for samples with 3% Sb as shown in Figure 6.3b. As the Sb content is increased to 10%, an indirect-to-direct absorption cross-over occurs while the fundamental band gap is reduced to 1.6 eV (Figure 6.4c). In order to confirm the direct transitions in the band gap of $\text{GaSb}_x\text{P}_{(1-x)}$, these films were also characterized with micro-photoluminescence spectroscopy using a 442 nm edge laser. The PL spectra of the $\text{GaSb}_{0.03}\text{P}_{0.97}$ films, presented in Figure 6.3c, obtained at 100K exhibits three main peaks centered at 2.22 eV, 2.26 eV, and 2.7 eV.

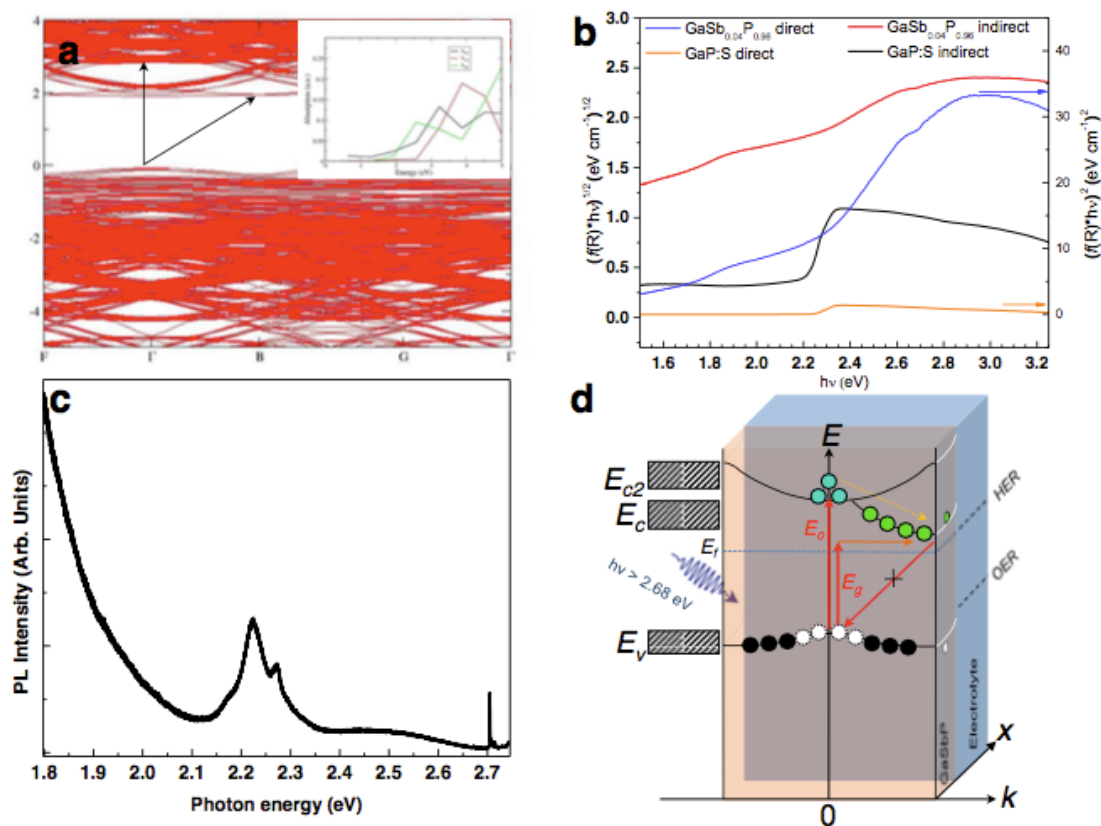
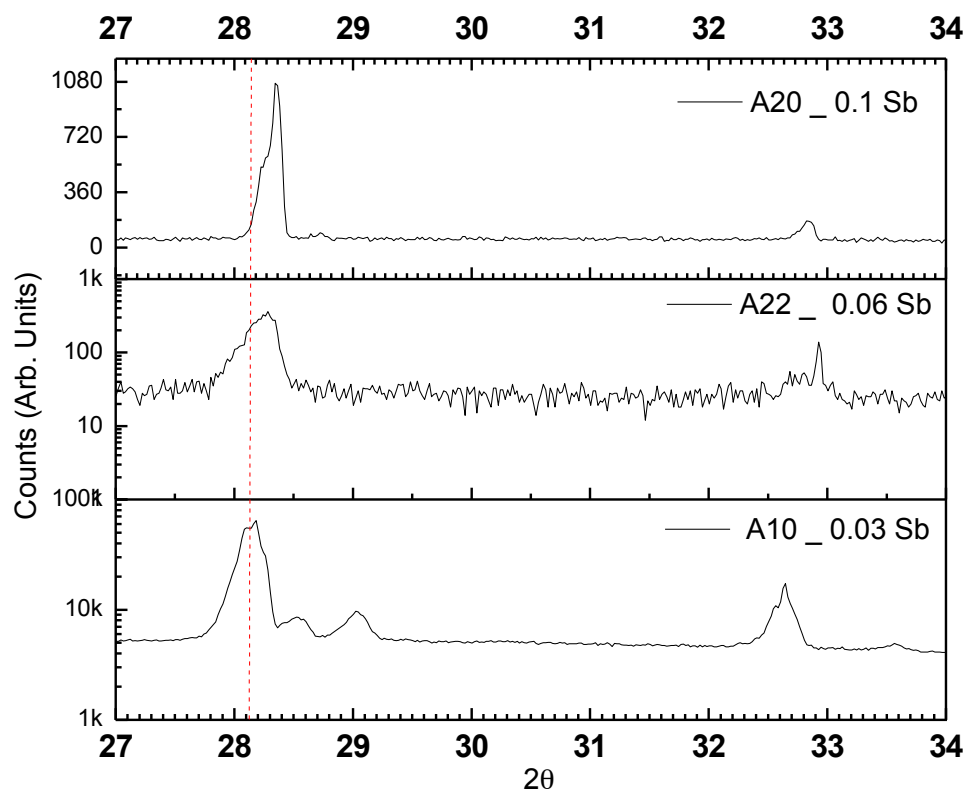
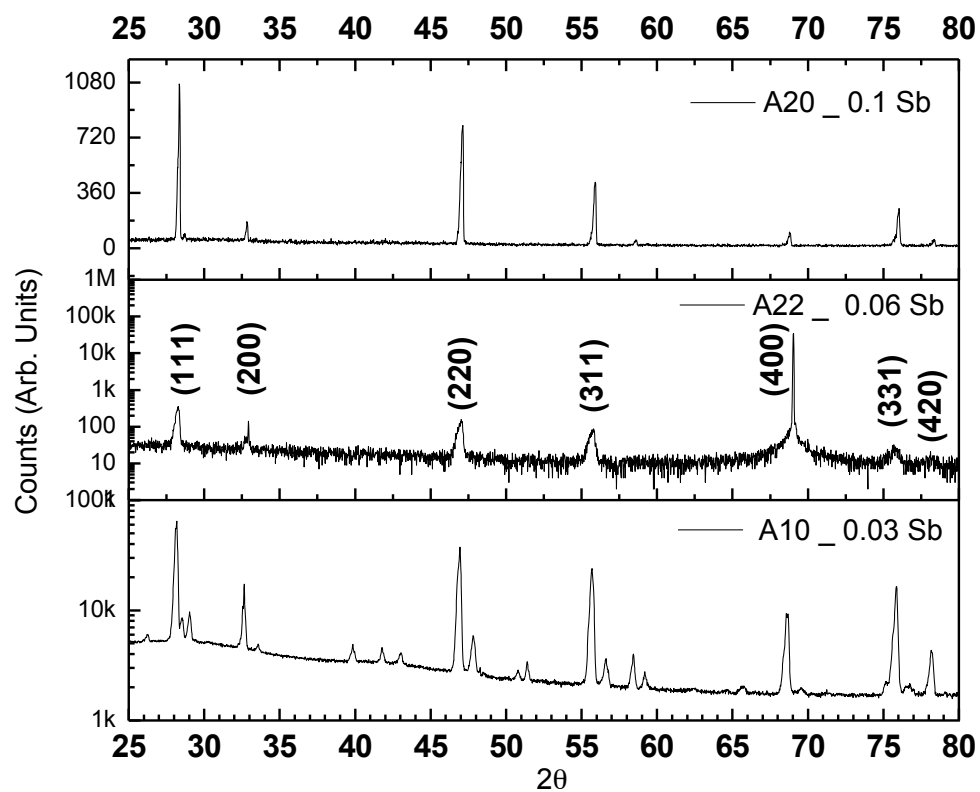


Figure 6.3 **a)** Simulated band structure for $\text{GaSb}_x\text{P}_{(1-x)}$, inset: Simulated Optical absorption spectra for $\text{GaSb}_{0.056}\text{P}_{0.944}$ for the three polarization directions. **b)** Tauc plot of Uv-Vis diffuse reflectance spectra of $\text{GaSb}_x\text{P}_{(1-x)}$ film (blue and red) and n-GaP (orange and black), **c)** PL spectrum (100K) for $\text{GaSb}_x\text{P}_{(1-x)}$, **d)** E-k-x diagram showing carrier excitation process, and injection to electrolyte.



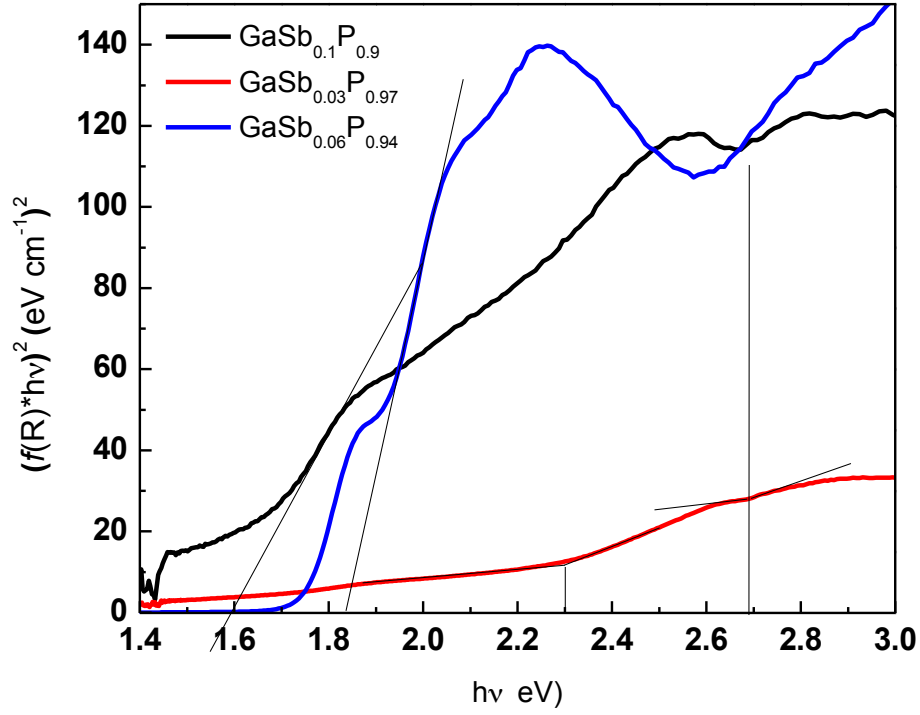


Figure 6.4 a) XRD of GaSbP grown increasing Sb vapor pressures b) detail of refraction peak (111) c) Tauc plot of Uv-Vis diffuse reflectance spectra of GaSb_{0.1}P_{0.9} films (black) , GaSb_{0.06}P_{0.97} (blue), GaSb_{0.03}P_{0.97} (red).

In Figure 6.3c, the PL signal centered around 2.26 eV corresponds to emission caused by conduction band edge to valence band edge transitions, so it represents the indirect band gap of GaSb_{0.03}P_{0.97}. The sharp emission at 2.7 eV can be interpreted as a direct transition from the valence band to an energy state above the conduction band, referred hereinafter as the energy separation E_o of GaSb_{0.03}P_{0.97}.

UV-vis spectra for a commercially available n-doped GaP (University Wafer, 500 μm thick) are also presented in Figure 6.3, for comparison. It is observed that the absorption coefficient of GaSbP films is at least 30 times greater than the absorption coefficient of pure GaP for photon energies higher than the direct transition at 2.7 eV.

Above the indirect transition energy the absorption coefficient is about 3 times larger for the ternary alloy than for pure GaP.

The simulated absorption spectra (Figure 6.3a) for a crystal with composition $\text{GaSb}_{0.03}\text{P}_{0.97}$ is in agreement with the electronic transitions found experimentally. That is, an indirect band gap of 2.26 eV and direct transition E_0 .

Previously, Sb incorporation in the lattice of GaN was shown to cause lattice expansion accompanied by a large band gap bowing and well-suited band edge energetics for water splitting. Such reports are an illustration of prospective computational materials by design where the gap between simulation and synthesizability has been bridged fruitfully.¹¹⁹ In an attempt to alter optical and electrical properties of GaP, antimony alloying has been used to create direct band gap $\text{GaSb}_x\text{P}_{1-x}$ alloys. Recently, we reported a direct band gap transition and the synthesis of p-type Gallium Antimonide Phosphide alloy nanowires having between 1-2 at% antimony (Sb) grown by plasma-assisted reactive vapor transport. Preliminary photoelectrochemical characterization suggested that this material was active as a photocathode producing photocurrents of $40 \mu\text{A cm}^{-2}$.⁸¹

6.4. Photoelectrochemical characteristics

Select $\text{GaSb}_x\text{P}_{(1-x)}$ samples with an antimony concentration between 3-10 at% were made into electrodes (surface area 0.25 cm^2). The flat band potentials of the electrodes were determined using the data from open circuit potential (OCP) measurements under chopped illumination at 10 suns, and compared with the flat band potential obtained by Mott-Schottky and photocurrent onset measurements. The OCP was

measured in a 3-electrode setup with a platinum counter electrode and Ag/AgCl reference electrode in 1M sulfuric acid. Figure 6.6a shows a chronopotentiometry plot of a typical $\text{GaSb}_{0.03}\text{P}_{0.97}$ electrode. In the dark, the open circuit potential of the working electrode is around 0.23 V vs. RHE. When the electrode surface is subjected to 10 sun illumination the OCP shifts negatively 780 mV to a potential of -0.55 V vs RHE, regardless of the Sb concentration in the deposit beyond 3% Sb. Such a response to illumination is attributed to n-type conductivity caused by extrinsic silicon doping in Gallium sites of $\text{GaSb}_x\text{P}_{(1-x)}$, as determined by secondary ion-mass spectrometry (SIMS). The silicon and antimony depth profiles are shown in Figure 6.5.

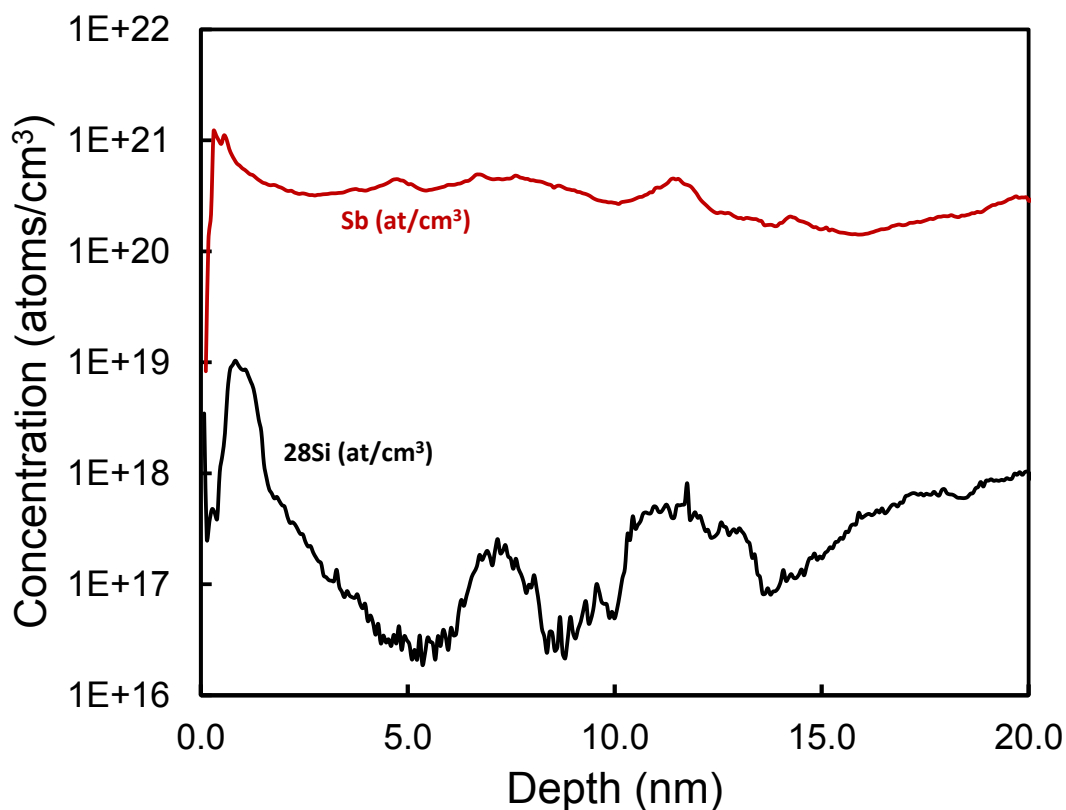


Figure 6.5 Secondary ion-mass spectrometry (SIMS) depth profile of silicon and antimony in a $\text{GaSb}_{0.03}\text{P}_{0.97}$ film.

These results indicate silicon doping of about 40 ppm and validate the Sb concentration between 3-4% for a sample grown with the Sb source at a temperature of 750°C. Substitutional silicon impurities occupying Ga sites, Si_{Ga} , are shallow donors (85 meV below the CBE) that add allowed states close to the conduction band, giving rise to the observed n-type conductivity. Etching of silicon from the quartz tube by gaseous HCl at elevated temperatures in HVPE tools is known to cause the presence of silicon at dopant levels.

Figure 6.6c shows a Mott-Schottky plot for a $\text{GaSb}_{0.03}\text{P}_{0.97}$ electrode. Extrapolating the slope of the linear region of the curve to zero C^{-2} , the flat band potential is estimated to be -0.7 V vs. RHE and from the slope, the donor concentration is approximately $8.6 \times 10^{19} \text{ cm}^{-3}$. While E_{fb} values obtained from the OCP change and MS plot extrapolation are comparable, the observed potential difference of about 150 mV may be attributed to the high charge carrier density and Helmholtz layer capacitance, or a potential barrier in the metal-semiconductor junction caused by the work function of the In-Ga eutectic contact layer. The alloys with higher Sb content, such as $\text{GaSb}_{0.1}\text{P}_{0.9}$, present the same conduction band edge position, however due to their smaller band gap of 1.6 eV, the valence band edge maximum is located negative of the oxygen evolution potential, i.e. above HER, and therefore such Sb-rich alloys are not expected to be able to do un-assisted water splitting because the band edges are not straddling the redox potentials, let alone the kinetic overpotentials associated with the water splitting half reactions.

Figure 6.6b shows the current-voltage characteristics of a $\text{GaSb}_{0.03}\text{P}_{0.97}$ photoanode under 10 sun illumination. From the first chopping spikes, it is readily observed that the onset potential of anodic photocurrent happens at around -0.6 V vs RHE. When the working electrode is biased negative of that potential, large cathodic currents appear due to the position of the conduction band being higher than the HER electrochemical potential, where accumulation ensues with the bands bend downward under forward bias. In this condition, electron flow from the $\text{GaSb}_{0.03}\text{P}_{0.97}$ electrode to the electrolyte becomes thermodynamically possible.

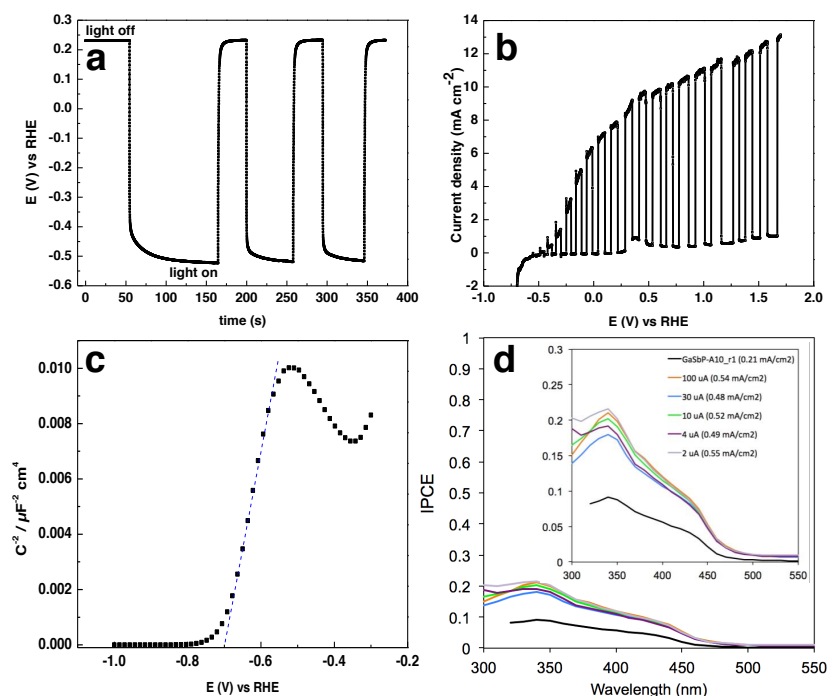


Figure 6.6 Photoelectrochemical characterization of $\text{GaSb}_{0.03}\text{P}_{0.97}$ photoanode a) Chronopotentiometry under 10 sun chopped illumination, b) Linear sweep voltammogram under chopped illumination (10 suns) c) Mott-Schottky plot (100 Hz) in the dark d) Spectral response

As the potential of the working $\text{GaSb}_{0.03}\text{P}_{0.97}$ electrodes is swept positively towards reverse bias, the photocurrent density grows anodically, and under illumination reaches about 7.5 mA/cm^2 at 0 V vs. RHE at 10 sun illumination. This photoresponse keeps growing until around 1 V vs. RHE where there the photocurrent plateaus at around 10 mA/cm^2 in the mass transfer limited regime (or photon-flux limited regime). Aqueous solutions of 1M H_2SO_4 were subjected to light-driven un-biased photoelectrolysis in a two-electrode electrochemical cell with a $\text{GaSb}_x\text{P}_{(1-x)}$ photoanode and a platinum counterelectrode. Gas bubbles were observed evolving and rapidly dislodging from the surface of both electrodes under concentrated illumination (10 suns) and zero-bias when the solution was stirred vigorously. The rate of oxygen production was assessed by measuring the oxygen concentration profile in-situ with an oxygen fluorescent probe (NeoFox, OceanOptics). The solar-to-hydrogen (STH) efficiency for $\text{GaSb}_{0.03}\text{P}_{0.97}$ was determined to be around 1.6% at 1 sun illumination and appears to increase at higher illumination suggesting enhanced efficiency at high-level injection conditions as shown in Figure 6.8. No co-catalysts were used on the photoanodes for these determinations. Interestingly, the theoretical STH of 2.26 eV semiconductor only considering the thermodynamic limits of water splitting is 12%. For a 2.68 eV semiconductor the maximum theoretic efficiency limit is 5%.¹³

Transient current spikes are prominent in each chopping cycle below 0 V vs RHE and gradually disappear as the potential of the working photoanode becomes larger (Figure 6.6b). This transition in the chopping profile from spiky to rectangular must indicate that beyond certain potential there is no hole accumulation at the solid-liquid interface.

The J-V characteristics of a $\text{GaSb}_{0.03}\text{P}_{0.97}$ electrode in the dark show an anodic wave with $E_p = 0.4 \text{ V vs RHE}$ (See Figure 6.6b). This oxidation/corrosion peak disappears in $\text{GaSb}_x\text{P}_{(1-x)}$ samples with Ir as a OER co-catalyst suggesting that hole accumulation at the solid-electrolyte interface might cause photocorrosion of the anode to some extent. A preliminary evaluation of the stability of the photoanode was performed through chronoamperometry showing constant photocurrent in the time scale of the experiment while simultaneously producing oxygen (Figure 6.8a & c). A more in-depth analysis of the stability in different pH conditions is advisable but beyond the scope of the present study.

The spectral response of the photoanode with 3% Sb, obtained at zero bias and one sun illumination, is presented in Figure 6.6d. The external quantum efficiency peaks at around 350 nm, with a narrow efficiency band up to 500 nm, and an integrated current of 0.5 mA/cm^2 . To corroborate these results, the J-V characteristics of a photoanode have been obtained using long pass filters for 400, 550, 610 nm edges. The total power output of filtered light has been adjusted to 1 sun in each case. Figure 6.9 shows that the photoabsorber has a negligible response to wavelengths greater than 550 nm.

The normalized photocurrent response obtained by PCS in Figure 6.7 clearly shows that the energetic threshold required for photons to produce mobile and extractable holes is around 2.68 eV for $\text{GaSb}_{0.03}\text{P}_{0.97}$. The linear regions of the normalized photocurrent plot in Figure 6.7b evidences a direct electronic transition. Unlike UV-Vis, the estimation of the electronic transition of the material by PCS includes the efficiency of charge transport to the surface and the efficiency of interfacial charge transfer.

The IPCE, PCS and optical measurements of the band gap of the material indicate that even though photons of 2.26 eV are absorbed in the semiconductor generating electron-hole pairs, yet these low energy excitons recombine before getting separated since no photocurrent at this photon energy can be extracted.

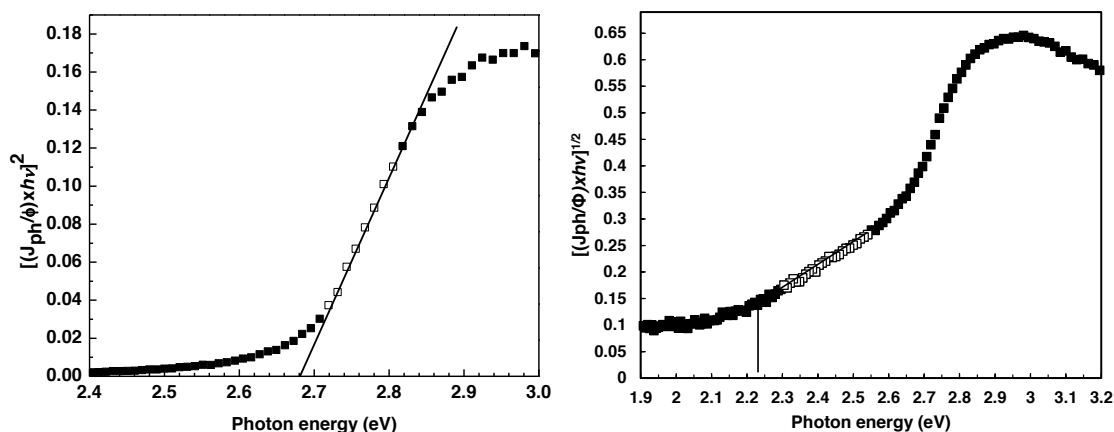


Figure 6.7 Normalized photocurrent response obtained by photocurrent spectroscopy: Tauc plots of a $\text{GaSb}_{0.03}\text{P}_{0.97}$ a) allowed direct transition b) allowed indirect transition.

Additionally, the external quantum efficiency presents a 2-fold improvement when the photoanode is functionalized with an IrO_2 monolayer as shown in Figure 6.10. We have shown that there is optical absorption beyond 550 nm that does not result in carriers sufficiently mobile to be collected as current. By contrast and as mentioned earlier, only more energetic radiation above 2.68 eV is capable of efficiently producing large amounts of photocurrent up to 7 mA/cm^2 at 10 sun illumination (and zero bias) as well as evolving oxygen at the photoanode (see Figure 6.8).

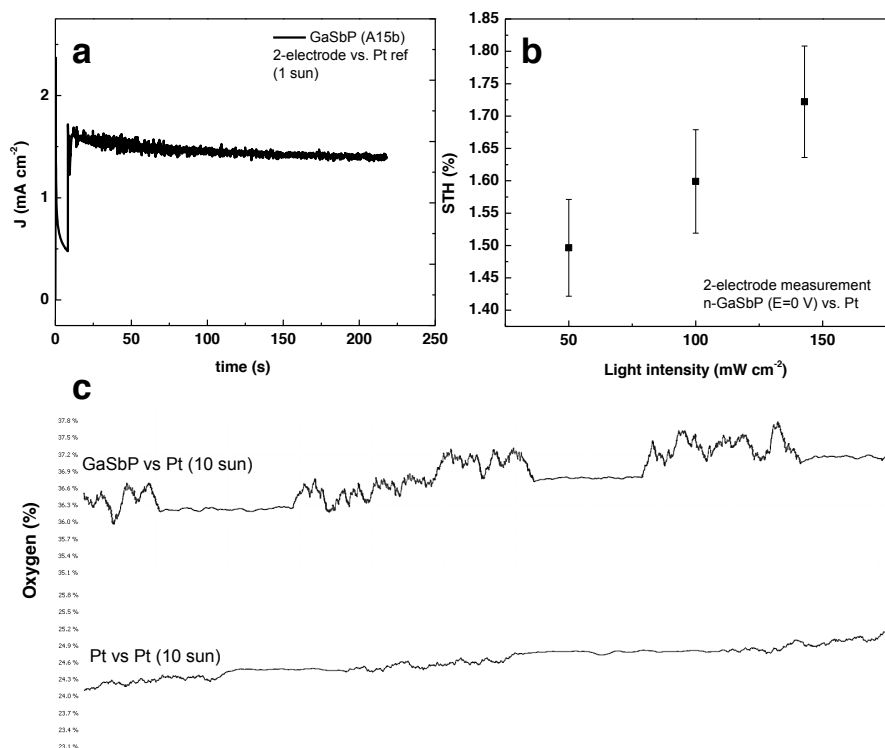


Figure 6.8 a) Chronoamperometry of GaSb_xP_(1-x) photoanode at zero external bias in two electrode configuration. b) STH efficiency of GaSb_{0.03}P_{0.97} at 3 different illumination intensities. c) Optical determination of oxygen concentration profile under chopped illumination. The results of a Pt vs Pt cell control cell are presented for comparison.

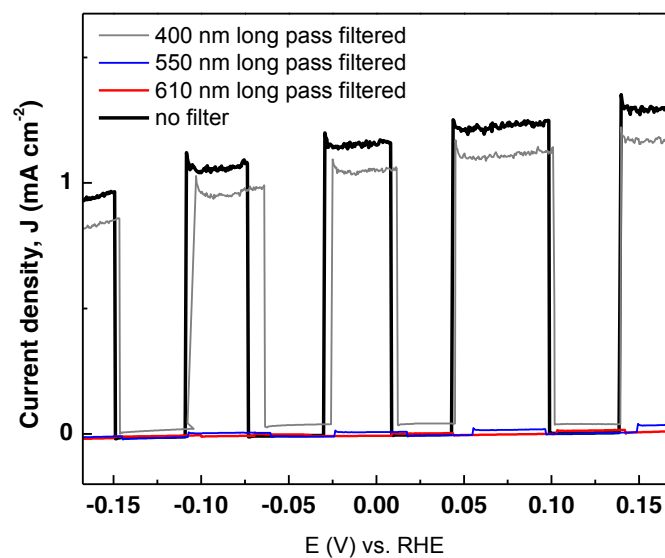


Figure 6.9 Linear sweep voltammograms for $\text{GaSb}_x\text{P}_{(1-x)}$ anode under chopped illumination with long-pass filtered light. Black curve: unfiltered AM 1.5G, Green curve: $\lambda_{\text{cutoff}} = 400$ nm; blue curve: $\lambda_{\text{cutoff}} = 550$ nm; and red curve: $\lambda_{\text{cutoff}} = 610$ nm.

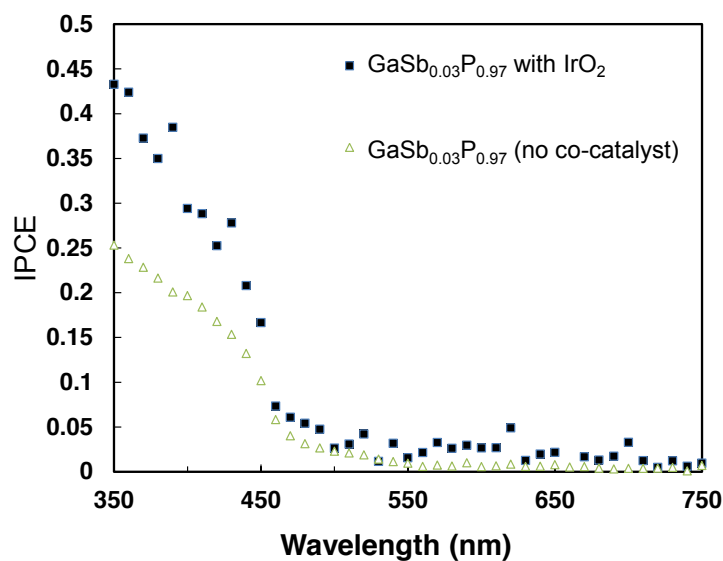


Figure 6.10 Spectral response of $\text{GaSb}_{0.03}\text{P}_{0.97}$ photoanode with and without IrO_2 as OER co-catalyst.

These observations can be interpreted in terms of the absorption coefficient and the light penetration depth of $\text{GaSb}_x\text{P}_{(1-x)}$. As $h\nu - E_g$ becomes more positive, the absorption coefficient grows in magnitude and the penetration depth considerably reduces from about $2\text{ }\mu\text{m}$ at $E_g + 0.2\text{ eV}$, to about $0.08\text{ }\mu\text{m}$ at 2.7 eV in $\text{GaSb}_{0.03}\text{P}_{0.97}$, whereas in pure n-GaP at $E_g + 0.2\text{ eV}$ the absorption depth is about $7\text{ }\mu\text{m}$, and at 2.7 eV reaches $0.8\text{ }\mu\text{m}$ into the material. The absorption depth difference between the two materials becomes more dramatic as the incident radiation becomes more energetic (see Figure 6.11). In materials with short diffusion lengths, the minority carriers generated deep in the bulk of the material cannot reach the solid-electrolyte interface because they recombine.

GaP has an indirect band gap of 2.26 eV and energy separation of 2.78 eV . Thus, in order to generate electron-hole pairs, illumination must be accompanied by a momentum change (phonon absorption). This results in a small absorption coefficient and a large penetration depth. While highly energetic radiation with $h\nu > 2.78\text{ eV}$ could possibly promote electrons to the higher-lying energy states above the conduction band, these electron-hole pairs are created deep into the bulk of the semiconductor, beyond the maximum minority carrier diffusion length. Therefore in GaP, photogenerated electrons in the bulk of the material easily recombine with holes, a phenomenon that has been referred to as back-electron recombination,⁸⁷ thus limiting the amount of carriers available for faradaic reactions at the semiconductor-liquid junction.

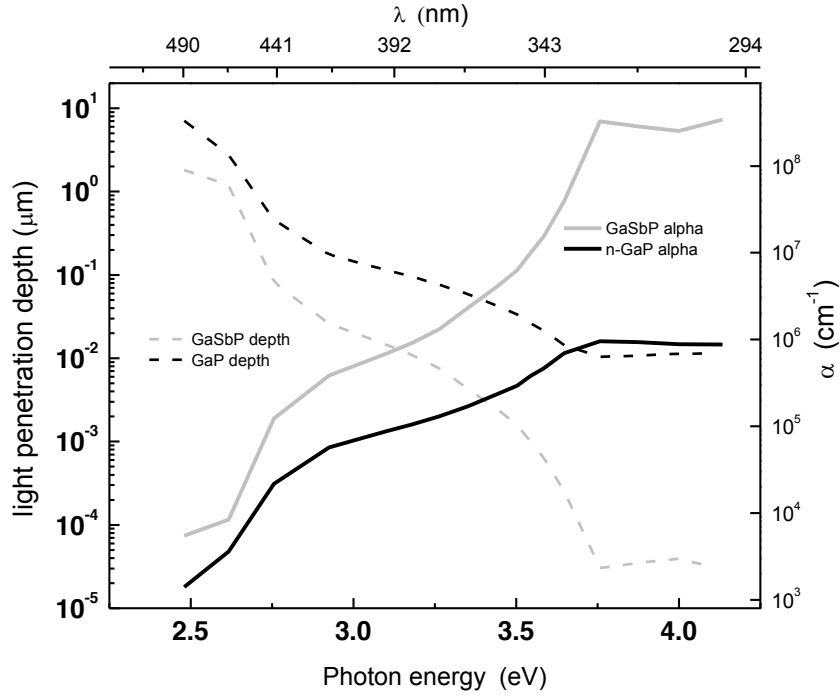


Figure 6.11 Spectral absorption coefficients and the light penetration depths in $\text{GaSb}_{0.03}\text{P}_{0.97}$ and GaP.

In the present case, the incorporation of 3% Sb creates a steep increase in the absorption coefficient within 0.2 eV beyond the fundamental absorption edge. Thus, in $\text{GaSb}_x\text{P}_{(1-x)}$ highly energetic electron-hole pairs are created close to the semiconductor-liquid junction where minority carriers easily drift through the depletion region to the interface while electrons get separated towards the back contact after thermalizing to the conduction band. In ternary alloys with up to 3% Sb incorporation, electrons from the Γ_1 valley thermally relax to the conduction band minimum. Since fast radiative recombination of these electrons with holes in the valence band maximum is forbidden, the thermalization process yields highly mobile carriers in the CBM.

A schematic of the optical excitation, thermalization and transfer of carriers to the solution is presented in Figure 6.3d and Figure 6.12d. These processes result in a 4 fold

improvement in the magnitude of photocurrent density of $\text{GaSb}_{0.03}\text{P}_{0.97}$ compared to GaP at 1 sun illumination and zero bias, as shown in Figure 6.13a. It should be noted that, unlike the behavior of GaSbP, the total magnitude of current density of the n-GaP anode under illumination includes a large component from the background anodic current in the dark, that arises from self-corrosion, since the GaP oxidation potential lays above the oxygen evolution potential.⁴¹ This oxidation process is exacerbated under illumination due to excess minority carriers (holes) which appears as more anodic current but the photo-generated holes obviously cannot participate in the oxidation of water to produce O_2 . The background dark current mentioned above is also apparent in the dark cyclic voltamogram (red curve) shown in Figure 6.12c.

The flat band potential of n-GaP was estimated to be between -0.17 and -0.3 V vs. RHE as determined OCP measurements in the dark and illumination in 1M H_2SO_4 (aq), and corroborated by Mott-Schottky analysis (Figure 6.12a and Figure 6.12b, respectively). Therefore, the valence and conduction bands of GaP should straddle the water splitting potentials, however, these processes are not favored due to the position of the GaP oxidation potential, and possibly also due to the high penetration depth compared to $\text{GaSb}_x\text{P}_{1-x}$.

$\text{GaSb}_{0.03}\text{P}_{0.97}$ and $\text{GaSb}_{0.1}\text{P}_{0.9}$ electrodes were compared by linear sweep voltammetry under chopped illumination, as shown in Figure 6.13b. These photoanodes have equal onset potentials, consistent with the position of the CBE positions in both materials, but the 3%-Sb electrode produces 3 times the amount of photocurrent at zero bias and presents a better fill factor.

The photovoltage obtained in $\text{GaSb}_x\text{P}_{(1-x)}$ electrodes outperforms n-GaP by about one order of magnitude, suggesting that the degree of band bending at the interface is much greater for the ternary alloy than for pure GaP. A graphical representation of this observation is presented in Figure 6.12d. Such differences explain the enhanced carrier separation observed in $\text{GaSb}_x\text{P}_{(1-x)}$.

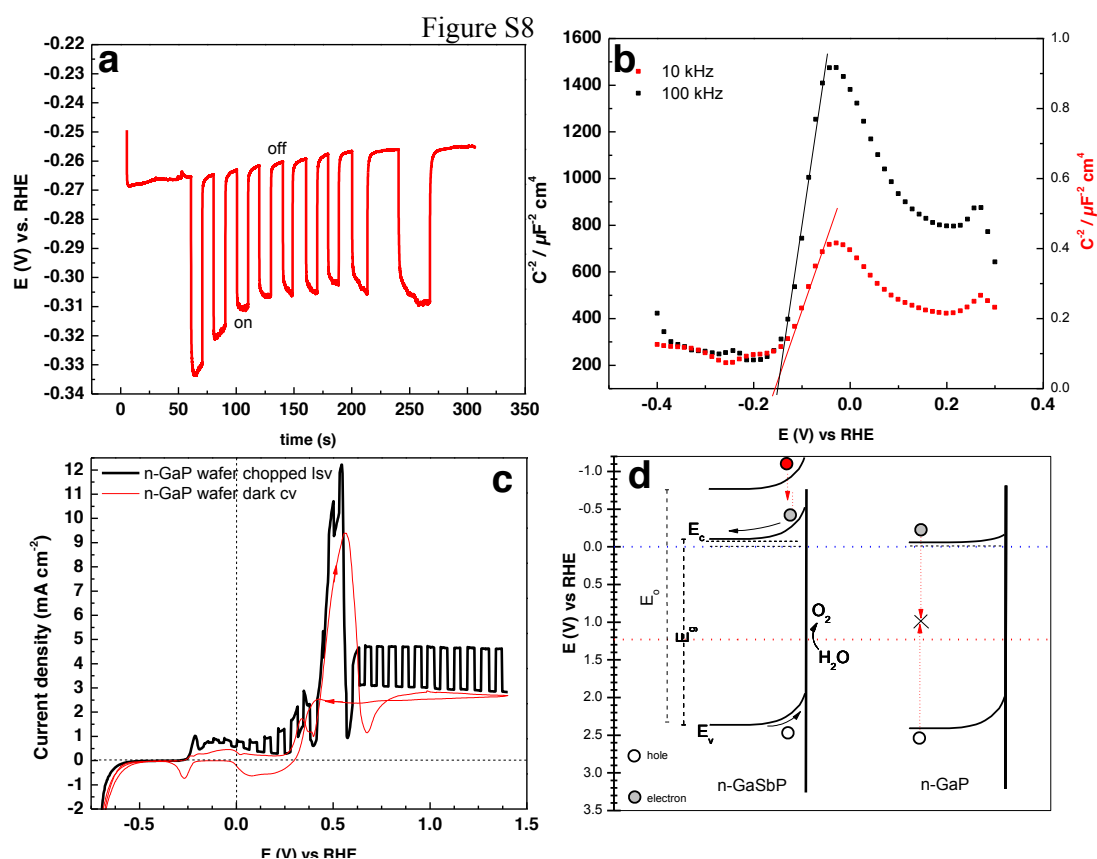


Figure 6.12 Photoelectrochemical characterization of n-GaP photoanode a) Chronopotentiometry under 10 sun chopped illumination, b) Mott-Schottky plot (100 Hz) in the dark c) Linear sweep voltammogram under chopped illumination (10 suns) d) Comparative band diagram of $\text{GaSb}_{0.03}\text{P}_{0.97}$ and GaP

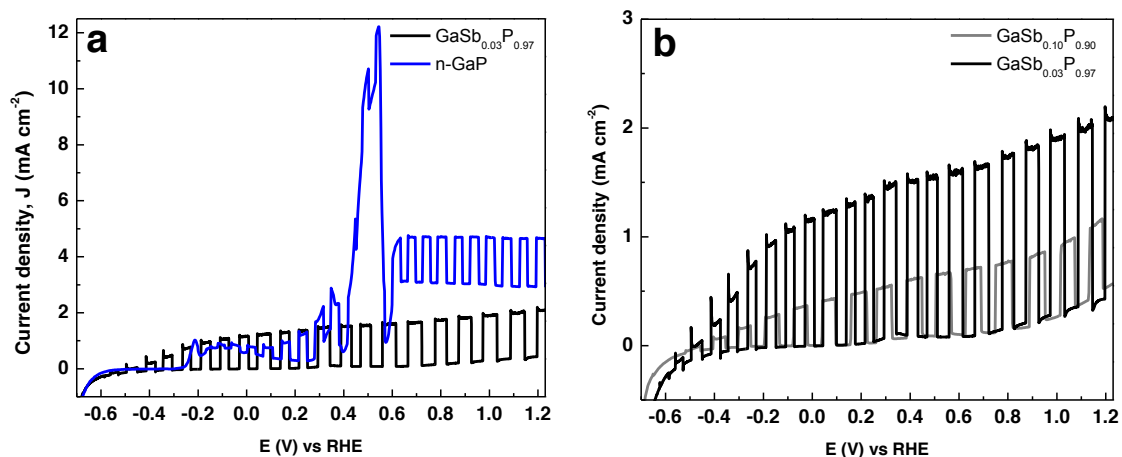


Figure 6.13 Linear sweep voltammograms under chopped illumination (2 suns) in 1M H₂SO₄, a) GaSb_{0.03}P_{0.97} (black) and GaP (blue), b) GaSb_{0.03}P_{0.97} and GaSb_{0.1}P_{0.9}

Based on the flat band potential and the estimated optical band gap and electronic transition of the material, the band structure can be plotted along with the E-x diagram relative to the redox potentials for the water splitting half-reactions, as shown in Figure 6.3d.

The current voltage curve of Figure 6.6b shows an onset potential of -0.55 V vs RHE running a photoanode. This means that the hydrogen evolution reaction is being done at the counterelectrode and the overpotential for that half-reaction is handled by the potentiostat and not included (in the 3 electrode configuration for an anode with a reference). So if the electrode is doing water-splitting only, it is adding voltage to the water oxidation potential with its OER overpotential; therefore this materials is driving a minimum of $0.55 + 1.23 + 0.22 \text{ V} = 2.0 \text{ V}$.

A $\text{GaSb}_x\text{P}_{(1-x)}$ electrode was tested as a wired dual semiconductor PEC cell configuration (Figure 6.14) by shorting the photoanode to 3° miscut p-type silicon (001) counterelectrode and both were subjected to 2 sun illumination.

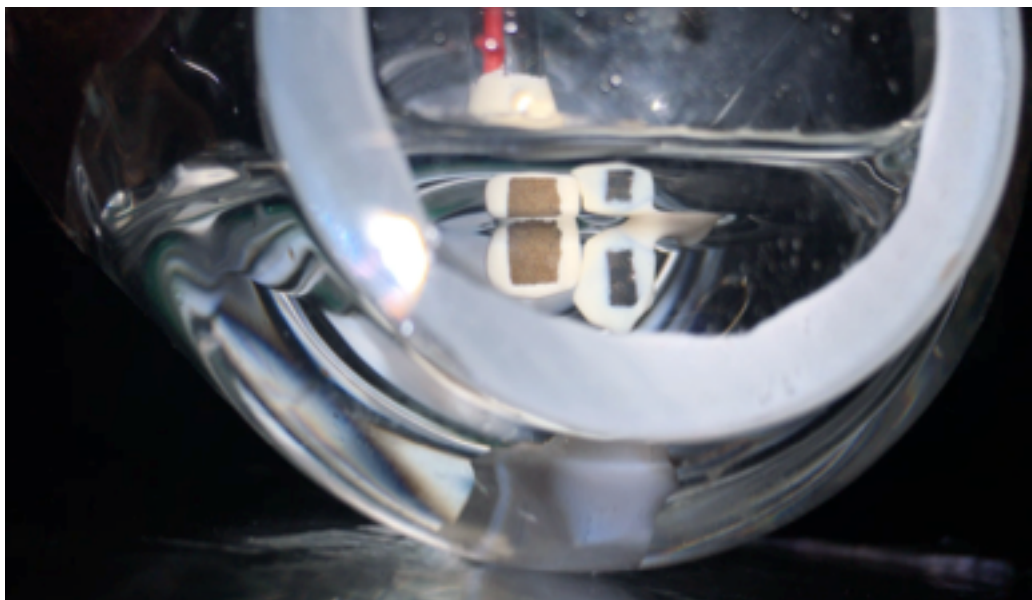


Figure 6.14 Testing of a wired PEC with GaSbP photoanode and GaP coated Si photocathode.

At the beginning of the experiment short circuit current density of 2.8 mA/cm^2 flowed between the electrodes, and decreased to about 2 mA/cm^2 after 1 hour of testing (Figure 6.15, inset). During this experiment hydrogen evolution was observed on the photocathode side of the cell. The net current passing through the circuit at zero bias is consistent with the operating point obtained by overlapping the IV curves of both photoelectrodes at 2 sun illumination (Figure 6.15) The improved photocurrent with this z-scheme results from enhanced absorption of low energy photons at the p-Si photocathode, and demonstrates the feasibility of using $\text{GaSb}_x\text{P}_{(1-x)}$ in a tandem photoelectrochemical cell.

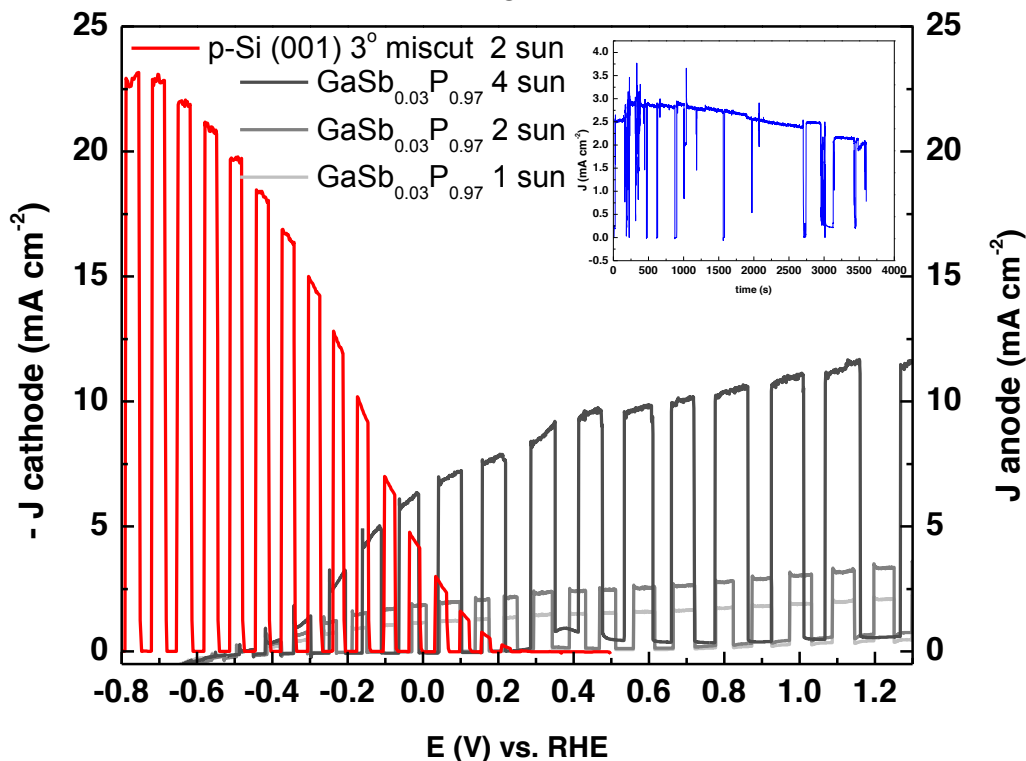


Figure 6.15 Overlapped J-V curves for p-Si photocathode and GaSb_{0.03}P_{0.97} photoanode.

Even though the quality of GaSb_xP_(1-x) films remains to be improved in order to be able to collect more valence band edge holes, the evidence shows that this material has a high efficiency of injection from the valence band energy level. Therefore, it is reasonable to predict that a single crystalline GaSb_xP_(1-x) photoanode would improve the device performance.

We conclude that in the dark and under illumination with radiation of up to 500 nm, the higher lying conduction band of the Γ valley is not normally populated with electrons, however when $h\nu > E_o$ (i.e. 2.65 eV) an appreciable population of hot electrons is observed and these carriers thermalize to the conduction band where they are efficiently separated towards the back contact. This effect is expected to be of general relevance to other semiconductors as hot carrier separation arising from direct transitions

may enable carrying out the water splitting half reactions with photoanodes having indirect band gaps. Optimization of the Sb content in $\text{GaSb}_x\text{P}_{(1-x)}$ films permits obtaining simultaneously a direct band gap semiconductor with high absorption coefficients, and band gap as low as 1.6 eV. The conduction band edge position in $\text{GaSb}_x\text{P}_{(1-x)}$ appears to remain unchanged at a potential between -0.55 and -0.7 eV, while the valence band becomes more negative as Sb is incorporated into the lattice of the ternary alloys.

Despite the enormous amount of publications on direct water photoelectrolysis, only very few studies have reported high efficiencies with a single photoabsorber configuration. Such is the case of Cu_2O , TiO_2 , Fe_2O_3 , BiVO_4 , Ta_3N_5 .^{48,52,120-124} To the best of our knowledge, this is the first report of a single band gap photoanode capable visible-light-driven and un-assisted water oxidation with STH efficiencies up to 2%.

CHAPTER 7

CONCLUSIONS

Coated Cu_2O electrodes benefit from the protective effect of WO_3 as a barrier is formed to prevent the dissolution of Cu_2O in the electrolyte, thereby extending the durability. WO_3 is more resistant than Cu_2O to photocorrosion by electrons because unlike Cu_2O , the WO_3 reduction potential is above its conduction band minimum.

The high crystallinity of the n-type WO_3 provides for faster charge transport and better carrier separation.

Phase purity of Cu_2O - that results from the reducing effect of WO_2 during deposition of WO_3 – is key to bettering the current density of the electrodes.

Thin epitaxial films of $\text{GaSb}_x\text{N}_{1-x}$ with optical band gaps as low as 1.8 eV were grown on GaN.

Heteroepitaxial growth of $\text{GaSb}_x\text{N}_{1-x}$ was achieved on silicon towards the implementation of a tandem III-V on Silicon as a monolithic dual absorber PEC configuration.

$\text{GaSb}_x\text{N}_{(1-x)}$ with optical band gaps for absorption of radiation in the visible wavelength are un-intentionally doped n^{++} , leading to degeneracy and a metal-like behavior that which limited the barrier height at the solid-liquid interface as demonstrated

by low photovoltages and positive position of the conduction band edge with respect to the hydrogen evolution potential.

Charges extending throughout the band gap of the semiconductor that result in a continuum of states in between the E_c and E_v , eliminate the required electrochemical potential differences between the phases. Degenerately doped $\text{GaSb}_x\text{N}_{(1-x)}$ does not show a depletion region and presents poor carrier separation.

$\text{GaSb}_x\text{P}_{1-x}$ thick films were deposited by Halide vapor phase epitaxy using inexpensive metallic precursors. The growth conditions of these compact and free-standing films were studied to optimize the performance of photoanodes for un-assisted PEC water splitting.

The results of this work prove that the temperature of the Sb source in the HVPE reactor is the key parameter for controlling the concentration of Sb in the alloy as well as the band gap the resulting material.

Experimental results indicate that only photon energies greater than 2.68 eV generate mobile and extractable charges, thus suggesting that the higher-laying conduction bands in the Γ_1 valley are populated by photoexcitation. Here it is demonstrated that a low penetration depth and efficient carrier extraction to the indirect conduction band of the material can be achieved above the energy level of the hydrogen reduction potential. Single semiconductor water splitting can be accomplished by tuning the band structure of $\text{GaSb}_x\text{P}_{1-x}$ through incorporation of antimony into the lattice of GaP.

The indirect-to-direct band gap cross-over composition for this material was estimated to be between 3-6%at Sb in the alloy. The indirect material with formula $\text{GaSb}_{0.03}\text{P}_{0.97}$ showed the highest STH efficiency for water splitting.

This work reports a single band gap photoanode capable visible-light-driven and un-assisted water oxidation with STH efficiencies up to 2% with no co-catalysts, additional passivation layers or surface functionalization.

The native conductivity type of the alloy is modified by silicon doping, resulting in a photovoltage of 750 mV, photocurrents of 7 mA cm^{-2} at 10 sun illumination, and corrosion resistance in aqueous acidic environment.

Hydrogen evolution was observed at a Silicon photocathode wired to a $\text{GaSb}_x\text{P}_{1-x}$ photoanode with currents of 2.5 mA cm^{-2} .

EIS and illuminated OCP measurements show that the conduction band of $\text{GaSb}_x\text{P}_{1-x}$ lays at -0.55 V vs. RHE irrespective of the Sb concentration, while PCS indicates that only radiation with photon energies greater than 2.68 eV generate mobile and extractable charges.

These results validate DFT predictions pertaining to the band structure and gap reduction in ternary semiconductors, confirming the importance of U-corrections to aid the search for new, efficient photoabsorbers for direct solar energy conversion to hydrogen.

$\text{GaSb}_x\text{P}_{(1-x)}$ was tested with p-type silicon (001) as a wired dual PEC cell and both were subjected to 2 sun illumination. A current density of 2.8 mA/cm^2 was measured between the electrodes and remained stable for 1 hour of testing.

Hydrogen evolution was observed on the photocathode side of the cell. Improved photocurrent with a z-scheme configuration results from enhanced absorption of low energy photons at the p-Si photocathode, and demonstrates the feasibility of using $\text{GaSb}_x\text{P}_{(1-x)}$ in a tandem photoelectrochemical cell.

CHAPTER 8

RECOMMENDATIONS

Improving the radial uniformity by implementing a rotatory susceptor in the MOCVD tool is highly recommended in order to be able to produce larger areas of samples to test. Additionally, having samples uniform thickness will simplify the assessment of the behavior of electrodes used for PEC tests, as the light absorption processes are highly dependent on the thickness of the material. Moreover, we have seen that the film morphology evolves as the films growth thicker. The ideal photoabsorbers must be thick enough to have evolved to the later growth stage, where charge traps are minimal.

Installation of a water trap in the ammonia source is necessary to improve the precursor purity. This simple modification will help indeed help reduce the un-intentional doping with oxygen and most likely lead to higher photovoltages and carrier separation in the electrodes.

Oxygen leaks into the MOCVD chamber in the order of 10^{19} molecules per minute have to be drastically reduced to synthesize absorbers with a lower donor density, such that the Fermi level equilibration process with the electrolyte creates more band bending.

For future experiments it is recommended to carry out resistivity and Hall measurements in order to evaluate the conductivity of the samples to compare the

dependence of photovoltage of degenerately doped samples and others grown with moderate doping.

It is recommended to study heteroepitaxy of $\text{GaSb}_x\text{N}_{(1-x)}$ on lattice matching templates such as LiAlO_2 to promote the growth in the A-direction, to avoid formation of stacking faults and make the electrical top contacts in such a way that majority carriers do not have to cross threading dislocations (oriented in the c-direction) to reach cathode.

Delamination of $\text{GaSb}_x\text{P}_{(1-x)}$ from the Silicon substrates needs to be solved in order to fabricate a monolithic dual photoabsorber device. It is suggested that the cool down process must be done slowly to minimize the strain caused by thermal expansion coefficient differences between the alloy and the substrate.

REFERENCES

- 1 Lewis, N. S. & Nocera, D. G. Powering the planet: Chemical challenges in solar energy utilization. *Proc. Natl. Acad. Sci. U. S. A.* **104**, 20142-20142, doi:10.1073/pnas.0710683104 (2007).
- 2 Gielen, D., Boshell, F. & Saygin, D. Climate and energy challenges for materials science. *Nat Mater* **15**, 117-120, doi:10.1038/nmat4545 (2016).
- 3 Miller, E. L., Gaillard, N., Kaneshiro, J., DeAngelis, A. & Garland, R. Progress in new semiconductor materials classes for solar photoelectrolysis. *International Journal of Energy Research* **34**, 1215-1222, doi:10.1002/er.1660 (2010).
- 4 Jiao, F., Bao, J., Hill, A. H. & Bruce, P. G. Synthesis of ordered mesoporous Li-Mn-O spinel as a positive electrode for rechargeable lithium batteries. *Angewandte Chemie International Edition* **47**, 9711-9716 (2008).
- 5 Sixto Gimenez, J. B. in *From Basic Principles to Advanced Devices* (Springer International Publishing, 2016).
- 6 AG, S. *World's Largest Hydrogen Electrolysis Facility*, <<https://http://www.siemens.com/innovation/en/home/pictures-of-the-future/energy-and-efficiency/smart-grids-and-energy-storage-largest-hydrogen-electrolysis-facility.html>> (2017).
- 7 QA, S. *Renewable Energy Storage and Decentralized Hydrogen Production Through Water Electrolysis (SOEC)*, <<http://www.soctesqa.eu/socells/applications-1/renewable-energy-storage-and-decentralized-hydrogen-production-through-water-electrolysis-soec>> (2017).
- 8 Energy, U. D. o. *DOE Hydrogen and Fuel Cells Program Record*, <https://http://www.hydrogen.energy.gov/pdfs/12014_current_us_hydrogen_production.pdf> (2012).
- 9 Nielander, A. C., Shaner, M. R., Papadantonakis, K. M., Francis, S. A. & Lewis, N. S. A taxonomy for solar fuels generators. *Energy & Environmental Science* **8**, 16-25, doi:10.1039/C4EE02251C (2015).
- 10 Hisatomi, T., Kubota, J. & Domen, K. Recent advances in semiconductors for photocatalytic and photoelectrochemical water splitting. *Chemical Society Reviews* **43**, 7520-7535, doi:10.1039/C3CS60378D (2014).
- 11 Lewerenz, H. J. *et al. Photoelectrochemical Water Splitting: Materials, Processes and Architectures*. (Royal Society of Chemistry, 2013).

- 12 Chung, S. *et al.* Evidence for a large phononic band gap leading to slow hot carrier thermalisation. *IOP Conference Series: Materials Science and Engineering* **68**, 012002 (2014).
- 13 Zhebo Chen, H. D., Eric Miller. in *Standard* (Springer-Verlag, New York, 2013).
- 14 Roel van de Krol, M. G. Vol. 102 (Springer US, 2012).
- 15 Wang, T. & Gong, J. Single-Crystal Semiconductors with Narrow Band Gaps for Solar Water Splitting. *Angewandte Chemie (International ed. in English)* **54**, 10718-10732, doi:10.1002/anie.201503346 (2015).
- 16 Sunkara, S. *et al.* New Visible Light Absorbing Materials for Solar Fuels, Ga(Sb_x)N_{1-x} Alloy. *Advanced Materials* **26**, 2878-2882 (2014).
- 17 Chen, Z. *et al.* Accelerating materials development for photoelectrochemical hydrogen production: Standards for methods, definitions, and reporting protocols. *Journal of Materials Research* **25**, 3-16 (2010).
- 18 Hu, S., Xiang, C., Haussener, S., Berger, A. D. & Lewis, N. S.
An analysis of the optimal band gaps of light absorbers in integrated tandem photoelectrochemical water-splitting systems. *Energy & Environmental Science* **6**, 2984-2993 (2013).
- 19 Mueller-Langer, F., Tzimas, E., Kaltschmitt, M. & Peteves, S. Techno-economic assessment of hydrogen production processes for the hydrogen economy for the short and medium term. *International Journal of Hydrogen Energy* **32**, 3797-3810, doi:<http://doi.org/10.1016/j.ijhydene.2007.05.027> (2007).
- 20 Khaselev, O. & Turner, J. A. A Monolithic Photovoltaic-Photoelectrochemical Device for Hydrogen Production via Water Splitting. *Science* **280**, 425-427, doi:10.1126/science.280.5362.425 (1998).
- 21 Peter, L. M. in *Photocatalysis: Fundamentals and Perspectives* 1-28 (The Royal Society of Chemistry, 2016).
- 22 Walter, M. G. *et al.* Solar water splitting cells. *Chemical reviews* **110**, 6446-6473 (2010).
- 23 Fujishima, A. & Honda, K. Electrochemical Photolysis of Water at a Semiconductor Electrode. *Nature* **238**, 37-38 (1972).
- 24 Peter, L. M. Photoelectrochemical Water Splitting. A Status Assessment. *Electroanalysis* **27**, 864-871 (2015).
- 25 (ed The National Academies Press) (Washington DC, 2004).
- 26 Pinaud, B. A. *et al.* Technical and economic feasibility of centralized facilities for solar hydrogen production via photocatalysis and photoelectrochemistry. *Energy & Environmental Science* **6**, 1983-2002, doi:10.1039/C3EE40831K (2013).

- 27 Fountaine, K. T., Lewerenz, H. J. & Atwater, H. A. Efficiency limits for photoelectrochemical water-splitting. *Nature communications* **7**, 13706 (2016).
- 28 Wang, Q. *et al.* Scalable water splitting on particulate photocatalyst sheets with a solar-to-hydrogen energy conversion efficiency exceeding 1%. *Nat Mater* **15**, 611-615, doi:10.1038/nmat4589
<http://www.nature.com/nmat/journal/v15/n6/abs/nmat4589.html> - [supplementary-information](#) (2016).
- 29 Bornoz, P. *et al.* A Bismuth Vanadate–Cuprous Oxide Tandem Cell for Overall Solar Water Splitting. *The Journal of Physical Chemistry C* **118**, 16959-16966, doi:10.1021/jp500441h (2014).
- 30 Wang, H., Deutsch, T. & Turner, J. A. Direct water splitting under visible light with nanostructured hematite and WO₃ photoanodes and a GaInP₂ photocathode. *Journal of the Electrochemical Society* **155**, F91-F96 (2008).
- 31 Coridan, R. H., Shaner, M., Wiggenhorn, C., Brunschwig, B. S. & Lewis, N. S. Electrical and Photoelectrochemical Properties of WO₃/Si Tandem Photoelectrodes. *The Journal of Physical Chemistry C* **117**, 6949-6957 (2013).
- 32 Liu, C., Tang, J., Chen, H. M., Liu, B. & Yang, P. A Fully Integrated Nanosystem of Semiconductor Nanowires for Direct Solar Water Splitting. *Nano Letters* **13**, 2989-2992, doi:10.1021/nl401615t (2013).
- 33 Abdi, F. F. *et al.* Efficient solar water splitting by enhanced charge separation in a bismuth vanadate-silicon tandem photoelectrode. *Nat Commun* **4**, 2195, doi:10.1038/ncomms3195 (2013).
- 34 Brillet, J. *et al.* Highly efficient water splitting by a dual-absorber tandem cell. *Nature Photonics* **6**, 823-827, doi:10.1038/nphoton.2012.265 (2012).
- 35 Lin, C.-Y., Lai, Y.-H., Mersch, D. & Reisner, E. Cu₂O| NiO_x nanocomposite as an inexpensive photocathode in photoelectrochemical water splitting. *Chemical Science* **3**, 3482-3487 (2012).
- 36 Khaselev, O. & Turner, J. A. Electrochemical stability of p-GaInP₂ in aqueous electrolytes toward photoelectrochemical water splitting. *J. Electrochem. Soc.* **145**, 3335-3339, doi:10.1149/1.1838808 (1998).
- 37 Kainthla, R. C., Zelenay, B. & Bockris, J. O. M. Significant Efficiency Increase in Self - Driven Photoelectrochemical Cell for Water Photoelectrolysis. *Journal of The Electrochemical Society* **134**, 841-845, doi:10.1149/1.2100583 (1987).
- 38 Nozik, A. J. P-N photoelectrolysis cells. *Appl. Phys. Lett.* **29**, 150-153, doi:10.1063/1.89004 (1976).
- 39 Ohashi, K., Uosaki, K. & Bockris, J. O. M. Cathodes For Photodriven Hydrogen Generators: ZnTe and CdTe. *International Journal of Energy Research* **1**, 25-30, doi:10.1002/er.4440010104 (1977).

- 40 Ager, J. W., Shaner, M. R., Walczak, K. A., Sharp, I. D. & Ardo, S. Experimental demonstrations of spontaneous, solar-driven photoelectrochemical water splitting. *Energy & Environmental Science* **8**, 2811-2824, doi:10.1039/C5EE00457H (2015).
- 41 Chen, S. & Wang, L.-W. Thermodynamic Oxidation and Reduction Potentials of Photocatalytic Semiconductors in Aqueous Solution. *Chemistry of Materials* **24**, 3659-3666, doi:10.1021/cm302533s (2012).
- 42 Gurudayal *et al.* Perovskite–Hematite Tandem Cells for Efficient Overall Solar Driven Water Splitting. *Nano Letters* **15**, 3833-3839, doi:10.1021/acs.nanolett.5b00616 (2015).
- 43 Strandwitz, N. C. *et al.* Photoelectrochemical Behavior of Planar and Microwire-Array Si|GaP Electrodes. *Advanced Energy Materials* **2**, 1109-1116, doi:10.1002/aenm.201100728 (2012).
- 44 Ji, L. *et al.* A silicon-based photocathode for water reduction with an epitaxial SrTiO₃ protection layer and a nanostructured catalyst. *Nat Nano* **10**, 84-90, doi:10.1038/nnano.2014.277
<http://www.nature.com/nnano/journal/v10/n1/abs/nnano.2014.277.html> - supplementary-information (2015).
- 45 Choi, M. J. *et al.* Long-term durable silicon photocathode protected by a thin Al₂O₃/SiO_x layer for photoelectrochemical hydrogen evolution. *Journal of Materials Chemistry A* **2**, 2928-2933, doi:10.1039/C3TA14443G (2014).
- 46 Wu, J. *et al.* Wafer-Scale Fabrication of Self-Catalyzed 1.7. eV GaAsP Core-Shell Nanowire Photocathode on Silicon Substrates. *Nano Letters* **14**, 2013-2018, doi:10.1021/nl500170m (2014).
- 47 Wang, G. *et al.* Hydrogen-Treated TiO₂ Nanowire Arrays for Photoelectrochemical Water Splitting. *Nano Letters* **11**, 3026-3033, doi:10.1021/nl201766h (2011).
- 48 Paracchino, A., Laporte, V., Sivula, K., Grätzel, M. & Thimsen, E. Highly active oxide photocathode for photoelectrochemical water reduction. *Nature Materials* **10**, 456-461, doi:10.1038/nmat3017 (2011).
- 49 Garcia, A. M. *et al.* in *Meeting Abstracts*. 1310-1310 (The Electrochemical Society).
- 50 Luo, J. *et al.* Cu₂O Nanowire Photocathodes for Efficient and Durable Solar Water Splitting. *Nano Letters* **16**, 1848-1857, doi:10.1021/acs.nanolett.5b04929 (2016).
- 51 Morales-Guio, C. G., Tilley, S. D., Vrubel, H., Grätzel, M. & Hu, X. Hydrogen evolution from a copper(I) oxide photocathode coated with an amorphous molybdenum sulphide catalyst. *Nature Communications* **5**, 3059, doi:10.1038/ncomms4059

<https://http://www.nature.com/articles/ncomms4059> - supplementary-information (2014).

- 52 Kim, T. W. & Choi, K.-S. Nanoporous BiVO₄ Photoanodes with Dual-Layer Oxygen Evolution Catalysts for Solar Water Splitting. *Science* **343**, 990-994, doi:10.1126/science.1246913 (2014).
- 53 Pilli, S. K. *et al.* BiVO₄/CuWO₄ heterojunction photoanodes for efficient solar driven water oxidation. *Physical Chemistry Chemical Physics* **15**, 3273-3278 (2013).
- 54 Nozik, A. J. Photoelectrochemistry: Applications to solar energy conversion. *Annual Review of Physical Chemistry* **29**, 189-222 (1978).
- 55 Hwang, Y. J., Wu, C. H., Hahn, C., Jeong, H. E. & Yang, P. Si/InGaN Core/Shell Hierarchical Nanowire Arrays and their Photoelectrochemical Properties. *Nano Letters* **12**, 1678-1682, doi:10.1021/nl3001138 (2012).
- 56 Barick, B. K., Carlos, R.-F., Andres, C. & Dhar, S. Structural and electronic properties of InN nanowire network grown by vapor-liquid-solid method. *AIP Advances* **5**, 057162, doi:10.1063/1.4921946 (2015).
- 57 Monemar, B., Paskov, P. P. & Kasic, A. Optical properties of InN—the bandgap question. *Superlattices and Microstructures* **38**, 38-56, doi:<http://doi.org/10.1016/j.spmi.2005.04.006> (2005).
- 58 Doescher, H. *et al.* Epitaxial III-V Films and Surfaces for Photoelectrocatalysis. *Chemphyschem* **13**, 2899-2909, doi:10.1002/cphc.201200390 (2012).
- 59 Deutsch, T. G., Koval, C. A. & Turner, J. A. III-V nitride epilayers for photoelectrochemical water splitting: GaPN and GaAsPN. *Journal of Physical Chemistry B* **110**, 25297-25307, doi:10.1021/jp0652805 (2006).
- 60 Standing, A. *et al.* Efficient water reduction with gallium phosphide nanowires. *Nature Communications* **6**, doi:10.1038/ncomms8824 (2015).
- 61 Hu, S., Xiang, C., Haussener, S., Berger, A. D. & Lewis, N. S. An analysis of the optimal band gaps of light absorbers in integrated tandem photoelectrochemical water-splitting systems. *Energy & Environmental Science* **6**, 2984-2993 (2013).
- 62 Hu, S., Xiang, C., Haussener, S., Berger, A. D. & Lewis, N. S. An analysis of the optimal band gaps of light absorbers in integrated tandem photoelectrochemical water-splitting systems. *Energy & Environmental Science* **6**, 2984-2993, doi:10.1039/C3EE40453F (2013).
- 63 Prévot, M. S. & Sivula, K. Photoelectrochemical Tandem Cells for Solar Water Splitting. *The Journal of Physical Chemistry C* **117**, 17879-17893, doi:10.1021/jp405291g (2013).
- 64 Zhang, Z. *et al.* Carbon Layer Protected Cuprous Oxide Nanowire Arrays for Efficient Water Reduction. *ACS nano* (2013).

- 65 Verlage, E. *et al.* A monolithically integrated, intrinsically safe, 10% efficient, solar-driven water-splitting system based on active, stable earth-abundant electrocatalysts in conjunction with tandem III-V light absorbers protected by amorphous TiO₂ films. *Energy & Environmental Science* **8**, 3166-3172, doi:10.1039/C5EE01786F (2015).
- 66 Kang, D. *et al.* Electrochemical Synthesis of Photoelectrodes and Catalysts for Use in Solar Water Splitting. *Chemical Reviews* **115**, 12839-12887, doi:10.1021/acs.chemrev.5b00498 (2015).
- 67 Licht, S. *et al.* Efficient Solar Water Splitting, Exemplified by RuO₂-Catalyzed AlGaAs/Si Photoelectrolysis. *The Journal of Physical Chemistry B* **104**, 8920-8924, doi:10.1021/jp002083b (2000).
- 68 May, M. M., Lewerenz, H.-J., Lackner, D., Dimroth, F. & Hannappel, T. Efficient direct solar-to-hydrogen conversion by in situ interface transformation of a tandem structure. *Nature Communications* **6**, 8286, doi:10.1038/ncomms9286
<http://www.nature.com/articles/ncomms9286-supplementary-information> (2015).
- 69 MacLeod, B. A. *et al.* Phosphonic Acid Modification of GaInP₂ Photocathodes Toward Unbiased Photoelectrochemical Water Splitting. *Acs Applied Materials & Interfaces* **7**, 11346-11350, doi:10.1021/acsami.5b01814 (2015).
- 70 Ucer, K. B. *Lecture 12 - Epitaxy*, <<http://users.wfu.edu/ucerkb/Nan242/L12-Epitaxy.pdf>> (2010).
- 71 Ayers, J. E. in *Heteroepitaxy of Semiconductors* 161-248 (CRC Press, 2007).
- 72 Hemmingsson, C., Monemar, B., Kumagai, Y. & Koukitu, A. in *Springer Handbook of Crystal Growth* (eds Govindhan Dhanaraj, Kullaiah Byrappa, Vishwanath Prasad, & Michael Dudley) 869-896 (Springer Berlin Heidelberg, 2010).
- 73 Fan, S. *et al.* High Efficiency Solar-to-Hydrogen Conversion on a Monolithically Integrated InGaN/GaN/Si Adaptive Tunnel Junction Photocathode. *Nano Letters* **15**, 2721-2726, doi:10.1021/acs.nanolett.5b00535 (2015).
- 74 Dahal, R., Pantha, B. N., Li, J., Lin, J. Y. & Jiang, H. X. Realizing InGaN monolithic solar-photoelectrochemical cells for artificial photosynthesis. *Applied Physics Letters* **104**, doi:10.1063/1.4871105 (2014).
- 75 Deguchi, M., Yotsuhashi, S., Hashiba, H., Yamada, Y. & Ohkawa, K. Enhanced Capability of Photoelectrochemical CO₂ Conversion System Using an AlGaN/GaN Photoelectrode. *Japanese Journal of Applied Physics* **52**, doi:10.7567/jjap.52.08jf07 (2013).
- 76 Yotsuhashi, S. *et al.* Enhanced CO₂ reduction capability in an AlGaN/GaN photoelectrode. *Applied Physics Letters* **100**, doi:10.1063/1.4729298 (2012).

- 77 Deguchi, M., Yotsuhashi, S., Yamada, Y. & Ohkawa, K. Photoelectrochemical CO₂ Conversion to Hydrocarbons Using an AlGa_N/Ga_N-Si Tandem Photoelectrode. *Advances in Condensed Matter Physics*, doi:10.1155/2015/537860 (2015).
- 78 Bellaiche, L., Wei, S.-H. & Zunger, A. Composition dependence of interband transition intensities in GaPN, GaAsN, and GaPAs alloys. *Physical Review B* **56**, 10233-10240 (1997).
- 79 Supplie, O. *et al.* Materials for light-induced water splitting: In situ controlled surface preparation of GaPN epilayers grown lattice-matched on Si(100). *Journal of Applied Physics* **115**, doi:10.1063/1.4869121 (2014).
- 80 Sunkara, S. *New Visible light absorber for solar fuels: GaSbxN_{1-x} alloys* PhD in Chemical Engineering thesis, University of Louisville, (2015).
- 81 Russell, H. B. *et al.* Direct Band Gap Gallium Antimony Phosphide (GaSbxP_{1-x}) Alloys. *Scientific Reports* **6**, 20822, doi:10.1038/srep20822 <http://www.nature.com/articles/srep20822 - supplementary-information> (2016).
- 82 Andriotis, N. A., Sheetz, R. M., Ernst, R. & Madhu, M. Band alignment and optical absorption in Ga(Sb)N alloys. *J. Phys: Cond. Matt.* **26**, 055013 (2014).
- 83 Andriotis, A. N., Mpourmpakis, G., Lisenkov, S., Sheetz, R. M. & Menon, M. U-calculation of the LSDA + U functional using the hybrid B3LYP and HSE functionals. *physica status solidi (b)* **250**, 356-363, doi:10.1002/pssb.201248215 (2013).
- 84 Sheetz, R. M. *et al.* Visible-light absorption and large band-gap bowing of GaN 1- x Sb x from first principles. *Physical Review B* **84**, 075304 (2011).
- 85 Morávek, P., Fulem, M., Pangráč, J., Hulicius, E. & Růžička, K. Vapor pressures of dimethylcadmium, trimethylbismuth, and tris(dimethylamino)antimony. *Fluid Phase Equilibria* **360**, 106-110, doi:<http://dx.doi.org/10.1016/j.fluid.2013.09.017> (2013).
- 86 Jaramillo-Cabanzo, D. F., Willing, G. A. & Sunkara, M. K. Plasma Etching Chemistry for Smoothing of Ultrananocrystalline Diamond Films. *ECS Solid State Letters* **4**, P80-P84, doi:10.1149/2.0081510ssl (2015).
- 87 Le Formal, F. *et al.* Back Electron-Hole Recombination in Hematite Photoanodes for Water Splitting. *Journal of the American Chemical Society* **136**, 2564-2574, doi:10.1021/ja412058x (2014).
- 88 Chen, Z. B. *et al.* Accelerating materials development for photoelectrochemical hydrogen production: Standards for methods, definitions, and reporting protocols. *J. of Mat. Res.* **25**, 3-16, doi:10.1557/jmr.2010.0020 (2010).
- 89 Krishnan, R. in *Encyclopedia of Electrochemistry* (Wiley-VCH Verlag GmbH & Co. KGaA, 2007).

- 90 Sunkara, S., Vendra, V. K., Kim, J. H., Druffel, T. & Sunkara, M. K. Scalable synthesis and photoelectrochemical properties of copper oxide nanowire arrays and films. *Catalysis Today* **199**, 27-35, doi:<http://dx.doi.org/10.1016/j.cattod.2012.03.014> (2013).
- 91 Paracchino, A. *et al.* Ultrathin films on copper(i) oxide water splitting photocathodes: a study on performance and stability. *Energy & Environmental Science* **5**, 8673-8681, doi:10.1039/c2ee22063f (2012).
- 92 Zhang, Z. & Wang, P. Highly stable copper oxide composite as an effective photocathode for water splitting via a facile electrochemical synthesis strategy. *Journal of Materials Chemistry* **22**, 2456-2464 (2012).
- 93 Huang, Q., Kang, F., Liu, H., Li, Q. & Xiao, X. Highly aligned Cu₂O/CuO/TiO₂ core/shell nanowire arrays as photocathodes for water photoelectrolysis. *Journal of Materials Chemistry A* **1**, 2418-2425 (2013).
- 94 Thangala, J., Vaddiraju, S., Malhotra, S., Chakrapani, V. & Sunkara, M. K. A hot-wire chemical vapor deposition (HWCVD) method for metal oxide and their alloy nanowire arrays. *Thin Solid Films* **517**, 3600-3605, doi:<http://dx.doi.org/10.1016/j.tsf.2009.01.051> (2009).
- 95 Zheng, J. Y., Song, G., Kim, C. W. & Kang, Y. S. Facile preparation of p-CuO and p-CuO/n-CuWO₄ junction thin films and their photoelectrochemical properties. *Electrochimica Acta* (2012).
- 96 Thangala, J. *et al.* Large-Scale, Hot-Filament-Assisted Synthesis of Tungsten Oxide and Related Transition Metal Oxide Nanowires. *Small* **3**, 890-896, doi:10.1002/sml.200600689 (2007).
- 97 Peter, L. Energetics and kinetics of light-driven oxygen evolution at semiconductor electrodes: the example of hematite. *Journal of Solid State Electrochemistry* **17**, 315-326, doi:10.1007/s10008-012-1957-3 (2013).
- 98 Lawrence S. Pan, D. R. K. Vol. 1 (Springer US, New York, 1995).
- 99 Zhu, D., Wallis, D. J. & Humphreys, C. J. Prospects of III-nitride optoelectronics grown on Si. *Reports on Progress in Physics* **76**, 106501 (2013).
- 100 Hiramatsu, K. *et al.* Growth mechanism of GaN grown on sapphire with AlN buffer layer by MOVPE. *Journal of Crystal Growth* **115**, 628-633, doi:[http://dx.doi.org/10.1016/0022-0248\(91\)90816-N](http://dx.doi.org/10.1016/0022-0248(91)90816-N) (1991).
- 101 Peng, L. *MOCVD growth and characterization of wide band gap group III-nitride semiconductors*, National University of Singapore, (2003).
- 102 Kung, W., Jasprit, S. & Dimitris, P. Theoretical study of GaN growth: A Monte Carlo approach. *Journal of Applied Physics* **76**, 3502-3510, doi:10.1063/1.357479 (1994).
- 103 Streetman, B. G. & Banerjee, S. *Solid State Electronic Devices*. (PRENTICE HALL, 2015).

- 104 Kim, H.-i., Monllor-Satoca, D., Kim, W. & Choi, W. N-doped TiO₂ nanotubes coated with a thin TaO_xN_y layer for photoelectrochemical water splitting: dual bulk and surface modification of photoanodes. *Energy & Environmental Science* **8**, 247-257, doi:10.1039/C4EE02169J (2015).
- 105 Bard, A. J., Bocarsly, A. B., Fan, F. R. F., Walton, E. G. & Wrighton, M. S. The concept of Fermi level pinning at semiconductor/liquid junctions. Consequences for energy conversion efficiency and selection of useful solution redox couples in solar devices. *Journal of the American Chemical Society* **102**, 3671-3677, doi:10.1021/ja00531a001 (1980).
- 106 Nair, V., Perkins, C. L., Lin, Q. & Law, M. Textured nanoporous Mo:BiVO₄ photoanodes with high charge transport and charge transfer quantum efficiencies for oxygen evolution. *Energy & Environmental Science* **9**, 1412-1429, doi:10.1039/C6EE00129G (2016).
- 107 Puhlmann, N., Oelgart, G., Gottschalch, V. & Nemitz, R. Minority carrier recombination and internal quantum yield in GaAs:Sn by means of EBIC and CL. *Semiconductor Science and Technology* **6**, 181 (1991).
- 108 Somanathan, N. B. & R, S. *Solid State Devices*. (PHI Learning Pvt. Ltd.).
- 109 *Engineering Physics*. (McGraw-Hill Education (India) Pvt Limited, 2010).
- 110 Pierret, R. F. *Advanced Semiconductor Fundamentals*. (Prentice Hall, 2003).
- 111 Grundmann, M. *The Physics of Semiconductors: An Introduction Including Nanophysics and Applications*. (Springer Berlin Heidelberg, 2010).
- 112 Zhu, T. & Oliver, R. A. Unintentional doping in GaN. *Physical Chemistry Chemical Physics* **14**, 9558-9573, doi:10.1039/C2CP40998D (2012).
- 113 Wright, A. F. Substitutional and interstitial oxygen in wurtzite GaN. *Journal of Applied Physics* **98**, 103531, doi:10.1063/1.2137446 (2005).
- 114 Sciences, T. R. S. A. o. Efficient Blue Light-Emitting Diodes Leading to Bright and Energy-Saving White Light Sources. (Stockholm, Sweden, 2014).
- 115 Edgar, J. H. *Properties, Processing and Applications of Gallium Nitride and Related Semiconductors*. (INSPEC, 1999).
- 116 Yohannes, K. & Kuo, D.-H. Growth of p-type Cu-doped GaN films with magnetron sputtering at and below 400 °C. *Materials Science in Semiconductor Processing* **29**, 288-293, doi:<http://doi.org/10.1016/j.mssp.2014.05.010> (2015).
- 117 Morkoç, H. *Nitride Semiconductors and Devices*. (Springer Berlin Heidelberg, 2013).
- 118 Russell, H. B. *Direct band gap gallium antimonide phosphide (GaSbxP1-x) for solar fuels*, University of Louisville, (2016).

- 119 Sunkara, S. *et al.* New Visible Light Absorbing Materials for Solar Fuels, Ga(Sb-x)N_{1-x}. *Advanced Materials* **26**, 2878-2882, doi:10.1002/adma.201305083 (2014).
- 120 Paracchino, A. *et al.* Ultrathin films on copper (i) oxide water splitting photocathodes: a study on performance and stability. *Energy & Environmental Science* **5**, 8673-8681 (2012).
- 121 Zhong, D. K., Choi, S. & Gamelin, D. R. Near-Complete Suppression of Surface Recombination in Solar Photoelectrolysis by “Co-Pi” Catalyst-Modified W:BiVO₄. *Journal of the American Chemical Society* **133**, 18370-18377, doi:10.1021/ja207348x (2011).
- 122 Zhong, D. K., Cornuz, M., Sivula, K., Graetzel, M. & Gamelin, D. R. Photo-assisted electrodeposition of cobalt-phosphate (Co-Pi) catalyst on hematite photoanodes for solar water oxidation. *Energy & Environmental Science* **4**, 1759-1764, doi:10.1039/c1ee01034d (2011).
- 123 Li, Y. *et al.* Cobalt phosphate-modified barium-doped tantalum nitride nanorod photoanode with 1.5% solar energy conversion efficiency. *Nat Commun* **4**, doi:10.1038/ncomms3566 (2013).
- 124 Liu, G. *et al.* Enabling an integrated tantalum nitride photoanode to approach the theoretical photocurrent limit for solar water splitting. *Energy & Environmental Science* **9**, 1327-1334, doi:10.1039/C5EE03802B (2016).

CURRICULUM VITAE

Alejandro Martinez Garcia

Education

- Doctor of Philosophy in Chemical Engineering Summer 2012- May 2017 University of Louisville.
- Master of Science in Chemical Engineering Spring 2010-Spring 2012
- Universidad de los Andes, Bogota, Colombia.
- Bachelor of Science in Chemical Engineering, Minor in Chemistry Fall 2002-Fall 2007. Universidad de los Andes, Bogota, Colombia

Research and Work Experience

- Conn Center for Renewable Energy Research, University of Louisville, KY May 2012 – May. 2017
- Universidad de los Andes, Bogota, Colombia Jan 2010-March 2011
- Cavalier Abogados Patent Law Firm, Bogota, Colombia , Jan 2008-Jan 201

Leadership Activities, Campus Involvement, and volunteer work

- President of the Chemical Engineering Graduate Student Association (2014-2015).
- Society of Hispanic Professional Engineers student chapter at The University of Louisville.
- Served as advisor/mentor for high-school and undergraduate students in research summer camps, and science fair projects.
- Volunteered to teach courses on Advanced Materials for Renewable Energy Challenges at UDLA in Bogota, Colombia in 2015 and at NITT in Tiruchirappalli, India.

Honors and Awards

- University of Louisville Fellowship 2012-2013
- J.B Speed School of Engineering, Grosscurth Fellowship, 2012-2014
- Powering the Kentucky Bioeconomy for a Sustainable Future, NSF Grant / Speed School Dean's Office, 2016

Publications

1. **A. Martinez-Garcia** & M.K Sunkara, et. al, *Un-assisted Water Splitting Using a $GaSb_xP_{(1-x)}$ Photoanode*, Manuscript in Preparation, 2017.
2. **A. Martinez-Garcia** & M.K Sunkara, et. al, *VLS-grown $GaSbN$ Thin Films for Photoelectrochemical Hydrogen Production*, Manuscript in Preparation, 2017.
3. **Martinez-Garcia, A.** et al. *High rate and durable, binder free anode based on silicon loaded MoO_3 nanoplatelets*. Sci. Rep. 5, 10530; doi: 10.1038/srep10530 (2015).
4. **A. Martinez-Garcia**, V.K. Vendra, S. Sunkara, P. Haldankar, J. Jasinski, and M.K. Sunkara, *Tungsten oxide coated copper oxide nanowire arrays for enhanced activity and*

- durability with photoelectrochemical water splitting*, J. Mater. Chem. A., 1 (48), 15235 - 15241, (2013).
5. Dustin R. Cummins, Ulises Martinez, Rajesh Kappera, Damien Voiry, **Alejandro Martinez-Garcia**, Jacek Jasinski, Dan Kelly, Manish Chhowalla, Aditya D. Mohite, Mahendra K. Sunkara, and Gautam Gupta. *Catalytic Activity in Lithium-Treated Core-Shell MoOx/MoS₂ Nanowires*. The Journal of Physical Chemistry C (2015) Article ASAP DOI: 10.1021/acs.jpcc.5b05640
 6. Dustin R. Cummins & **Alejandro Martinez-Garcia**, et al. *Efficient hydrogen evolution in transition metal dichalcogenides via a simple one-step hydrazine reaction*. Nat. Commun. 7:11857 doi: 10.1038/ncomms11857 (2016).
 7. H.B. Russell & **A. Martinez Garcia**, et al. *Direct Band Gap Gallium Antimony Phosphide (GaSb_xP_{1-x}) Alloys*. Nature Sci. Rep. 6, 20822; doi: 10.1038/srep20822 (2016).

Conference Presentations

1. **A. Martinez-Garcia** et al., Tungsten Oxide Coated Copper Oxide Nanowire Arrays for Enhanced Activity and Durability with Photoelectrochemical Water Splitting, ECS Meeting, Orlando FL, Oct 2014.
2. **A. Martinez-Garcia** et al., New III-V Semiconductor Alloys for Solar Hydrogen Production, SPIE Meeting, San Diego CA, Aug 2015.
3. **A. Martinez-Garcia** et al., Novel Band-Gap Engineered III-V Alloys for Unassisted Water Photoelectrolysis, ECS PRIME Meeting, Honolulu HI, Oct 2016.
4. **Alejandro Martinez**, Diana M. Liévano and Pablo Ortiz. Flow Characteristics Across Hydrophobic/Hydrophilic Packed Beds in Hele-Shaw Cell. Conference Proceedings AIChE Annual Meeting, Salt Lake City UT (2010). <http://apps.aiche.org/proceedings/Abstract.aspx?PaperID=197627>
5. **Alejandro Martinez**, Daniel F. Jaramillo and Pablo Ortiz. Hot-wire assisted Chemical Vapor Deposition (HWCVD) of Niobium Nitride Thin Films. Department of Chemical Engineering, Universidad de los Andes. AIChE Annual Meeting, Minneapolis MN (2011). <http://aiche.confex.com/aiche/2011/webprogrampreliminary/Paper238550.html>
6. Daniel F. Jaramillo, **Alejandro Martinez**, Ana M. Araujo and Pablo Ortiz. Effect of Process Variables on Microstructure and Composition of HWCVD Tungsten Oxides Thin Films. Department of Chemical Engineering, Universidad de los Andes. AIChE Annual Meeting, Minneapolis MN (2011).
7. Daniel F. Lopez, Jhon A. Triana, **Alejandro Martinez**, Marcela Hernandez and Pablo Ortiz. Mixing Distribution Pattern in a Glass Packed Bed as a Function of Hydrophobic/Hydrophilic Surface Treatment. Departments of Chemical and Computer Engineering, Universidad de los Andes. AIChE Annual Meeting, Minneapolis MN (2011).